DEVELOPMENT OF HIGH-PERFORMANCE, LIGHTWEIGHT, LOW-COST CARBON FIBERS FOR SUSTAINABILITY

A Dissertation
Presented to
The Academic Faculty

by

Jyotsna Ramachandran

In Partial Fulfillment
of the Requirements for the Degree
Doctor of Philosophy in the
School of Materials Science and Engineering

Georgia Institute of Technology

December 2021

DEVELOPMENT OF HIGH-PERFORMANCE, LIGHTWEIGHT, LOW-COST CARBON FIBERS FOR SUSTAINABILITY

Approved by:

Dr. Satish Kumar, *Advisor*
School of Materials Science and Engineering
Georgia Institute of Technology

Dr. Paul Russo
School of Materials Science and Engineering
Georgia Institute of Technology

Dr. Donggang Yao
School of Materials Science and Engineering
Georgia Institute of Technology

Dr. Sankar Nair
School of Chemical and Biomolecular Engineering
Georgia Institute of Technology

Dr. Karl Jacob
School of Materials Science and Engineering
Georgia Institute of Technology

Dr. Guoliang Liu
Department of Chemistry
Virginia Tech

Dr. Mary Lynn Realff
School of Materials Science and Engineering
Georgia Institute of Technology

Date Approved: December 1, 2021

To all the Women in Science- past, present and future.

ACKNOWLEDGEMENTS

Reflecting at the coda of my PhD journey, it took a village to help me navigate it and I take this opportunity to acknowledge their contribution. Starting with my advisor, Dr. Satish Kumar, I am thankful for his constant guidance, support, motivation to showcase my best abilities and limitless patience. I am grateful for his valuable lessons on seeking solutions to challenging research problems and the importance of detail-oriented scientific research, which would stay with me forever. I was fortunate to have worked with the most passionate researchers in Dr. Kumar's group. I am thankful to Dr. Prabhakar Gulgunje, Dr. Huibin Chang, Dr. Clive Liu, Dr. Jeffrey Luo, Dr. Po-Hsiang Wang, and Dr. Shruthi Venkatraman, for training me in the initial stages of my PhD and having resourceful discussions. I wish to acknowledge the contribution and help lent by Dr. Kishor Gupta and Casey Smith while working with a new and challenging research project. This journey would not have been possible without the collaboration and knowledge-sharing by my peer researchers: Pedro Arias Monje, Mingxuan Lu, Mohammad Hamza Kirmani, and Narayan Shirolkar. They have been my friends and support system both inside and outside the lab and I really thank them for their dual roles.

I thank my dissertation committee members: Dr. Donggang Yao, Dr. Karl Jacob, Dr. Mary Lynn Realff, Dr. Paul Russo, Dr. Sankar Nair and Dr. Guoliang Liu, for their critical feedback and time.

I would like to acknowledge the contributions and insightful discussions of my collaborators, Joel Serrano, Dr. Tianyu Liu, John Elliot, Dr. Guoliang Liu from Virgina Tech and Jinwon Cho and Dr. Seung Soon Jang from Georgia Tech.

Outside the lab and the technical work, I am grateful for the leadership experiences that I got to pursue at Georgia Tech. I am thankful for the opportunity to work and lead an amazing group of women through *Women in Materials Science and Engineering*. I have been fortunate to co-lead a conference with brilliant team of graduate students, work for improving belongingness among the graduate community at Tech and most importantly meet some amazing people along the way at the *Graduate Student Government Association*. I wish to particularly thank Robbie Outz, Dr. Jana Stone, Sang Yun-Han, Aroua Gharbi, Francisco Quintero, Sakshi Hattargi, Usman Ashraf, Cong Luo, and Jayce Wu.

I have had numerous mentors along my journey, and I am indebted to their kindness, life-lessons and time. I am grateful to Dr. Abha Misra, my first mentor at the Indian Institute of Science, Bangalore, for introducing me to the world of materials research and inspiring me to continue along the same path. I thank Dracy Blackwell and Dr. Mary Lynn Realff for lending their support and always patiently listening to me. I am also thankful to Colleen Riggle for coaching me to hone my leadership skills. I am grateful to Dr. Anjli Kumar for teaching me the importance of self-reflection and awareness through my PhD journey and beyond. I thank Moe Moe San, Dr. Marie Markarian, Dr. Erica Thompson, from Intel, for inspiring early-career women scientists like me to pursue a career of their passion.

Finally, I wish to acknowledge my friends, near and far away, who have never shied away from lending their support, given their time and believing in me. I am thankful to my friends Pedro, Francisco, Hamza, Neha, Gauri and Ming, for all the fun times in Atlanta and always ending their ears. I also thank my friends from undergraduate

days, Malu, Neeha, Koushik, Sundaram, Gowtham, Ayyapan, Bala, Pranav, Dutta and Narayan, for being there always and sending in their support despite the time zone differences. My home and family in Atlanta are Aditi, Harshit and Narayan. I do not think words suffice for their roles through my journey. I am extremely grateful for all the experiences that we shared together from Flats to Allure, hosting picnics to Grad Gala, and talking non-stop about SGA. More importantly, you three were my sounding board, showing me the mirror when required, feeding me and supporting me through my trials and triumphs.

I owe it to my parents, grandmother, and sister, for their unconditional love and emotional support despite being miles away. I would not be who I am today, without them. I am grateful to them for relentless believing in my abilities, instilling in me the value of education, constantly motivating me to pursue my dreams, no matter the circumstances and always cheering for me. Last but not the least, a special thanks to my bunnies, Snoopy and Luna, for supporting me through the last yet crucial part of my PhD.

TABLE OF CONTENTS

LIST OF TABLES

LIST OF FIGURES

SUMMARY

This dissertation focuses on the development of high-performance carbon fibers for light weighting automobiles to achieve sustainable developmental goals (SDG) of clean energy, climate action and infrastructure. Replacing steel and aluminum used in current day automobiles by carbon fibers leads to low-weight structures (theoretical reduction by ~70 % and 35% for steel and aluminum, respectively) with higher fuel savings and lower emissions. Two pathways were studied to design high performance carbon fibers that could have the potential for such replacement and their widespread use in the future. The first approach towards the goal involved designing porous carbon fibers with low-density and multifunctional capability using blends of poly(acrylonitrile) (PAN) with sacrificial polymers and block copolymers. The second route explored the use of low-cost precursor, asphaltene, to derive carbon fibers.

Porous carbon fibers from gel-spun blends of PAN with sacrificial polymers were the initial systems studied to characterize the mechanical performance upon introduction of porosity. Orientation imparted during gel-spinning of the PAN-sacrificial polymer blends was synergistically combined with the micro-phase separation of the polymer pairs, to tailor the porous morphology of these fibers and their resultant mechanical properties. From five sacrificial polymers, three systems including poly(acrylic acid) (PAA), poly(methyl methacrylate) (PMMA), poly(styrene-co-acrylonitrile) (SAN), were selected due to their intermediate and higher degree of compatibility with PAN, discerned through UV-vis spectroscopy. Porous morphology of the different carbon fibers produced

was characterized through scanning electron microscopy (SEM) and the differences shown due to the sacrificial polymers studied. The variation in pore size caused by the differences in compatibility between PAN and the sacrificial polymer was evaluated experimentally through blend rheology and theoretically using interaction parameter values. The tensile properties of porous carbon fibers from the three systems were compared to that of the non-porous PAN based carbon fibers processed under similar conditions. Specific tensile modulus of the porous carbon fibers derived from PAN-PAA and PAN-PMMA was found to be 15 to 40 % higher than that for the PAN based carbon fibers. Additionally, influence of sacrificial polymer content (5-20 wt%) on the mechanical, structural and morphological properties was studied for the PAN-SAN fiber systems with porous channeled morphology.

This study showed that gel-spinning of bicomponent PAN/PMMA-*b*-PAN fibers provided a versatile means for tuning the mechanical and electrochemical properties of porous carbon fibers, thus allowing for their potential use as structural energy storage materials. Herein, by gel-spinning polymer precursors of poly(acrylonitrile) (PAN) and poly(methyl methacrylate)-*block*-poly(acrylonitrile) (PMMA-*b*-PAN), we produced a series of carbon fibers and systematically studied the morphological, mechanical, and electrochemical properties. Porous carbon fibers with block copolymer (BCP) in the sheath exhibited the best tensile properties with a strength of 1.1 GPa, modulus of ~190 GPa, and electrochemical capacitance of 11 F/g at 10 mV/s when pyrolyzed at 1315 °C under tension. Without tension and at a pyrolysis temperature of 800 °C, the fibers with BCP as both the sheath and core components achieved the highest electrochemical capacitance of 70 F/g at 10 mV/s and highest surface area of 264 m^2/g. The characteristic

correlation length of PMMA-*b*-PAN was calculated through thermodynamically governed computational method and compared with the pore size in the experimentally obtained carbon fibers.

Through the second approach, conditions to gel-spin blends of low-cost precursor of asphaltene with PAN were established. Functionalization of asphaltenes with nitric acid (f-Asp) enabled their complete solubility in dimethylacetamide (DMAc) unlike the as-received asphaltene powder and further resulted in obtaining relatively homogeneous spinning solutions with PAN. Mechanical properties and structural parameters of precursor f-Asp/PAN fibers with their blend ratio ranging from 30/70 to 60/40, were studied. Carbon fibers with maximum tensile strength and modulus of 1.1 GPa and 181 GPa, were obtained from the gel-spun f-Asp/PAN blends. The study suggests that carbon fibers with reasonable mechanical properties can be derived from low-cost asphaltene through the scalable route of solution/gel-spinning.

The two approaches studied in the dissertation present ways to develop high-performance carbon fibers that would have the potential to light weighting automobiles and thus, steer towards a future of achieving SDG.

CHAPTER 1. INTRODUCTION

Carbon fibers (CF) are a class of high-performance material with high tensile strength (2-7 GPa) and modulus (200-900 GPa), high strength to weight ratio, high chemical and thermal resistance and low thermal expansion, that find applications in aerospace, space, structural reinforcement, luxury automotive industry, sporting goods and numerous other structural goods.[2–4] Carbon fibers have stacks of distorted graphene sheets that are oriented roughly parallel to the fiber axis, without any rotational or translational order between the stacked sheets, giving them a turbostratic structure.[5,6] Carbon fibers are classified based on their a) precursors, b) tensile strength and modulus, and c) heat treatment temperature [5,7]. PAN is the most predominantly used precursor[8] for commercial production of carbon fiber, and was industrially sold as 'Orlon' by Dupont.[9] Processing of carbon fibers from PAN involves the spinning of precursor fibers, followed by thermal stabilization in an oxidative environment and carbonization in an inert environment under tension and graphitization.[10] High modulus carbon fibers from PAN are obtained by processing the fibers at higher temperatures and at the cost of decreasing tensile strength, but under optimized conditions carbon fibers with high modulus ranging from 354 -375 GPa and high strength of 5.5- 5.8 GPa were reported by Chae *et al.*[11] Given that PAN is the predominantly used precursor for obtaining high performance carbon fibers, a brief overview of producing these PAN-based carbon fibers is presented in Section 1.1.

1.1. Production of carbon fibers

1.1.1. Spinning of PAN precursor fibers

As stated earlier, production of high-performance carbon fibers starts with the spinning of precursor fibers from PAN. Fiber spinning from PAN involves a variety of techniques including solution spinning further classified into dry, wet and dry-jet wet spinning, gel spinning and electrospinning. Electrospinning is a process that uses electric field to collect charged polymeric fibers on a grounded collector. Solution spinning requires the dissolution of precursor polymer in suitable solvent to prepare the dope solution. In dry spinning, polymer solution extruded through a spinneret is passed through hot chamber to evaporate the dope solvent while in wet spinning the spinneret is submerged in a coagulation bath. A small air gap is introduced for the fibers being extruded before coagulating them, in dry-jet wet spinning. Gel spinning of fibers involves spinning higher molecular weight polymers at lower solid concentrations and coagulating them in a bath of non-solvent maintained at appropriate temperature to induce gelation. The as-spun fibers are drawn at temperatures above the glass transition (T_g) temperature of the polymer to get highly oriented precursor fibers. PAN precursors obtained from gel spinning typically have tensile strength > 0.9 GPa and tensile modulus of 18-22 GPa.[12]

1.1.2. Stabilization and carbonization of PAN

Once the PAN precursor fibers have been produced, they undergo oxidative stabilization in the temperature range of 200-350 °C, followed by carbonization in an inert atmosphere in the temperature range of 1000-1700 °C and an additional step of graphitization, if required, in the temperature range of 2500-3000 °C.[10] Various reaction mechanisms have been proposed for stabilization including formation of heteroatomic cyclic structure, cyclic ladder polymer followed by isomerization, and dehydrogenation.[13] The generally accepted scheme of reactions during oxidative stabilization include

cyclization, dehydrogenation and oxidation.[14] The cyclization allows the formation of infusible and crosslinked ladder-like structure that prevents melting during carbonization. Dehydrogenation and oxidation reactions require an oxidative environment while cyclization can occur in a non-oxidative environment. Study of stabilization kinetics is facilitated by separation of cyclization reaction from dehydrogenation and oxidation by heating in nitrogen.[15] Planar polycyclic carbon is formed during carbonization with the elimination of volatile byproducts including water, ammonia, carbon-oxides and nitrogen.[16] Now that an insight into the way of producing high performance carbon fiber from PAN has been elucidated, the question remains on how they can be tailored to meet the current needs and challenges of the society, specifically focused on sustainability.

1.2. How can the development of carbon fibers be steered to meet sustainable development goals?

With their high tensile strength, modulus and low density, efforts by academics and industry have been made to steer the development of carbon fibers to meet the current United Nation's Sustainable Development Goals (SDG) in the sectors of clean energy, climate action, and infrastructure.[17–19] Light weighting of automobiles using carbon fibers and carbon fiber reinforced composites, provides pathway to achieve the above mentioned SDG.[20,21] Replacing structures of steel and aluminum in automobiles by carbon fiber composites lends the potential of theoretical weight reduction by ~70 % and 35%, respectively.[22] Cascading effect of light weighting of passenger vehicles with high-performance carbon fibers includes fuel savings of 6-8% for every 10% in weight reduction as lesser power is required for accelerating lighter structures, lesser CO_2 /green-house gas emissions, which are all critical given the stringent environmental regulations

and emphasis on clean energy.[17,22–24] The Boeing 787, by adopting the concept of switching aluminum for about 50% of carbon fiber composites resulted in about 20% weight reduction along with fuel savings of 10-12% [25]. Following suit, for light weighting of passenger vehicles through widespread use of carbon fibers and transforming the landscape of sustainable transportation, the Department of Energy (DOE) has established the following conditions: 1. cost of carbon fibers should be ~$5/lb., and 2. have minimum tensile strength and modulus of 1.72 GPa and 172 GPa, respectively.[26]

In addition, using carbon fibers for light-weighting hybrid and electric vehicles has the added benefits of allowing for smaller battery pack, increasing the efficiency and range of these vehicles, thus resulting in lower emissions.[27–29] Going further ahead along the direction, advances in energy storage have paved ways for multifunctional materials that possess both high energy density and load-bearing capacities, thus giving rise to a new class of high-performance structural energy storage materials.[30] Battery packs utilized in current vehicles, like Tesla model S, contribute to ~25% of the vehicle weight without any load-bearing capabilities.[31] A model estimated that on replacing electric car structures made of separate carbon fiber composites and lithium ion battery with a combined structural energy storage carbon composite, an additional weight reduction of 20% are obtained.[32]

With the benefits of light-weighting using carbon fibers, the question remains on ways to achieving these SDGs and we focus upon two potential pathways. First, the dual performance requirements of high energy storage capacity and mechanical strength leads to broadening the functionality of the current high-performance carbon fibers. Non-

porous carbon fibers are excellent structural materials owing to their superior mechanical properties (*e.g.*, strength to weight ratio)[3,33], but because of small surface areas, their electrochemical energy storage capacitance remains unsuitable for use in structural energy storage devices [30,34,35]. Exploiting their load-bearing capacity and improving their electrochemical energy storage performance are being actively pursued.[32,36–40] Imparting porosity to the carbon fibers has been considered a potential avenue to design structural energy storage materials. The density of carbon fibers manufactured from polyacrylonitrile (PAN) precursor varies between 1.73-1.93 g/cm^3.[41] Further reduction in the density of the carbon fibers and increase in specific surface area are possible by introducing porosity resulting in structural energy storage materials. The introduction of pores improves the electrochemical energy storage performance, but it inevitably reduces the mechanical strength when compared to non-porous carbon fibers.[42]

The second part of enabling the widespread use of carbon fibers for light weighting vehicles and other sustainable applications relies on reducing the cost of carbon fibers production without comprising their structural performance. Precursor of carbon fibers, PAN, obtained from petroleum feedstock are significant contributors to their cost and thus options to replace them with alternate precursors including lignin, and cellulose have been studied.[21,41] Asphaltene, a by-product of the crude oil refining, is available in abundance and often disposed off in environmentally destructive ways, due to their low market value.[43] Use of asphaltenes as carbon precursors is studied, due to their low cost (< $1/lb), availability and potential to gain higher valued products from lower valued by-products of crude oil refining.[44–46]

1.3. Porous Carbon Fibers

In addition to light weighting automobiles, porous carbon fibers with high specific surface area also find applications in gas storage, as filtration membranes and catalysis.[47,48] Physical or chemical activation, polymer blend carbonization[49,50], templating using nanoparticles[51–54] and block-copolymers[55], are some of the techniques that have been pursued to produce porous carbon fibers and the following section lends insights into two of them.

1.3.1. Templating

Ordered and disordered porous carbons have been synthesized by templating techniques. The templating process is akin to baking a ceramic jar. Wood is used as a template, to which the ceramic precursor material is coated. The template along with the coating is baked to the desired temperature and the template is removed off by etching, thus obtaining ceramic jars.[56] Micro and mesoporous carbon materials ae synthesized by using templates like zeolites, silicon, silicon dioxide (SiO_2) nanoparticles, mesoporous silicon templates, anodic aluminum oxide(AAO) membranes.[47] Templating techniques are categorized into the two types, namely hard and soft templating.[54] Hard templating involves either the addition of the pore forming agents to the precursor polymers before processing/ spinning or forcing the precursor polymer into the pores of the template.[51,53] Soft templating involves the self- assembly of ordered mesoporous structure by reacting surfactants with precursor polymers, block copolymers and organic molecular templates bonded through interactive forces.[52]

SiO_2 nanoparticles (7 nm) were used as a pore forming agent to synthesize porous carbon fibers from electrospun PAN/SiO_2 composite mats for use as anodes in lithium

(Li) ion batteries.[57] A surface area of 92 m^2/g was attained with 20 wt % addition of SiO_2 to the precursor in comparison to an area of 26.1 m^2/g, without the addition of SiO_2 and the increased surface area led to decrease in interfacial impedance between the electrode and electrolyte as well as improved the diffusional flux for electrolyte ions. SiO_2 and silicon based mesoporous templates have been the most widespread choices, in the literature, for synthesis of mesoporous carbon material. The surface area (250-2500 m^2/g) and resulting porous morphology of carbon materials prepared through templating varied based on the type of templating agents used, precursor material, shape and structure of the templates with highly ordered mesoporous templates yielding the highest surface area,.[54]

1.3.2. Blend and Copolymer Carbonization

Polymer blend carbonization involves the blending of thermally labile pore forming (sacrificial) polymer with carbon precursor, like PAN. The pore size and surface area of carbon materials prepared by blend carbonization for a variety of electrochemical applications varied depending on the sacrificial polymer, the carbon source, geometry of the carbon material like film, fiber and processing conditions.[58,59] The incompatibility or immiscibility of the components in polymer blends, need to be tailored such that they lead to micro-phase separation rather than macrophase separation.[60] During the thermodynamic-driven solvent induced phase separation of incompatible homopolymers, microphase separation is favored when the rate of the separation (kinetics) is altered due to processing parameters including the rate of removal of solvent causing difference in viscosity of the polymers.[61] Figure 1.1 depicts the phase diagram of incompatible blend of homopolymers (P1 and P2) systems upon the removal of common solvent (S), where

evolution of micro-phase separated morphology is favored due to an interplay of thermodynamic and kinetic factors. Point A in the figure represents the initial blend of two homopolymers in the solvent, with point B marking the removal of the solvent. Point C denotes the beginning of phase separation of the two polymers upon reaching critical concentration and point D denotes the curbing of an equilibrium macro phase separated morphology due to enhanced viscosity of the polymer components influenced by the rate of the solvent removal, thus, resulting in domain segregated morphology. Major component of the blends forms continuous phase while the minor component the dispersed phase. The morphology and the periodic size of the domains depends on factors including the rate of removal of solvent, the interaction between the polymers and the blend ratio.

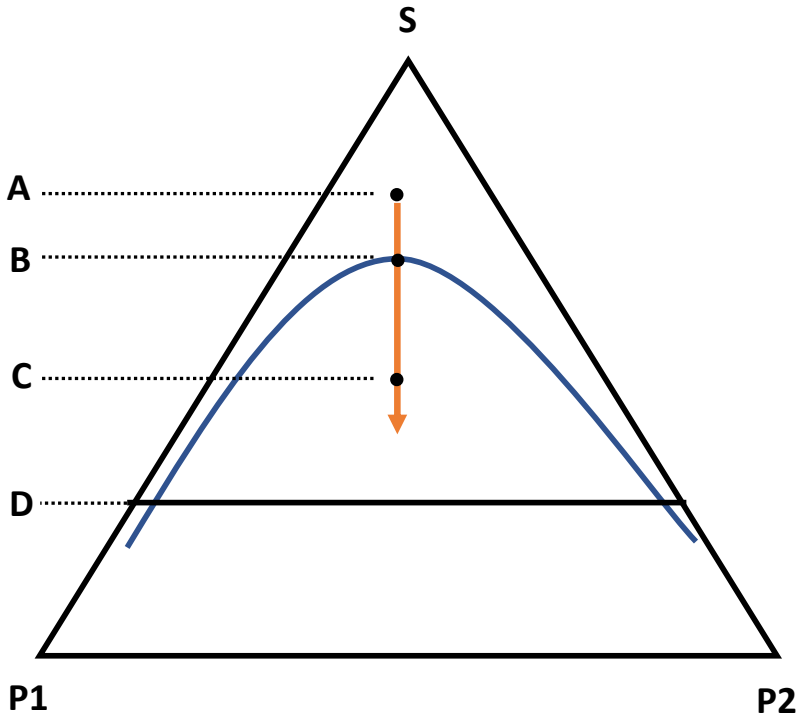

Figure 1.1. Schematic phase diagram of phase separation of blend of two immiscible homopolymers.[61]

Block copolymers have two or more monomers that are covalently bonded. Unlike in the case of blends of homopolymers where evolution of micro phase separated morphology needs an interplay of thermodynamic and kinetic factors, block copolymers are thermodynamically driven to self-assemble into varied micro-phase separated morphologies (cubic, hexagonal, gyroidal, lamellar) with short- or long-term order. These micro phase separated morphologies occurs due to the interplay of intrachain repulsive forces of incompatible monomers bound by covalent bond and interchain attraction of like monomers in the block.[46] In addition to the thermodynamically driven self-assembly, domains size and structure in such phase-separated morphologies are further

modified by molecular weight of monomers in the block, the fraction of the blocks in the copolymer and processing conditions.[62,63]

For polymer blends consisting of copolymer-homopolymer or copolymer-copolymer, microphase separation into varied self-assembled morphologies occurs due to two types of interactions at play: (a) repulsive interaction balanced by the covalent bonding between the incompatible polymer blocks in the copolymer and, (b) specific attractive interaction between the homopolymer and the common monomer of the copolymer.[64,65] The domain separated microphase morphology is dependent on the copolymer composition[66], blend ratio, molecular weight of the blend components[67], compatibility between the blend components (interaction parameters), rate and type of solvent removal (thermal, solvent or non-solvent induced). Porosity in the cases of blends and block-copolymers, is generated by burning off the dispersed micro-domains. Porosity and pore size distribution of fibers are effectively controlled by tailoring the morphology of the blend or block copolymer systems.

1.4. Asphaltenes

Asphaltene has been studied for its potential as a carbon fiber precursor, as mentioned earlier, owing to their lower cost when compared to PAN. This section provides some basic insights on asphaltenes. Asphaltenes have sometimes been defined by their solubility in toluene or by their insolubility in heptane or hexane. Previous literature proposed different structures for asphaltene.[68,69] The consensus is that asphaltenes are composed of polycyclic aromatic molecules in the core with aliphatic chains on the ends.

These aromatic molecules tend to stack up to form aggregates. Successful oil extraction and transport depends on preventing asphaltene precipitates from damaging piping and equipment by maintaining its solubility in crude oil.[70,71]

Asphaltenes were either melt-spun or solution-spun using toluene, and the resulting fibers were stabilized and carbonized.[72] Carbon fibers with (a) tensile strength in the range of 0.8 – 1.1 GPa were obtained by converting asphaltenes from coal-tar into mesophase pitch through pre-treatment followed by melt spinning and pyrolysis.[73,74] Melt spun coal derived asphaltene with styrene-ethylene-butylene-styrene, when carbonized at 1000 °C yielded carbon fibers with a tensile strength in the range of 0.6-1.1 GPa.[75] Solutions of asphaltene in toluene were electrospun to study their potential as membranes.[76] Asphaltenes were melt-spun, treated with nitric acid, stabilized, carbonized at 800 °C and activated to produce porous carbon fibers.[77]

1.5. Dissertation Objectives and Outline

The objective of this dissertation is to tailor high-performance carbon fibers for light weighting automobiles to achieve SDGs of clean energy, climate change and infrastructure. Two pathways of designing carbon fibers with the potential to replace steel/aluminum used in current day vehicles are elucidated. The first approach involves tailoring multifunctional porous and low-density (lightweight) carbon fibers using sacrificial polymer blends and block copolymers. The second path involves the exploration of alternate and cheaper precursors to PAN, specifically asphaltenes, for obtaining carbon fibers.

In Chapter 2, a potential pathway to synergistically impart structural integrity to the micro-phase separated porous morphology of carbon fibers through gel-spinning of PAN with sacrificial polymer blends was presented. From five different sacrificial polymers, three systems including (a) homopolymers poly(acrylic acid) (PAA), (b) poly(methyl methacrylate) (PMMA) and (c) copolymer poly(styrene-co-acrylonitrile)(SAN) were blended with PAN based on their degree of incompatibility and used as precursors to obtain porous carbon fibers. Differences in the mechanical, structural, porous morphology and pore size of the resultant carbon fibers due to the choice of sacrificial polymers were elucidated. Sacrificial polymer systems of PAN-PAA and PAN-PMMA yielded porous carbon fibers with mechanical properties closer to that of non-porous PAN based fibers. Porous carbon fibers derived from PAN-SAN in this chapter resulted in fibers with porous channeled morphology and decreased mechanical performance. In Chapter 3, a follow-up study to improve the tensile properties of porous morphology of carbon fibers from PAN- SAN blends were conducted. The role of PAN-SAN blend ratio in influencing the performance of the fibers was established.

The concept of structural energy storage materials was studied in Chapter 4. Series of porous carbon fibers were obtained through gel-spinning of di-block copolymer, PMMA-*b*-PAN. The parameters influencing the thermo-mechanical and structural properties of polymer blend fibers were studied. Further, the effect of carbonization temperature and application of tension on the morphological, mechanical and electrochemical properties of these carbon fibers was determined. A computational study was conducted to understand the thermodynamics of phase separated morphology of PMMA-*b*-PAN and its characteristic domain length/size. The thermodynamically

calculated domain size was then compared with the experimentally observed pore size in the carbon fibers.

In Chapter 5, the production of carbon fibers from gel-spun asphaltene precursors was explored. Conditions to obtain carbon fibers through functionalization of asphaltenes and blending them with PAN, were established. The mechanical and structural properties of the resultant precursor and carbon fibers were studied, thereby opening avenues to derive carbon fibers from low-cost precursors.

The key takeaways of the dissertation are summarized in Chapter 6. Future pathways and recommendations for development of these high-performance carbon fibers for sustainable applications are also presented.in Chapter 6.

CHAPTER 2. TOWARDS DESIGNING STRONG POROUS CARBON FIBERS THROUGH GEL SPINNING OF POLYMER BLENDS

This chapter is adapted from the following published work: Ramachandran, J. (dissertation author); Lu, M.; Arias-Monje, P. J.; Kirmani, M. H.; Shirolkar, N.; Kumar, S. Towards Designing Strong Porous Carbon Fibers through Gel Spinning of Polymer Blends. *Carbon.* **2021**, *173*, 724–735. https://doi.org/10.1016/j.carbon.2020.10.029

2.1. Introduction

Blending of polymers provides a straightforward route to utilizing the synergistic benefits of the individual components without synthesizing specialized block copolymers. Polymer blend carbonization to obtain porous carbon materials involves the blending of incompatible polymers that micro-phase separate into a) the matrix-forming, carbon source polymer and b) dispersed pore forming, sacrificial polymer. The precursor polymer blend fibers for the porous carbon fibers have conventionally been produced by electrospinning.[13,14] The precursor fibers are first, electrospun from polymer blends with PAN as the carbon source, then stabilized, and finally carbonized to create porous carbon fibers.[80–83] Porosity and pore size distribution of these fibers are effectively controlled by tailoring the morphology of the blend systems by varying factors including the choice of sacrificial polymer and blend ratio.[58,60] The enhancement in electrochemical performance of porous carbon materials prepared by polymer blend carbonization has been studied by varying the sacrificial polymer, the carbon source, geometry of the carbon material like film, fiber, and processing conditions.[59]

Despite the significant efforts and progress in tailoring the pore morphology and electrochemical performance of porous carbon fibers from electrospun fibers, the mechanical integrity of these fibers remains low. High tensile strength and modulus carbon fibers are obtained by gel spinning of PAN which allows for high polymer alignment in the precursor and graphitic ordering in the carbon fiber.[11] In addition to the improvement in mechanical properties, addition of nanofillers or polymers to the gel spun PAN precursors, renders multi-functionality to these fibers: PAN/CNT have improved the electrical conductivity; PAN/CNC and PAN/lignin provided ways for their sustainable manufacture; hollow carbon fibers from PAN/PMMA through tailoring of geometry have lowered densities.[41] Porous carbon fibers from gel spinning blends of PAN with sacrificial polymers is an unexplored pathway to add functionality to the mechanically strong fibers by tailoring the porosity and density.

To this end, we combine the phase separation of polymer blends in the micro/nano scale range with the gel-spinning technique to produce porous carbon fibers. Spinning the precursor fibers with uniform distribution of domains of the sacrificial polymer and drawing the precursor fibers will elongate and orient these domains along the length of the fiber. The oriented precursor fibers with elongated pores will create porous channels, due to the burn-off of the sacrificial polymer domains upon stabilizing and carbonizing. This way, the resulting carbon fibers are expected to possess pores on the surface as well as the hollow channel in the bulk, low density, and self-standing structure with mechanical integrity, as depicted schematically in Figure 2.1.

Porous carbon fibers from gel spun precursor blends of PAN with three different sacrificial polymers: (a) homopolymers poly(acrylic acid) (PAA), (b) poly(methyl

methacrylate) (PMMA) and (c) copolymer poly(styrene-co-acrylonitrile)(SAN) have successfully been made. Out of five different sacrificial polymer systems, the above mentioned three sacrificial polymers are selected based on their intermediate and higher degree of compatibility with PAN, by analyzing the UV-Vis transmittance (Table A.1 and Figure A.1). The effect that the processing factors, choice of sacrificial polymer and the blend ratio have on the structural, mechanical and thermal properties of the precursor fibers have been first evaluated. Then, the porous morphology, mechanical properties and structural characteristics of the carbon fibers have been elucidated and discussed. The variation in the pore sizes of the carbon fibers has been evaluated by studying the compatibility of sacrificial polymers with PAN through interaction parameters and viscosity.

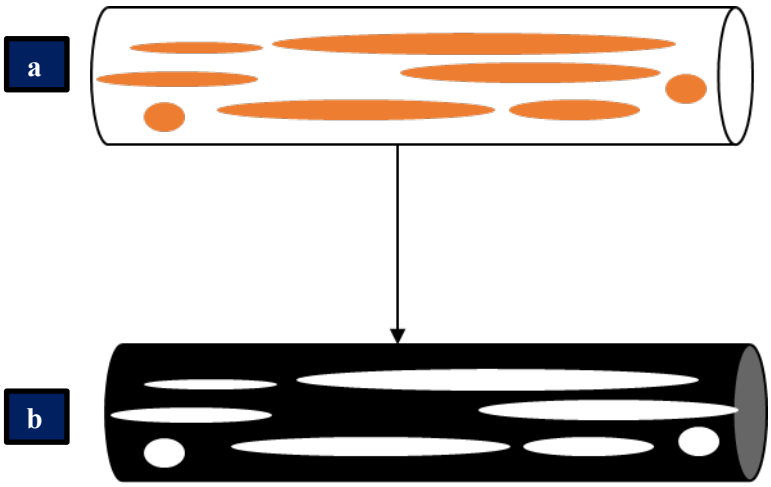

Figure 2.1. Schematics of the development of porosity in the blend starting from gel spun: (a) drawn and oriented precursor fiber, (b) carbon fiber. In (a) white areas, represent PAN while orange areas represent the sacrificial polymer. In (b) white areas represent the pores created by burning off the sacrificial polymer, and black areas represent carbon.

2.2. Experimental

2.2.1. Materials

Polyacrylonitrile-co-methacrylic acid (PAN; viscosity average molecular weight: 500,000 g/mol and 4 wt% methacrylic acid) was supplied by Japan Exlan, Co. Sacrificial polymers including polyacrylic acid (PAA; viscosity average molecular weight: 500,000 g/mol), polymethylmethacrylate (PMMA; viscosity average molecular weight: 350,000 g/mol) and styrene-co-acrylonitrile (SAN; viscosity average molecular weight: 165,000 g/mol; 25 wt% acrylonitrile), and the solvents dimethylacetamide (DMAc) and dimethylsulfoxide (DMSO) were obtained from Sigma Aldrich.

2.2.2. Preparation of blend solutions

PAN-sacrificial polymer blend solutions were prepared by dissolving PAN and sacrificial polymer, in their appropriate weight ratios (90/10) in DMAc such that the total solid content was 11 g/100 ml of DMAc. In the case of PAN-SAN (80/20) solution, PAN and SAN were dissolved in DMSO, maintaining the weight ratio of the blend to obtain a solution with total solid content of 11 g/100 ml of DMSO. The blend slurry in each case was continuously stirred at 70 °C for 3 hours until a visually homogenous spinning solution was obtained.

2.2.3. Spinning of blend fibers

The blend fibers were spun using a single filament line spinning equipment manufactured by Hills, Inc. The spinning solution was extruded through a spinneret with a diameter of 200 μm. The extrudate was passed through an air gap of 6 cm and then through either a cold or room temperature methanol coagulation bath. The as-spun fibers were collected on the take up-roller and stored in methanol overnight. The fibers were subsequently drawn at room temperature and then passed through a hot glycerol bath

maintained at temperatures between 160 and 165 °C. Table A.1 lists the processing parameters used for spinning the PAN-PAA, PAN-PMMA and PAN-SAN, blend fiber systems.

2.2.4. Stabilization and carbonization

Bundles of precursor fibers were stabilized and carbonized, under tension, in a tube furnace. During the two-step stabilization in an atmosphere of air, the precursor blend fibers exposed to a constant stress of 20 MPa, were first heated from room temperature to 265 °C at a heating rate of 3 °C/min, maintained at isothermal condition for 170 min and then heated to 305 °C at a heating rate of 3 °C/min and maintained at isothermal condition for 10 min. The stabilized fibers were then carbonized in an inert nitrogen atmosphere. The fibers were heated from room temperature to 1315 °C at a heating rate of 5 °C/min and maintained at isothermal condition for 10 min under a constant stress of 20-25 MPa, based on the overall diameter of the precursor fiber.

2.2.5. Characterization

Rheological behavior of the spinning solution was studied using an ARES Rheometer with parallel plate geometry (50 mm plate diameter and 1 mm gap between the plates) at room temperature. A constant strain of 1% (within the linear viscoelastic region) was applied and the angular frequency varied from 0.1 to 300 rad/s. Single filament tensile testing of the precursor blend fibers was done using a FAVIMAT$^+$ equipment at a strain rate of 1 %/s and a gauge length of 25 mm. At least 25 filaments were tested for each sample. Dynamic mechanical analysis (DMA) of precursor fibers was conducted on fiber bundles with an effective cross-sectional area of 55 μm^2 at a

frequency of 0.1 Hz using RSA III solids analyzer (Rheometric Scientific Co.) at a heating rate of 1 °C/min from 50 °C to 200 °C. Differential Scanning Calorimetry (DSC-TA Q200) was used to characterize the influence of sacrificial polymer on stabilization by heating the samples from 70 °C to 400 °C at different heating rates first in nitrogen atmosphere and then rerun in air. Single filament tensile testing of carbon fibers was done using FAVIMAT^{+} tensile tester and RSA III Solids Analyzer at a strain rate of 0.1 %/s and gauge length of 25 mm. The properties of carbon fibers from PAN-PAA were obtained by testing them on FAVIMAT while in the case of PAN-PMMA, the test could not be conducted on FAVIMAT as these fibers could not be clamped in their grips without loss of mechanical integrity. Instead, RSA Solids Analyzer III was used to conduct single-filament tensile test on carbon fibers from PAN-PMMA by mounting single filaments on paper tabs with one inch gauge length. Carbon fibers from PAN-SAN could not be tested using either of the methods listed above. The tensile modulus and strength were obtained from the individual stress-strain curves of the single fibers, based on overall cross section area of the fiber, as determined from fiber outer diameter. Specific tensile strength and modulus values were calculated using theoretically estimated carbon fiber densities. Carbon fiber volume fraction and density calculations are presented in Appendix B. The morphology of the carbon fibers was observed using a scanning electron microscope (HITACHI SU8230). The volume fraction of the porous channels in PAN-SAN system was obtained by analyzing the SEM images through the processing software, ImageJ. Wide-angle X-ray diffractions (WAXD) patterns were obtained on a Rigaku MicroMax 002 X-ray generator producing Cu Kα radiation (λ = 1.5418 Å, 50 kV and 0.6 mA), equipped with a R-axis IV++ detector. The crystal size of

PAN was calculated from the FWHM (full width at half-maximum intensity) of its crystalline peak from the equatorial scan using Scherrer's equation with k of 0.9. Raman spectra of the carbon fibers were collected on a Horiba Scientific Xplora confocal microRaman system (laser wavelength of 785 nm). The electrical resistance of single filament carbon fibers (minimum of 5 samples) was measured using Keithley 2400 source meter using a two-point probe geometry (the distance between the probes was varied between 6 and 20 mm and the current applied was 0.05 mA). Electrical conductivity was then calculated from measured electrical resistance, distance between the probes and overall cross-sectional area of fibers.

2.3. Results and Discussion

2.3.1. Selection of sacrificial polymer for spinning

To produce gel spun porous carbon fibers by carbonization of polymer blend, the first step is identifying suitable sacrificial polymers to blend with PAN. The degree of incompatibility between polymers in the blend dictated the pore size of carbon fibers obtained from them, with the lowest pore size obtained for the blends with highest compatibility.[60] Therefore, the degree of compatibility between two polymer components in the blend was experimentally discerned using UV-Visible spectroscopy. Polymer blend solutions of PAN were made with the five different sacrificial polymers as listed in Table A.2. The transmittance of the blend solutions in the visible region of the spectrum (400 – 700 nm) is lower than that of pure PAN solution (Figure A.1). The reduction in transmittance signifies immiscibility and poor interactions between the polymers. We

select three systems, namely PAN-PAA, PAN-PMMA and PAN-SAN, with intermediate and higher degree of compatibility with PAN, for gel spinning into fibers.

Four different precursor blend fibers, namely, PAN-PAA (90/10), PAN-PMMA (90/10), PAN-SAN (90/10) and PAN-SAN (80/20) were prepared, stabilized and carbonized to obtain porous carbon fibers. The solvent-coagulation pair for the PAN-SAN (80/20) was varied from the other three systems to evaluate if this variation caused difference in the porous morphology. We first look at the influence that the choice of the sacrificial polymers has on the properties of the precursor fibers and later study the resulting carbon fibers.

2.3.2. Rheological behavior of polymer blend spinning solutions

The complex viscosity plot and the rheological behavior of the spinning solutions are illustrated in Figure 2.2 and Figure A.3, respectively. Typical shear thinning behavior is observed for all the four blend solutions. Table 2.1 lists the viscosities of the blend solutions at room temperature and an angular frequency of 1 rad/s. The magnitude of viscosities of the 90/10 fiber systems, where the only varying parameter is the sacrificial polymer, follows the order: PAN-PAA< PAN-PMMA ~ PAN-SAN. The trend in the viscosities of the blend solutions can be qualitatively correlated with the compatibility between their constituent polymers as reported elsewhere.[84] Hence, the trend in compatibility as predicted from their viscosity is PAN-PAA< PAN-PMMA ~PAN-SAN. The trend of compatibility from the viscosity study is compared with compatibility deduced from thermodynamic interaction parameter and correlated to pore size of the carbon fibers, in the later part of this study. Table 2.1 summarizes the slopes obtained

from the modified Cole-Cole plot of the spinning solutions (Figure A.3). The plot indicates the homogeneity of the solution and a solution is considered homogenous if the slope is approximately 2.[85,86] Lower slope values represent lower degree of solution homogeneity. The data in Table 2.1 shows that solutions of PAN with the sacrificial polymers in DMAc is less homogeneous (slope values between 1.3 to 1.4) than in DMSO (slope value 1.5), pointing to better interaction of the two polymers in DMSO.

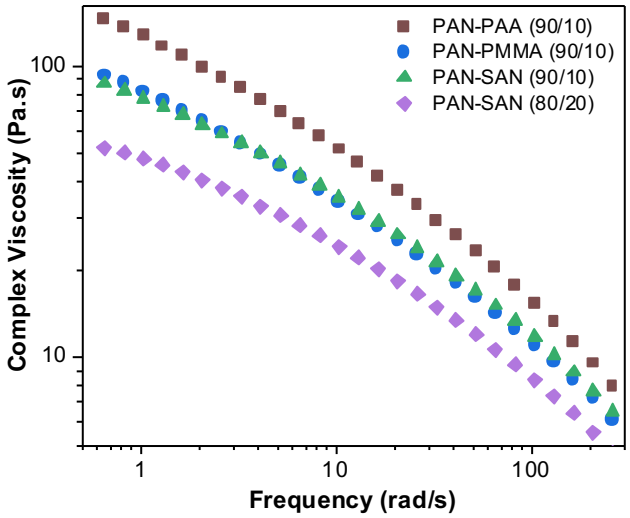

Figure 2.2. Plot of complex viscosity as a function of frequency for various spinning solutions.

Table 2.1. Summary of viscosities and slopes obtained from the modified Cole-Cole plots for spinning solutions.

	PAN-PAA (90/10)	PAN-PMMA (90/10)	PAN-SAN (90/10)	PAN-SAN (80/20)
Viscosity (Pa.s)	126	84	70	48
Slope Value	1.4	1.3	1.4	1.5

2.3.3. Tensile and structural properties of polymer blend precursor fibers

The mechanical properties of the PAN-PAA, PAN-PMMA and PAN-SAN precursor fibers are listed in Table 2.2. The drawability of the fibers is defined in terms of the total draw ratio, TDR, which is the combined elongation that has been imparted to the fibers during spinning, room temperature drawing and hot drawing. PAN-PAA (90/10) fibers have the lowest TDR among the precursor blend fibers compared. TDR of the PAN-PAA fibers could be limited due to the domain size and shape of the micro phase separated structure. Wang et.al observed that for micro phase separated blends, dispersed phase with higher domain size and lower viscosity had a higher degree of elongation of the dispersed phase, with their morphology changing from spherical droplets to ribbon-like structures.[87] Carbon fibers from PAN-PAA reveal non-elongated spherical pores that have average diameter of 15 nm unlike the elongated porous channels in the other two systems (> 30 nm) and show the highest viscosity, as discussed in the previous section. Correlating the trend between the pore size and shape of PAA with the highest molecular weight and viscosity among the other systems, it is hypothesized that non-elongated domains constrict the elongation of surrounding PAN matrix, limit the drawability of the precursor fibers and lead to PAN-PAA fibers with the lowest TDR. PAN-PMMA (90/10) precursor fibers have the highest tensile strength among all the blend systems compared. The tensile modulus of the 90/10 blend precursors is comparable to each other. Increasing the SAN content in the PAN-SAN system to 20% results in modest decrease of the tensile strength by 22% and in the tensile modulus by 16%.

Table 2.2. Mechanical properties of precursor blend fibers.

	PAN-PAA (90/10) (TDR 10)	PAN-PMMA (90/10) (TDR 13.5)	PAN-SAN (90/10) (TDR 17.1)	PAN-SAN (80/20) (TDR 15.6)
Diameter (μm)	19.7 ± 2.9	17.1 ± 3.3	15.1 ± 2.1	14.7 ± 2.3
Tensile Strength (MPa)	622 ± 35	803 ± 42	679 ± 29	528 ± 9
Tensile Modulus (GPa)	15.2 ± 0.4	15.5 ± 0.7	15.4 ± 0.3	13 ± 0.01
Elongation at Break (%)	11.4 ± 3.6	8.0 ± 0.2	7.1 ± 0.2	9.6 ± 0.2

*TDR: Total draw ratio

The integrated WAXD patterns for the 90/10 precursors (Figure 2.3a) produced in this study are similar, while the 80/20 fibers (Figure 2.3b-c) show an additional amorphous shoulder ~ 13º, that is attributed to the presence of SAN copolymer in the system.[88,89] Its emergence in just the PAN-SAN (80/20) fibers unlike the PAN-SAN (90/10) is due to the higher relative intensity of the peak with the increase in content of SAN. The structural parameters of the precursor blend fibers are listed in Table 2.3. The effects of inclusion of different sacrificial polymers in the PAN matrix and changing the blend ratio for SAN system are reflected in the crystallinity of the precursor fibers. PAN-PMMA fibers with the highest crystallinity among the blend systems, have the highest tensile strength. Changing the blend ratio from 90/10 to 80/20 in the PAN-SAN system decreased the crystallinity from 61 to 43%. PAN-SAN systems despite the higher draw ratio in comparison to PAN-PAA and PAN-PMMA have lower orientation. A plausible explanation behind this observation could be that the porous channels of SAN domains structurally hindered the orientation of the PAN crystals along the axis of the fiber.

Crystal structure of PAN is hexagonal when the $d_{17°}/d_{30°}$ =1.732 ($\sqrt{3}$) while a ratio > 1.732 or <1.732, indicates an orthorhombic crystal structure.[90,91] In our study, PAN-PAA (90/10) system with the ratio closest to 1.732 has a hexagonal crystal structure while the other three blend fibers have orthogonal crystal structures. The choice of the sacrificial polymer influences the crystal packing of PAN in the blend fibers.

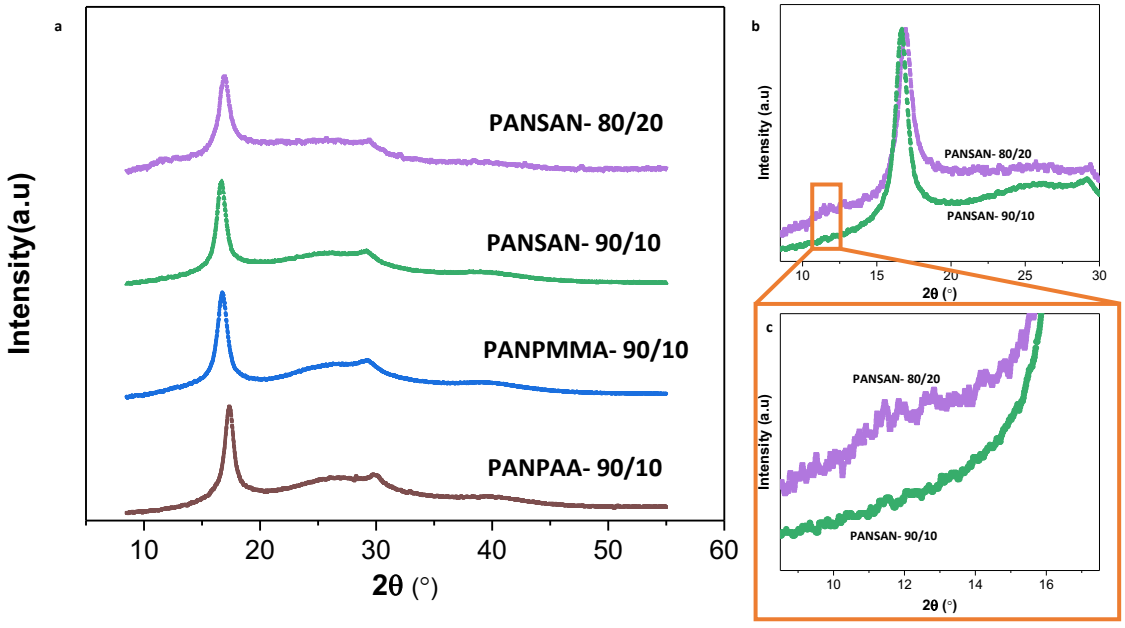

Figure 2.3. Integrated WAXD plots of precursor blend fibers (a) PAN-PAA (90/10), PAN-PMMA (90/10), PAN-SAN (90/10) and PAN-SAN (80/20); (b) and (c) Presence of peak ~13° in the integrated scan for PAN-SAN (80/20), and the absence of peak in PAN-SAN (90/10).

Table 2.3. Structural parameters of precursor blend fibers.

	PAN-PAA (90/10) (TDR 10)	PAN-PMMA (90/10) (TDR 13.5)	PAN-SAN (90/10) (TDR 17.1)	PAN-SAN (80/20) (TDR 15.6)
Crystallinity (%)[a]	54	64	61	43
Crystal size (nm)[b]	9.8	9.2	10.1	9.9
f_{PAN}[c]	0.83	0.84	0.76	0.70
$PAN_{2\theta meridional}$	38.7	39.1	39.5	38.7
$d_{17°}/d_{30°}$	1.729	1.740	1.739	1.714

[a] Crystallinity is calculated only with respect to the PAN crystal since the sacrificial polymers are amorphous
[b] Crystal size of PAN at $2\theta \approx 17°$ (200) and (110) planes
[c] Herman's orientation factor of PAN, calculated from the azimuthal scan of PAN (200) and (110) planes

DMA of the precursor blend fibers was done to corroborate the variation in the mechanical and structural properties of the fibers due to sacrificial polymer and the blend ratio. The storage modulus (Figure A.4a) at room temperature follows a similar trend, that the tensile modulus and the crystallinity of the precursor fibers have, thus reinforcing the consistency in the fiber properties. Despite the incompatibility of PAN and the sacrificial polymer in the blend, a single glass transition is observed due to the proximity of the glass transition temperatures of sacrificial polymers to PAN (Figure 2.4). The tan δ peak around 80 to 100 °C in PAN fibers denoted as β_c transition is representative of the molecular motion of helical sequences in the para-crystalline region.[92,93] The β_c peak temperature of the fibers reveal shifts with the choice of the sacrificial polymer and the blend ratio, with their values in the following order: 77 °C PAN-PMMA (90/10) < 86 °C PAN-PAA (90/10) ~ 88 °C PAN-SAN (90/10) < 95 °C PAN-SAN (80/20).

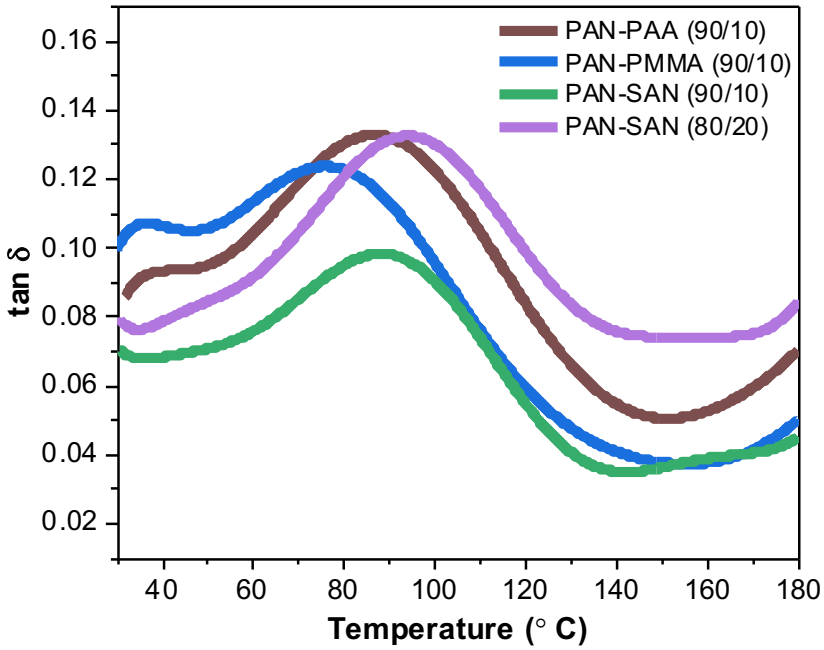

Figure 2.4. Temperature sweeps of tan δ, at a frequency of 0.1 Hz for the precursor blend fibers characterized by dynamic mechanical analysis.

Thermal stabilization of the PAN based precursor blend fibers is a crucial step in obtaining carbon fibers and hence, understanding the influence of the choice of sacrificial polymers on the reaction kinetics of these fibers is pertinent. The generally accepted scheme of reactions during oxidative stabilization include cyclization, oxidation, dehydrogenation and crosslinking, that concurrently occur leading to a thermally stable ladder polymer structure.[13,14,94] While cyclization reactions can be initiated in either oxidative or non-oxidative environment, oxidation reactions require the presence of oxidative environment.[95] This facilitates the study of individual reaction kinetics through DSC by, (i) first running the samples in nitrogen, where the exothermic peak is ascribed to cyclization, followed by (ii) rerunning the samples in air with the first exothermic peak

attributed to oxidation.[15,96–98] The activation energies of cyclization and oxidation are then, obtained using Eq.2.1 following Kissinger's method.[99]

$$-\frac{E_a}{R} = \frac{d\left(\frac{\emptyset}{T_P^2}\right)}{d\left(\frac{1}{T_p}\right)} \qquad (2.1)$$

where $\emptyset$, T_p, E_a, R are heating rate (°C/min), peak temperature (in Kelvin), activation energy, and universal gas constant (8.3415 J/mol.K) respectively. The activation energy obtained from the Kissinger's method (Eq.1) is further used to calculate the pre-exponential factor, A, and the reaction rate constants, k, according to Eq.2.2 and 2.3, respectively.[100]

$$A = \frac{\emptyset E_a}{RT_P^2} e^{\frac{E_a}{RT_p}} \qquad (2.2)$$

$$k = Ae^{-E_a/RT} \qquad (2.3)$$

The DSC plots of the precursor blend fibers at different heating rates in nitrogen and their rerun in air (Figure A.5) were used to obtain the plots (Figure A.6) for calculating the activation energies using Kissinger's method. The activation energies of cyclization and oxidation of the precursor blend fibers are compared in Figure 2.5 and their kinetic parameters are listed in Table A.3. From the variation in the kinetic parameters, it is evident that the choice of the sacrificial polymer in these blend fibers influence the stabilization reactions of PAN. The activation energies of cyclization of fibers with SAN (90/10 and 80/20) are higher than the PAA and PMMA fibers, which predominantly have acidic acrylic acid (AA) or neutral methyl methacrylate (MMA)

functional groups. AA and MMA moieties promote a ionic cyclization mechanism, which reduces the energy barrier for the initiation of the cyclization reactions as evidenced by their lower activation energy and reaction rate constants (Table A.3).[101–104]

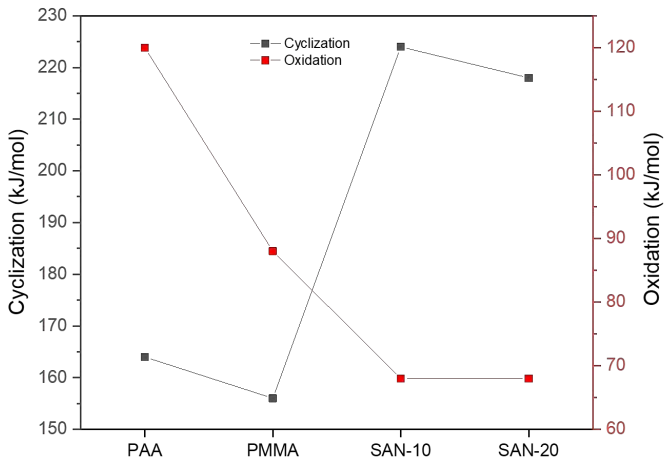

Figure 2.5. Influence of the choice of sacrificial polymers on the activation energies of cyclization and oxidation of the precursor blend fibers.

2.3.4. Morphological features of porous carbon fibers

Blend precursor systems in this study did not macro-phase separate into two distinct phases and instead formed phase separated domains in the nano/micro scale range, which upon stabilization and carbonization give rise to porous carbon fibers with different morphological features. The morphology of carbon fibers obtained from PAN-PAA (90/10) precursors are shown in Figure 2.6. The images show nearly circular and non-elongated pores with average pore diameter of 15 nm, as calculated using ImageJ analysis. Figure 2.7 shows elongated pores with average pore diameter of 31 nm

(analyzed using Figure 2.7b) in the carbon fibers made from PAN-PMMA (90/10). These pores do not appear to be interconnected but are oriented along the length of the fiber.

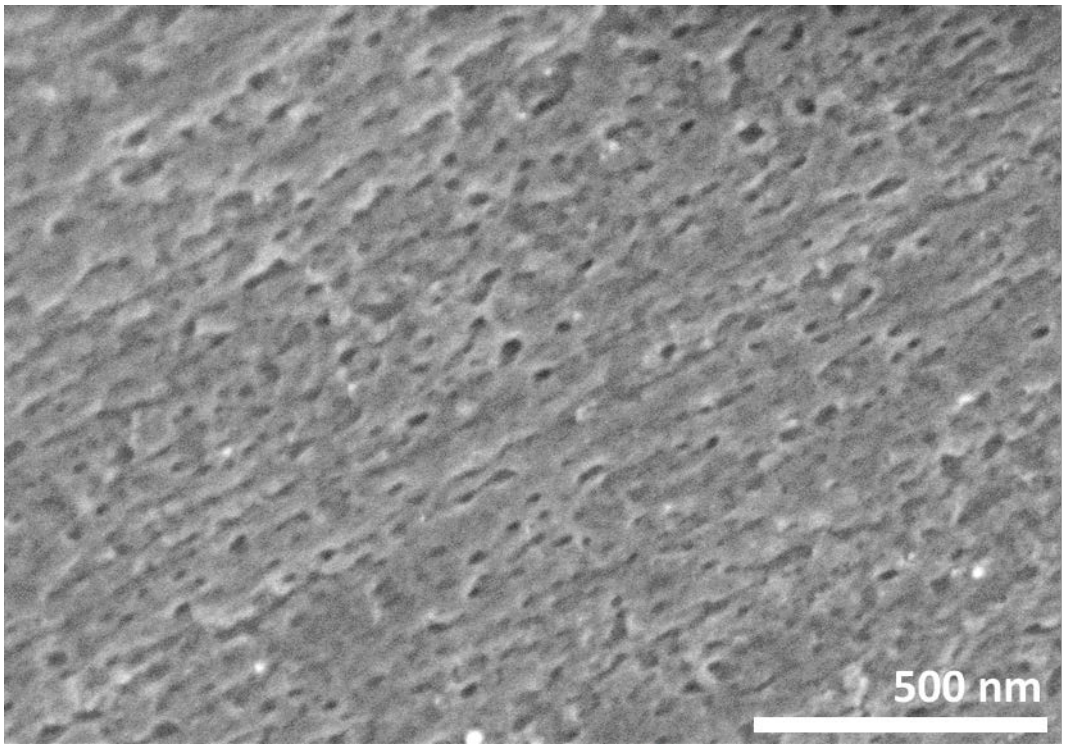

Figure 2.6. Morphology of nearly circular and non-elongated pores, with an average pore diameter of 15 nm found in carbon fibers from PAN-PAA (90/10) blend precursor.

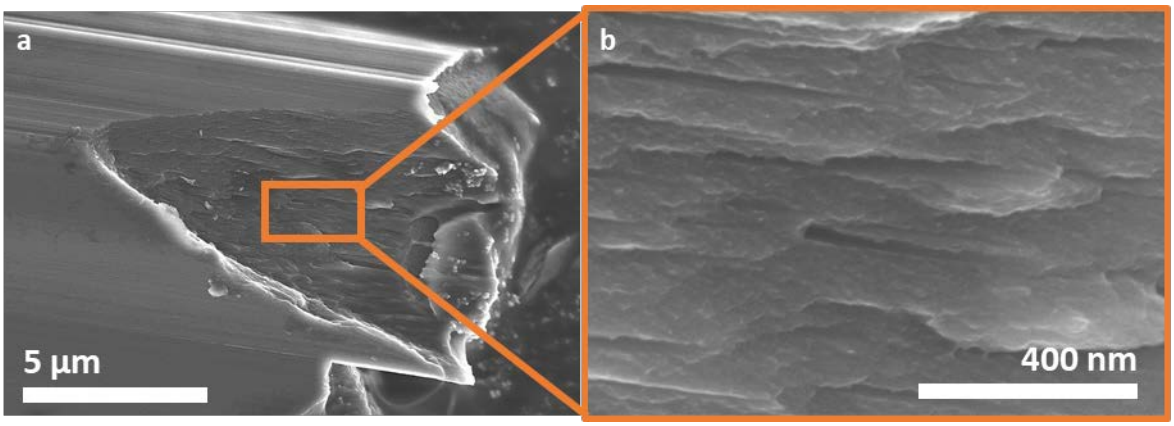

Figure 2.7. Morphology of carbon fibers from PAN-PMMA (90/10) blend precursor as represented through SEM images (a-b), with elongated pores having average pore diameter of 31 nm.

Carbon fibers from PAN-SAN (90/10) reveal elongated porous channels oriented along the fiber axis direction (Figure 2.8). The porous channels of these carbon fibers have an average pore diameter of 37 nm (calculated using Figure 2.8b-c). Porous channels are also present in the carbon fibers obtained from PAN-SAN (80/20) fibers and have an average pore diameter of 115 nm (calculated using Figure 2.9b). Increasing the composition of the sacrificial polymer in the blend here thus leads to an increase in the pore dimensions, which is consistent with the reports on carbon nanofibers made from blends.[58,78] The volume fraction of porous channels calculated from Figure 2.8b-c and Figure 2.9b using image analysis is 16% for the PAN-SAN (90/10) fibers and 36% for the PAN-SAN (80/20) system. The pore volume is also calculated using the rule of mixtures (Appendix B) and is 19% for the PAN-SAN (90/10) fibers and 34% for the PAN-SAN (80/20) system. The pore volume estimated using Figure 2.8b-c and Figure 2.9b is thus comparable (within experimental error) to the pore volume calculated using rule of mixtures.

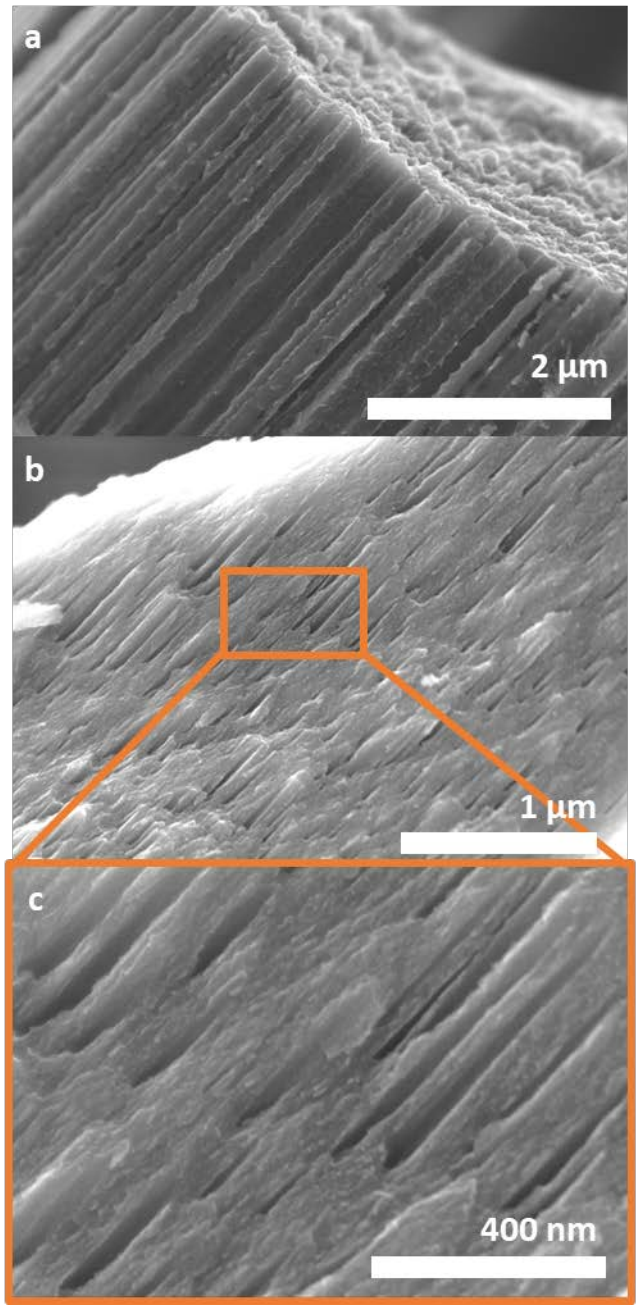

Figure 2.8. Morphology of elongated pores on carbon fibers from PAN-SAN (90/10) blend precursor imaged through SEM (a-c). Porous channels have an average pore diameter of 37 nm (b-c).

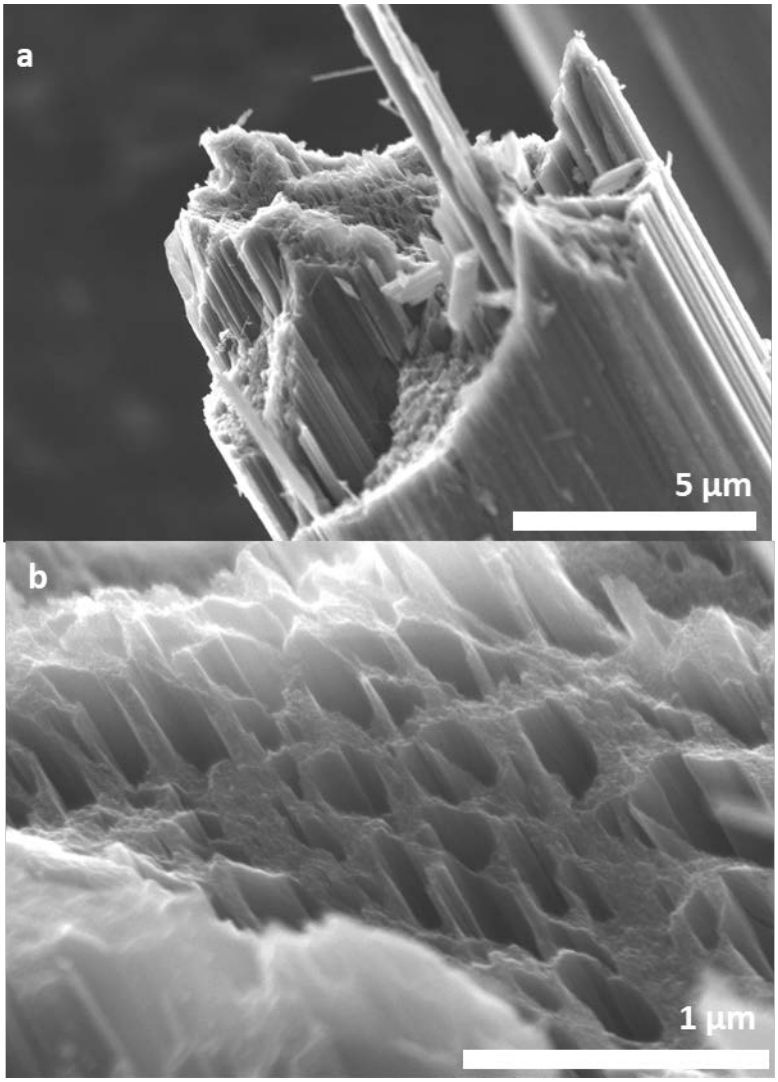

Figure 2.9. Porous channels with average pore diameter of 115 nm in the carbon fibers from PAN-SAN (80/20) blend precursors as represented through SEM images (a-b) at different magnifications.

The elongated porous channels in the PAN-PMMA and PAN-SAN system can be attributed to the elongation imparted during the gel spinning and drawing process as hypothesized in Figure 2.1. Previously, hollow carbon fibers with porous channels (seven channels) have been obtained by tailoring the geometry of the PAN precursor.[105] Literature studies report pores in the 2-10 micron range for carbon films made from PAN-SAN blend[106], non-elongated mesopores (2-50 nm) in carbon nanofibers

electrospun from PAN-SAN blends[107] and elongated porous channels with average pore diameter in the 2 -50 nm range in carbon nanofibers electrospun from PAN-SAN and PAN-PS blends.[108–112] However, in this study, we have achieved a porous channel morphology through by combining the incompatibility induced microphase separation in the PAN-SAN systems with the orientation imparted by the gel spinning process (Figure 2.10).

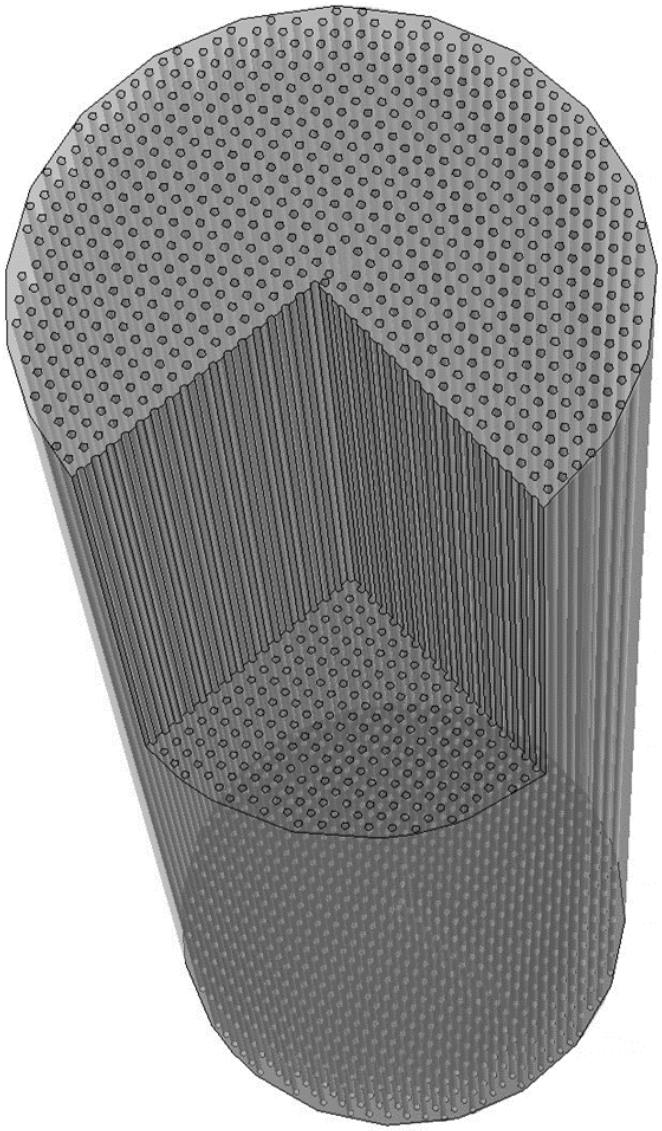

Figure 2.10. Schematic of porous channel morphology with pores oriented in the fiber axis direction.

The cross section of carbon fibers representative of the different blend fibers produced in this study are compared in Figure 2.11. The solvent-coagulation bath pair for PAN-SAN (80/20) fibers was varied from the 90/10 systems to study their influence on the morphology of the carbon fibers produced from them and we observed two features that were a result of this variation. The first feature observed is that the carbon fibers from PAN-SAN (80/20) blend (Figure 2.11d) have a circular cross-section in comparison

to the non-circular cross-section of the carbon fibers from 90/10 blends (Figure 2.11a-c). This difference in the cross sectional shapes of carbon fibers can be attributed to the temperature of coagulation bath, given that it is the only parameter that distinguishes the 80/20 fibers from the 90/10 systems in our study.[12] The second distinguishing feature is the presence of finger-like macro voids with average dimension of 1.9 μm in the carbon fibers from PAN-SAN (80/20) unlike the PAN-SAN (90/10) system. Carbon fibers revealed finger-like elongated macro voids when PAN[113] and PAN/Lignin blends[114] were spun using DMSO as the solvent owing to their instantaneous phase separation and diffusion during the coagulation process. Hence, the macro voids in the PAN-SAN (80/20) could be attributed to the differences in the choice of solvent (DMSO vs DMAc) used, rather than sacrificial polymer content.

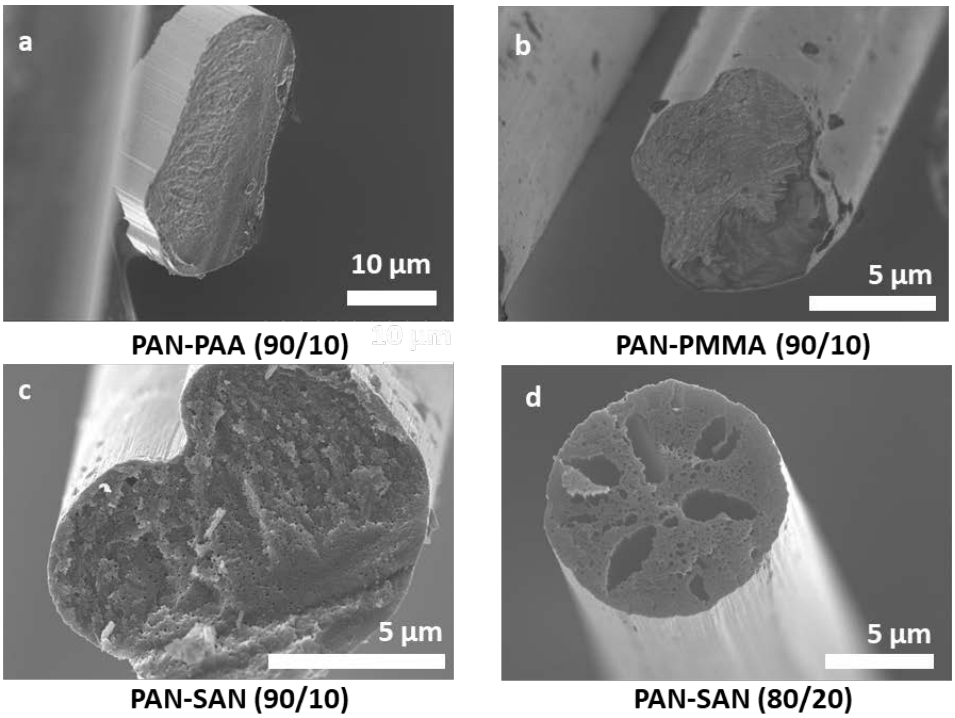

Figure 2.11. Cross-sectional morphology of carbon fibers from (a) PAN-PAA (90/10), (b) PAN-PMMA (90/10), (c) PAN-SAN (90/10), and (d) PAN-SAN (80/20).

2.3.5. *Effect of sacrificial polymer on the pore size*

The difference in size of the pores can be attributed to the compatibility between the two polymers in the blend by analysis of the thermodynamic-dependent interaction parameter and the kinetic-dependent solution viscosity. From the morphologies of carbon fibers discussed earlier, the size of the pores for PAN-PAA (90/10), PAN-PMMA (90/10) and PAN-SAN (90/10) are 15 nm, 31 nm and 37 nm, respectively. Jo et al. correlated the pore size of the carbon fibers obtained from polymer blends of PAN-sacrificial polymer to the difference in compatibility predicted through solubility parameters between polymers, while the blend ratio and processing conditions of the blend were kept constant.[60] Following the report, we estimate the compatibility of the PAN-sacrificial systems to evaluate the pertinence of such a correlation with the pore sizes of carbon fibers in our study.

The compatibility of PAN-sacrificial polymers in this study are estimated by calculating the interaction parameter between the component polymers using the solubility parameters, as illustrated by Krause using an approximate method given by Eq 2.4.[115]

$$\chi_{AB} = \frac{V}{RT}(\delta_A - \delta_B)^2 \qquad (2.4)$$

where V is reference volume (molar volume), R is universal gas constant, T is temperature, A and B refer to the two constituent polymers in the blend, δ is Hildebrand solubility parameter.

Simplifying the calculation for Eq 4 and using the following values: V = 100 cm^3/mol, R = 1.987 cal/ °mol, T = (273 + 25) °K, interaction parameter is given by Eq 2.5.

$$\chi_{AB} \approx \frac{1}{6}(\delta_A - \delta_B)^2 \qquad (2.5)$$

Finally, the critical interaction parameter defines the limit below which the polymer blend is compatible and, in the case, where $\chi_{AB} > (\chi_{AB})_{cr}$ the blends are incompatible.

$$(\chi_{AB})_{cr} = \frac{1}{2}\left(\frac{1}{n_A^{\frac{1}{2}}} + \frac{1}{n_B^{\frac{1}{2}}}\right)^2 \qquad (2.6)$$

n_A or n_B: Degree of polymerization approximately calculated as n = Molecular weight/ Volume (M_w/100).

Based on the equations 2.4 to 2.6, the interaction parameters calculated for the PAN-PAA, PAN-PMMA and PAN-SAN systems are given in Table 2.4. Individual solubility parameters are listed in Table A.4. The interaction parameter χ_{AB} for all the three systems are higher than their respective critical interaction parameters, indicating

that all the three polymer blends are incompatible. The degree of incompatibility in the three systems though is different due to the differences in solubility parameters of the corresponding polymers in the blend. The difference in the interaction parameter of PAN-PAA from its critical interaction parameter is lower than that for PAN-PMMA or PAN-SAN systems. This indicates that PAN-PAA is closer to the compatibility window, but still incompatible, while PAN-PMMA and PAN-SAN systems are farther removed from the compatibility window. Given the relatively lower magnitude of the interaction parameter (0.04 ($\chi_{PAN-PAA}$) < 1.08 ($\chi_{PAN-SAN}$) ~ 1.71 ($\chi_{PAN-PMMA}$)) and closeness to the compatibility window of PAN-PAA systems in comparison to the PAN-PMMA or PAN-SAN systems, the degree of incompatibility deduced through the thermodynamic interaction parameter is as follows: PAN-PAA < PAN-SAN ~ PAN-PMMA. The pore size in our study also follows the same trend as the degree of incompatibility. The compatibility of the polymer blends predicted by viscosity study of the spinning solutions, earlier in this study (PAN-PAA < PAN-SAN ~ PAN-PMMA) match the trend as deduced from the thermodynamic interaction parameters. Thus, during the evolution of phase domains for the PAN-sacrificial polymer upon phase separation, both the factors, i.e. thermodynamics and kinetics (viscosity) play a role. For the PAN-PAA system, the compatibility predicted by the interaction parameter and the viscosity is the lowest and hence they reveal pores of the lowest size viz. 15 nm. While in case of the PAN-PMMA and PAN-SAN systems with comparable viscosities and interaction parameters, they result in similar domain sizes (31 and 37 nm respectively). Thus, pore size of the carbon fibers obtained from gel-spun polymer blends can be qualitatively predicted by the degree

of incompatibility, discerned through experimental study of viscosity in addition to theoretical approach of the interaction parameter.

Table 2.4. Interaction parameter and the critical interaction parameter calculated for various blends.

	χ_{AB}	$(\chi_{AB})_{cr}$	Δ_{χ} $\chi_{AB} - (\chi_{AB})_{cr}$
PAN-PAA	0.04	0.007	0.03
PAN-PMMA	1.71	0.007	1.70
PAN-SAN	1.08	0.007	1.07

2.3.6. Tensile and structural properties of porous carbon fibers

The mechanical properties of the carbon fibers from PAN-PAA (90/10) and PAN-PMMA (90/10) blends are listed in Table 2.5. Carbon fibers from these blend fibers possess tensile strength and tensile modulus of ~1.6 GPa and 280 GPa, respectively. The tensile strength and specific tensile strength of the carbon fibers from the control PAN precursor, processed under similar conditions, are comparable to the values for the carbon fibers obtained from PAN-PAA and PAN-PMMA blends in this study (Table 2.5).[116] The porous carbon fibers have specific modulus that is 19 to 40 % higher due to the decrease in density from the introduction of porosity, and due to higher graphitic order as discussed elsewhere. The presence of pores in the carbon fibers from PAN-PAA and PAN-PMMA does not result in a decrease in strength. It is noted that the modulus values have relatively large error bars. Future work, where fibers from blends are processed in multifilament tow, and when the stabilization and carbonization of the multifilament tow is done on a continuous carbonization line, should result in lower error bars in the

modulus values. These studies will further clarify the mechanical property benefits of the polymer blends approach for making carbon fibers.

Table 2.5. Mechanical properties of carbon fibers from various precursors, as listed.

	PAN-PAA (90/10)	PAN-PMMA (90/10)	PAN [116]	PAN [117]
Diameter (μm)	10.5	9.4	7.7	8.2
Tensile Strength (GPa)	1.7 ± 0.3	1.5 ± 0.3	1.9 ± 0.4	2.1 ± 0.3
Tensile Modulus (GPa)	287 ± 48	281 ± 22	251 ± 27	288 ± 9
Specific Strength (N/tex)	1.2 ± 0.2	1.2 ± 0.2	1.1 ± 0.2	1.2 ± 0.2
Specific Modulus (N/tex)	197 ± 33	192 ± 15	141 ± 15	162 ± 5
Elongation at Break (%)	0.6 ± 0.07	0.5 ± 0.06	0.7 ± 0.1	0.8 ± 0.1

Blend ratio and the choice of sacrificial polymer has a predominant effect on the mechanical properties of the carbon fiber, as observed in the case of PAN-SAN. The mechanical strength of carbon fibers from PAN-SAN (90/10) and PAN-SAN (80/20) could not be experimentally tested due to their poor mechanical integrity, which prevented them from being clamped on the grips of the FAVIMAT or mounted on paper tabs to be tested on the RSA. The morphology of the carbon fibers from PAN-SAN show that these fibers have porous channels, unlike the other two sacrificial polymer systems. The loss in mechanical integrity of these fibers can be attributed to the variation in their porous morphology.

Figure 2.12 depicts the 2D images and equatorial WAXD scan of these carbon fibers. Carbon fibers from all the four precursor systems have similar equatorial patterns

with the prominent equatorial peak approximately at 26°, corresponding to the (002) peak of carbon structure. The structural parameters of carbon fibers are listed in Table 2.6. Noticeably, carbon fibers from PAN-PMMA (90/10) have lower d-spacing among all the fibers compared, pointing to more densely packed planes than the rest. The Raman spectra of carbon fibers from different precursor blends are given in Figure A.7. I_D/I_G ratio of the carbon fibers, which is a ratio of the defects (D-band at ~1330 cm^{-1}) to the graphitized plane (G-band at ~1560 cm^{-1}) in the structure, is evaluated for all the fibers. While the carbon fibers from blend precursors have comparable ratios, they are lower than the ratio of the carbon fibers obtained from control PAN. Hollow carbon fibers revealed higher graphitic ordering on the interior and exterior walls of the porous channels.[105] Corroborating the above results to the porous carbon fibers in this study, their lower I_D/I_G ratios (1.34 in PAN-PMMA and 1.67 in PAN-PAA) in comparison to the nonporous carbon fibers (I_D/I_G ratio of 2.5) as listed in Table 6, is attributed to the higher graphitic ordering. These lower I_D/I_G ratios also result in higher electrical conductivities of these two fibers (Table A.5). Despite comparable orientation values, PAN-PAA and PAN-PMMA based carbon fibers exhibit higher specific modulus than PAN based carbon fiber (Table 2.5), and this is attributed to the higher graphitic order in the former two fibers.

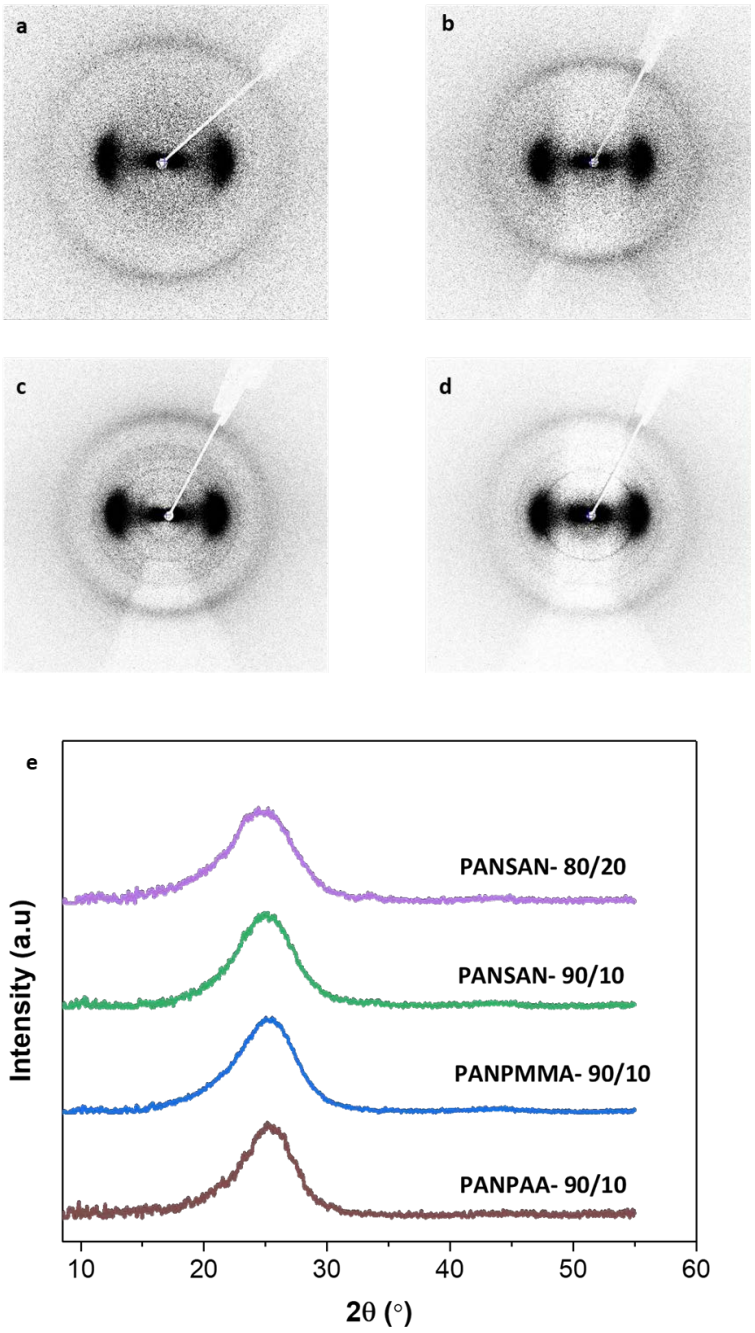

Figure 2.12. 2D WAXD images of carbon fibers from blend precursors: (a) PAN-PAA (90/10), (b) PAN-PMMA (90/10), (c) PAN-SAN (90/10), and (d) PAN-SAN (80/20). (e) Equatorial WAXD plots.

Table 2.6. Structural parameters of carbon fibers from various precursors, as listed.

	PAN-PAA (90/10)	PAN-PMMA (90/10)	PAN-SAN (90/10)	PAN-SAN (80/20)	PAN [116]
L002 (nm)[a]	1.67	1.96	1.46	1.56	1.36
L10 (nm)[b]	1.86	1.79	1.23	1.93	1.98
f_{002}[c]	0.76	0.75	0.74	0.74	0.75
d-spacing (nm)[d]	0.355	0.348	0.358	0.356	0.356
I_D/I_G	1.67 ± 0.24	1.34 ± 0.01	1.76 ± 0.08	1.77 ± 0.23	2.5 ± 0.20

[a and b] Crystal size of (002) plane at 2θ ~ 26°, and (10) plane at 2θ ~ 43°, according to Scherrer's equation with K = 0.9.
[c] Orientation factor of (002) plane.
[d] d-spacing of (002) plane at 2θ ~ 26°.

2.4. Conclusion

Blends of PAN with sacrificial polymers PAA, PMMA and SAN are successfully gel-spun, stabilized and carbonized to obtain porous carbon fibers. The factors influencing the porous morphology, mechanical and structural integrity of the precursor blend fibers processed through gel spinning and the resultant carbon fibers are studied. In terms of the precursor fibers, the choice of the sacrificial polymer and the blend ratio influences the viscosity, draw ratio, tensile strength, crystallinity and crystal-packing structure. The choice of the sacrificial polymer alters the activation energies of cyclization and oxidation affecting the thermal stabilization reaction kinetics. The carbon fibers from three sacrificial polymer systems reveal the following porous morphologies: PAA- nearly circular and non-elongated pores; PMMA: elongated pores; SAN- porous channels. The average pore diameter in carbon fibers obtained from PAN-PAA (90/10),

PAN-PMMA (90/10) and PAN-SAN (90/10) are 15 nm, 31 nm and 37 nm, respectively. Degree of compatibility between the polymer components in the blend is evaluated through experimental viscosity study and theoretical study of interaction parameters. Increasing the blend ratio in the PAN-SAN fiber system from 10 wt% to 20 wt%, lead to increase in the pore size from 37 nm to 115 nm. Despite the introduction of pores, carbon fibers from PAN-PAA (90/10) and PAN-PMMA (90/10) have tensile strength (~1.6 GPa) and tensile modulus (~280 GPa) closer to that of the carbon fibers obtained from PAN (~2.0 GPa and ~270 GPa) processed under comparable conditions. Specific modulus of PAN-PAA and PAN-PMMA based carbon fibers is up to 15 to 40 % higher than the comparably processed PAN based carbon fiber, and the electrical conductivity is as high as 74 kS/m. Using the polymer blends approach to exploit the porous channel morphology presented in carbon fibers, through gel spinning, should be considered a prototype that can be explored further towards designing low-density, porous carbon fibers with good mechanical integrity.

CHAPTER 3. IMPROVING MECHANICAL PERFORMANCE OF POROUS CARBON FIBERS FROM PAN-SAN BLENDS

3.1. Introduction

In Chapter 2, we successfully elucidated the concept of synergistically combining the gel-spinning of poly(acrylonitrile) (PAN) based polymer blends with the microphase separation of polymer pairs, to design structurally strong porous carbon fibers. Porous carbon fibers from gel-spun poly(acrylonitrile)-poly(acrylic acid) PAN-PAA (90/10) and poly(acrylonitrile)-poly(methyl methacrylate) PAN-PMMA (90/10) had comparable specific strength and 15-40% higher specific modulus than that of the non-porous PAN derived fibers.[118] Porous morphology exhibited by the PAN-PAA and PAN-PMMA derived carbon fibers were non-elongated and elongated pores, respectively. Interestingly, carbon fibers from poly(acrylonitrile)-poly(styrene-*co*-acrylonitrile) PAN-SAN blends (80/20 and 90/10) had a porous channel morphology, that sets it apart from the other two systems. On the other hand, this unique morphology greatly impaired the mechanical performance of these PAN-SAN derived porous carbon fibers. It was concluded that the prototype of the porous morphology revealed by PAN-SAN needed to be further studied and ways to improve their mechanical properties pondered upon.

SAN, a random copolymer, has been used in prior studies to design hollow and porous fibers for electrochemical energy storage (electrode materials, electrocatalysts) and desalination membranes.[106,119–125] Uniform hollow carbon fibers for synthesizing electrode materials were coaxially electrospun with SAN and PAN in the core and sheath,

respectively.[126,127] SAN was specifically used in these studies due to their incompatibility with PAN, co-axial spinnability and thermal stability until certain stage of pyrolysis. Hollow carbon fibers with porous sheath derived from PAN-SAN (75/25) blend were electrospun to improve the electrochemical performance for application in lithium-ion batteries.[112] Mesoporous (2-50 nm) morphology rendered by SAN in these porous fibers aid in the diffusion of ions, accommodate volume changes during electrochemical cycling and can be used both as cathode and anode materials.[128] PAN-SAN blend systems have been extensively studied in the literature for their electrochemical performance and our earlier study (Chapter 2) was the first to gel-spun precursors from them. Nevertheless, the mechanical performance of the porous carbon fibers from PAN-SAN blends could not be studied.

From the knowledge gained through earlier studies, we hypothesized that decreasing the SAN content in the PAN-SAN polymer blend, would retain the porous morphology without degrading the mechanical performance. To this effect, we gel-spun PAN-SAN (95/5) blend precursor fibers and compared their performance with fibers having higher content (10 and 20 wt%) of SAN. Then four different porous carbon fibers were produced from these precursor blend fibers by varying the pyrolysis conditions. We studied the porous morphology, mechanical and structural performance of these fibers. Our hypothesis of improving the mechanical performance of PAN-SAN fibers with their unique porous morphology was proven successful. Thus, we were able to expand on the idea of strong and lightweight porous carbon fiber prototypes from gel-spun PAN-SAN blends. This work could prove impactful in the area of structural energy storage, desalination and more.

3.2. Experimental

3.2.1. Materials

Poly(acrylonitrile-*co*-methacrylic acid) (PAN; viscosity average molecular weight, M_v: 500,000 g/mol; 4 wt% copolymer) was obtained from Japan Exlan, Co. Sacrificial polymer, poly (styrene-*co*-acrylonitrile) (SAN; weight average molecular weight, M_w: 165,000 g/mol; 25 wt% acrylonitrile), and the solvent dimethylacetamide (DMAc) were obtained from Sigma Aldrich.

3.2.2. Spinning of precursor fibers from blend solution

A PAN: SAN blended powder (11 g; 95:5 by weight ratio) was first added to 100 mL of pre-chilled (~ 0 C°) DMAc. Slurry of PAN-SAN in DMAc was then heated to 70 °C using a silicone oil bath. The spinning solution was obtained after continuous stirring of the heated blend slurry for 3 hours. PAN-SAN (95/5) fibers were spun using a single filament spinning equipment manufactured by Hills, Inc. The spinning solution was extruded through a spinneret with a diameter of 200 μm. The extrudate was passed through an air gap of 6 cm and then through a -50 °C methanol coagulation bath. The as-spun fibers with a spin draw ratio (SDR) of 3 were collected on the take up-roller and stored in methanol overnight. The fibers were subsequently drawn at 160 °C by passing through a glycerol bath, with a hot draw ratio of 4.5. Drawn fibers with total draw ratio of 13.5 (TDR= SDR*HDR) are referred to as the precursor blend fibers.

3.2.3. Stabilization and carbonization of precursor blend fibers

Bundles of precursor fibers were stabilized and carbonized, with and without the application of tension, in a tube furnace. Fibers were stabilized in air by heating them from room temperature to 265 °C (heating rate, 3 °C/min) for 170 min, then heated to 305 °C (heating rate ,3 °C/min) for 10 min. Two sets of stabilization conditions were used: (a) fibers were constrained and allowed 30% shrinkage and (b) 20 MPa tension was applied on the fibers. The stabilized fibers were further carbonized in nitrogen, by heating to 800°C or 1315 °C (heating rate, 5 °C/min) for 10 min, both with and without tension. For the fibers carbonized with tension, a constant stress of 20 MPa was applied. The stress applied was calculated based on the overall cross-sectional area of the precursor blend fiber.

3.2.4. Characterization

Rheology of the spinning solution was characterized using an ARES Rheometer with parallel plate geometry (50 mm plate diameter and 1 mm gap between the plates) at room temperature. A constant strain of 1% (within the linear viscoelastic region) was applied and the angular frequency varied from 0.1 to 300 rad/s. Single filament tensile testing of the precursor blend fibers was done using a FAVIMAT$^+$ equipment at a strain rate of 1 %/s and gauge length of 25 mm (atleast 25 filaments were tested). RSA III Solids Analyzer was used to test the tensile properties of single filament porous carbon fibers by mounting them on paper tabs of gauge length 12.7 mm and a strain rate of 0.1 %/s. Tensile strength and modulus were then calculated from the stress-strain curves of the single filaments based on the overall cross-sectional area. Surface and cross-sectional morphologies of the porous carbon fibers were imaged on a HITACHI SU8230 scanning electron microscope (SEM) with an accelerating voltage of 2 kV and at working

distances of 5-10 mm. The density of the porous carbon fibers was calculated to be 1.59 g/cm^3 for all the PAN-SAN (95/5) porous fibers (carbonized at 800 °C and 1315 °C), using a reference density of IM7 carbon fiber. The calculation and the associated assumptions are elucidated in Appendix B. Wide-angle X-ray diffractions (WAXD) patterns were obtained on a Rigaku MicroMax 002 X-ray generator producing Cu Kα radiation (λ = 1.5418 Å, 50 kV and 0.6 mA), equipped with a R-axis IV++ detector. The crystal size of PAN was calculated from the FWHM (full width at half-maximum intensity) of its crystalline peak from the equatorial scan using Scherrer's equation with K of 0.9. Raman spectra of the carbon fibers were collected on a Renishaw Qontor Dispersive Raman Spectrometer (λ = 785 nm).

3.3. Results and Discussion

3.3.1. Properties of precursor blend solution and fiber

Viscosity of PAN-SAN (95/5) blend solution at room temperature and 1 rad/s was 79 Pa.s (Figure C.1), comparable to PAN-SAN (90/10) (70 Pa.s) and higher than PAN-SAN (80/20) (48 Pa.s) solutions. Decreasing the amount of SAN to 5 wt% improved the compatibility of the PAN-SAN polymer pairs in the blend, as qualitatively predicted by measuring the viscosity of the blend solutions.[118]

The effect of changing the blend ratio of PAN-SAN on the mechanical and structural performance of the precursor blend fibers was studied (Table 3.1). The TDR of the three fiber systems were compared without including the cold drawing treatment received by PAN-SAN (90/10) and PAN-SAN (80/20). PAN-SAN (95/5) precursor fibers had marginally higher draw ratio but the diameter of all the three systems were similar.

While the tensile strength of PAN-SAN (95/5) and PAN-SAN (90/10) were comparable, the precursor fibers with 20 wt% SAN had lower tensile strength. Decreasing the amount of SAN in the precursor blend fibers from 20 wt% to 5 wt%, increased the tensile modulus by 22%. Tensile modulus of PAN-SAN (95/5) fibers was marginally higher compared to the PAN-SAN (90/10) fibers. The influence of changing the blend ratio of PAN-SAN fibers on the tensile properties was more significant upon a 15 wt% decrease rather than 5 wt%.

WAXD integrated plot of the PAN-SAN (95/5) precursor blend fibers exhibited only the two characteristic peaks (~17° and 30°) of PAN (Figure C.2). Crystal size and orientation factor of the PAN-SAN precursor blend fibers followed the trend: PAN-SAN (95/5) > PAN-SAN (90/10) > PAN-SAN (80/20), in alignment with the tensile modulus. The packing of PAN crystals is elucidated by comparing the $d_{17^\circ}/d_{30^\circ}$ ratio of the fibers. PAN-SAN (95/5) with the highest PAN content among the fibers compared, had a $d_{17^\circ}/d_{30^\circ}$ ratio closer to that of the hexagonal crystal structure of PAN ($d_{17^\circ}/d_{30^\circ} \sim 1.732$).[91,93] Thus, PAN-SAN (95/5) precursor blend fibers with higher amount of PAN showed characteristics of the major component of the blend.

Table 3.1. Mechanical and structural properties of precursor PAN-SAN blend fibers.

	PAN-SAN (95/5)	PAN-SAN (90/10) [118]	PAN-SAN (80/20) [118]
TDR*	13.5	11.4	12
Diameter (μm)	14.7 ± 2.1	15.1 ± 2.1	14.7 ± 2.3
Tensile Strength (MPa)	734 ± 21	679 ± 29	528 ± 9
Tensile Modulus (GPa)	15.9 ± 0.2	15.4 ± 0.3	13 ± 0.01
Elongation at Break (%)	7.6 ± 0.6	7.1 ± 0.2	9.6 ± 0.2
Crystallinity (%)[a]	61	61	43
Crystal size (nm)[b]	11.7	10.1	9.9
f_{PAN}[c]	0.82	0.76	0.70
$d_{17°}/d_{30°}$	1.729	1.739	1.714

*TDR: Total draw ratio

[a] Crystallinity is calculated only with respect to the PAN's crystalline peaks (Figure C1 shows the peak fitting)

[b] Crystal size of PAN at $2\theta \approx 17°$ (200) and (110) planes, calculated using Scherrer's equation from the equatorial scan with K=0.9.

[c] Herman's orientation factor of PAN, calculated from the azimuthal scan of PAN (200) and (110) planes

3.3.2. Morphology of porous carbon fibers

We produced four different porous carbon fibers by varying the pyrolysis conditions namely: 800 °C with and without tension; 1315 °C with and without tension. Porous morphology of these four different carbon fibers was comparable (Figures 3.1-3.4). The cross-section of all the fibers were non-circular, like the carbon fibers from PAN-SAN (90/10) fibers spun using the same solvent DMAc.[118] Pores were well distributed across the cross-sections of the fibers in all the four cases. Pores on the

surface and the bulk were axially aligned and elongated. Unique porous channel morphology exhibited by PAN-SAN (90/10) and PAN-SAN (80/20) systems in Chapter 2 was observed in PAN-SAN (95/5) fibers as well. Average pore size of the four different PAN-SAN (95/5) derived carbon fibers was calculated to be ~27 nm, except for fibers carbonized at 1315 °C without tension that resulted in 41 nm (Figure 3.5). Nevertheless, given the large standard deviation in the pore sizes of these fibers, we can conclude that they are comparable irrespective of the application of tension or not and the temperature of carbonization. For comparison, carbon fibers from PAN-SAN (90/10) precursor blend had an average pore size of 37 nm, while PAN-SAN (80/20) fibers exhibited an average size of 115 nm.[118] Decreasing the amount of SAN from 20 to 5 wt% had a larger impact on the reduction of pore size (factor of ~4.4) when compared to the decrease from 10 to 5 wt% (factor of ~1.4). In Chapter 2, we established that the viscosity of blend solutions that indicated compatibility was inversely proportional to the pore size.[118] The inverse relationship between viscosity of PAN-SAN blend solutions with 5, 10 and 20 wt% SAN and their pore size was proven true: Viscosity of PAN-SAN (95/5) ~ PAN-SAN (90/10) > PAN-SAN (80/20), and the pore size of PAN-SAN (95/5) ~ PAN-SAN (90/10) < PAN-SAN (80/20.

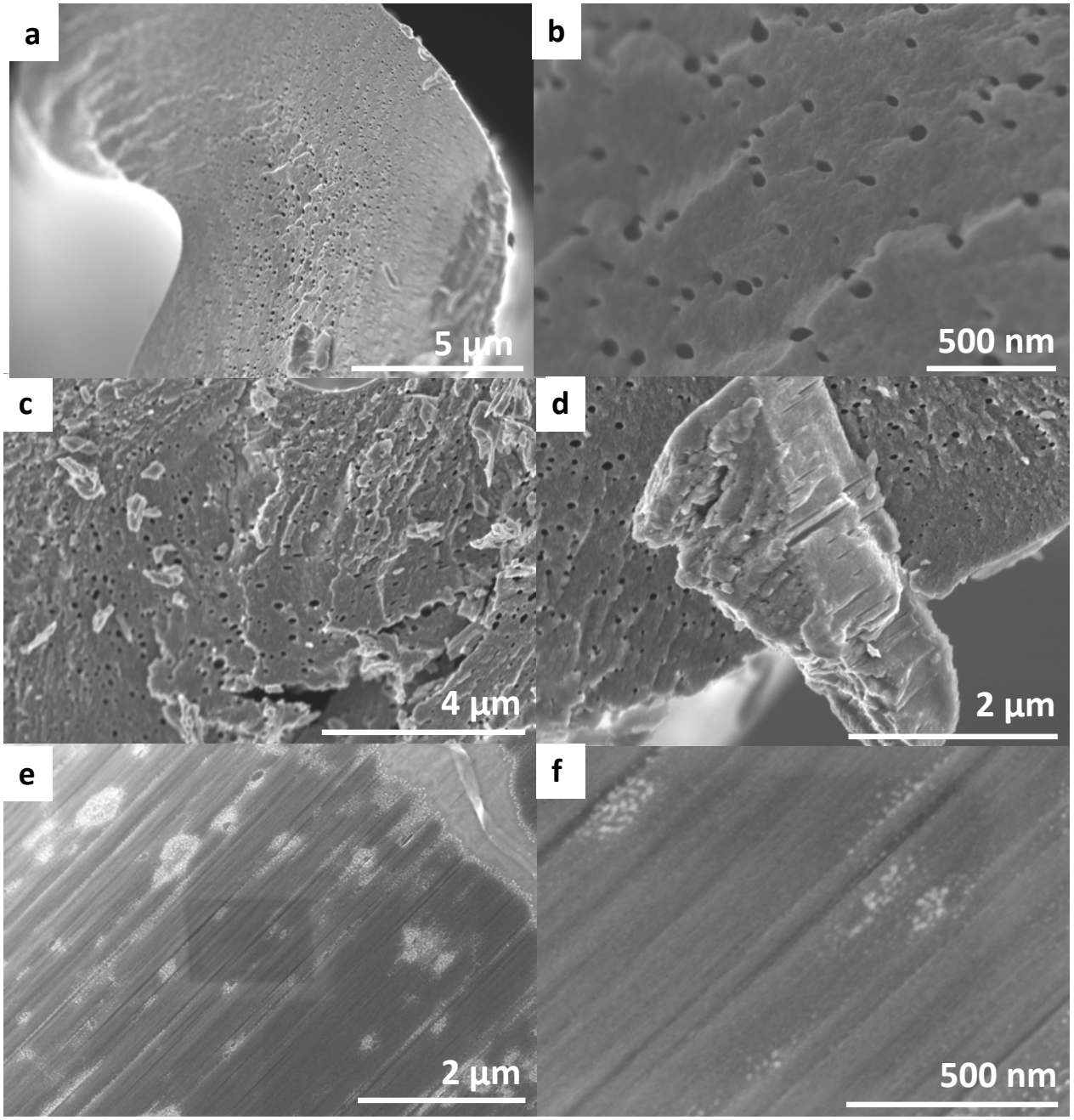

Figure 3.1. Representative SEM images of carbon fiber cross-section (a-d) and surface (e-f), carbonized at 800 °C with tension.

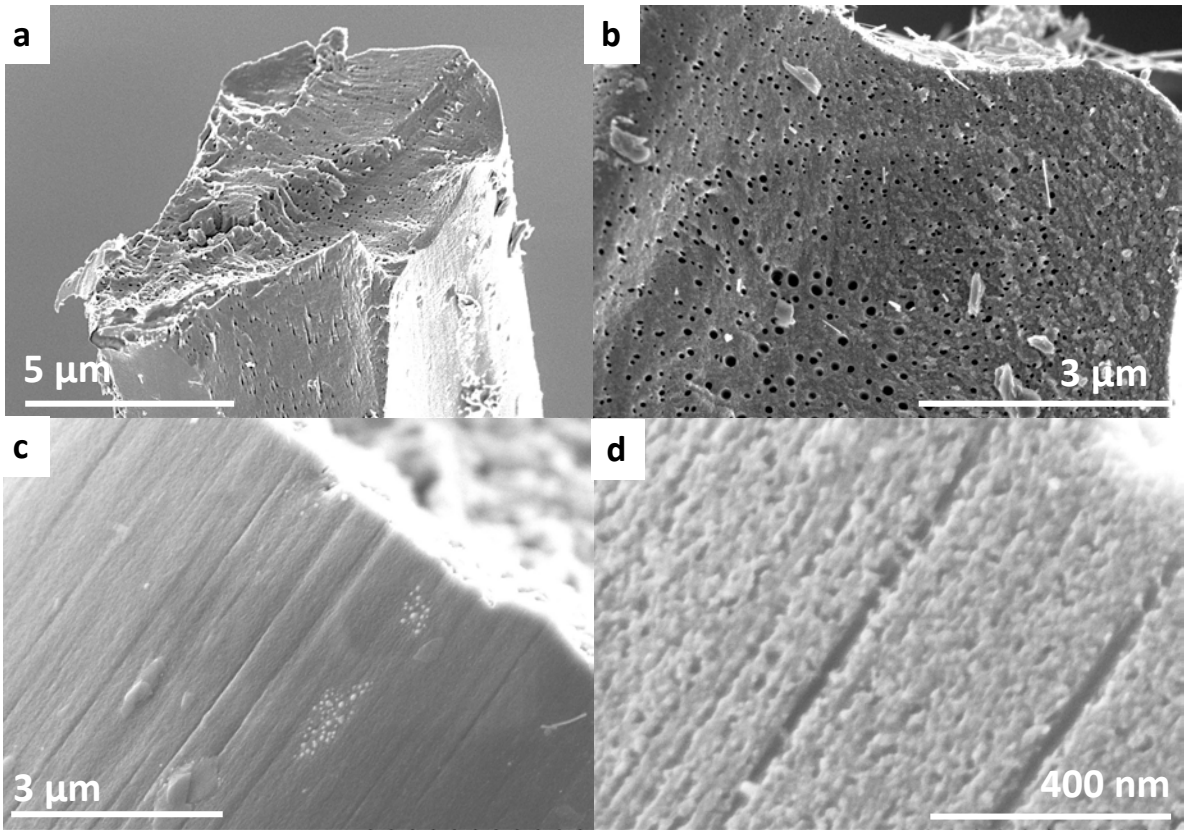

Figure 3.2. Representative SEM images of carbon fiber cross-section (a-b) and surface (c-d), carbonized at 1315 °C with tension.

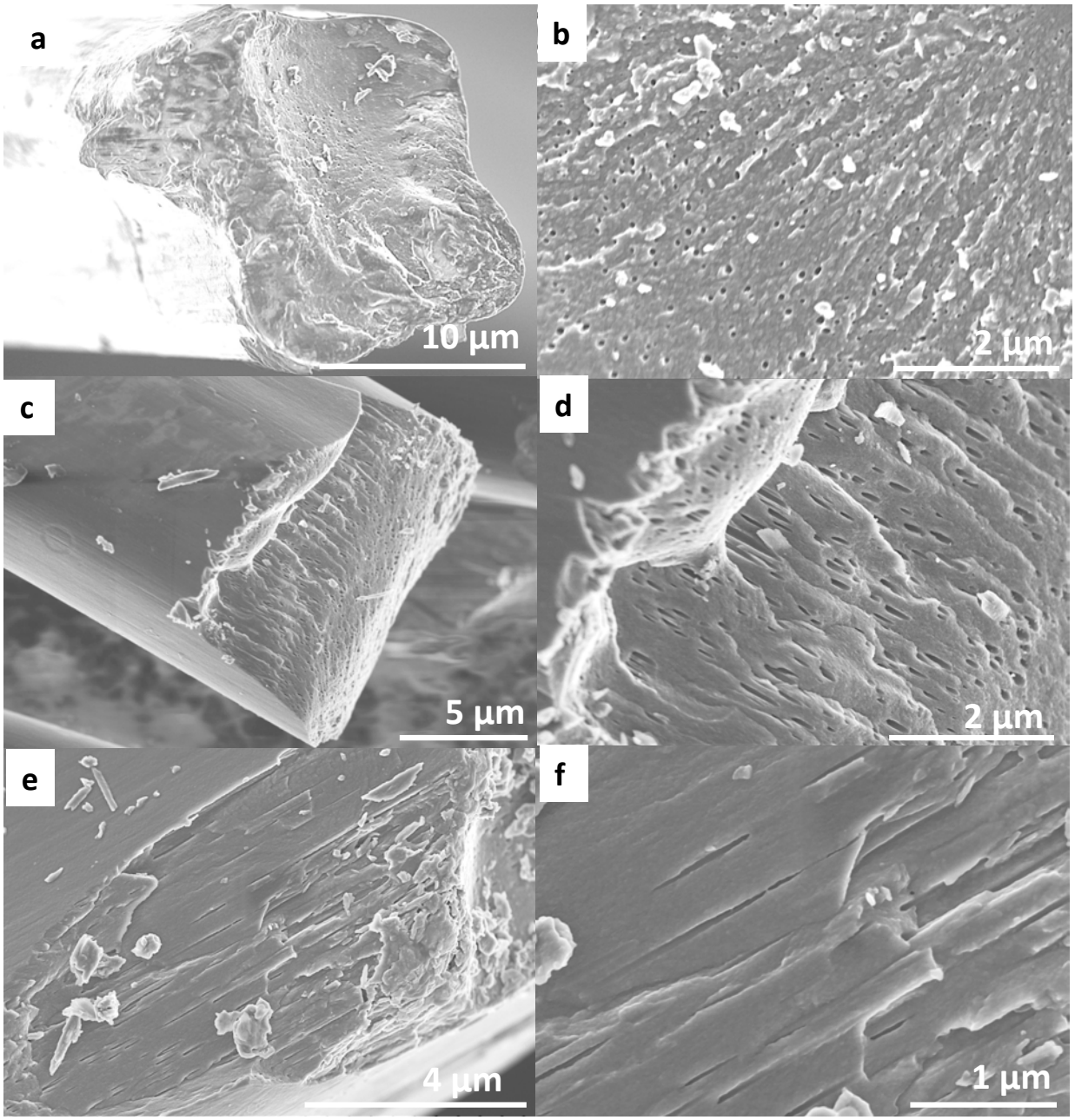

Figure 3.3. Representative SEM images of carbon fiber cross-section (a-d) and surface (e-f), carbonized at 800 °C without tension.

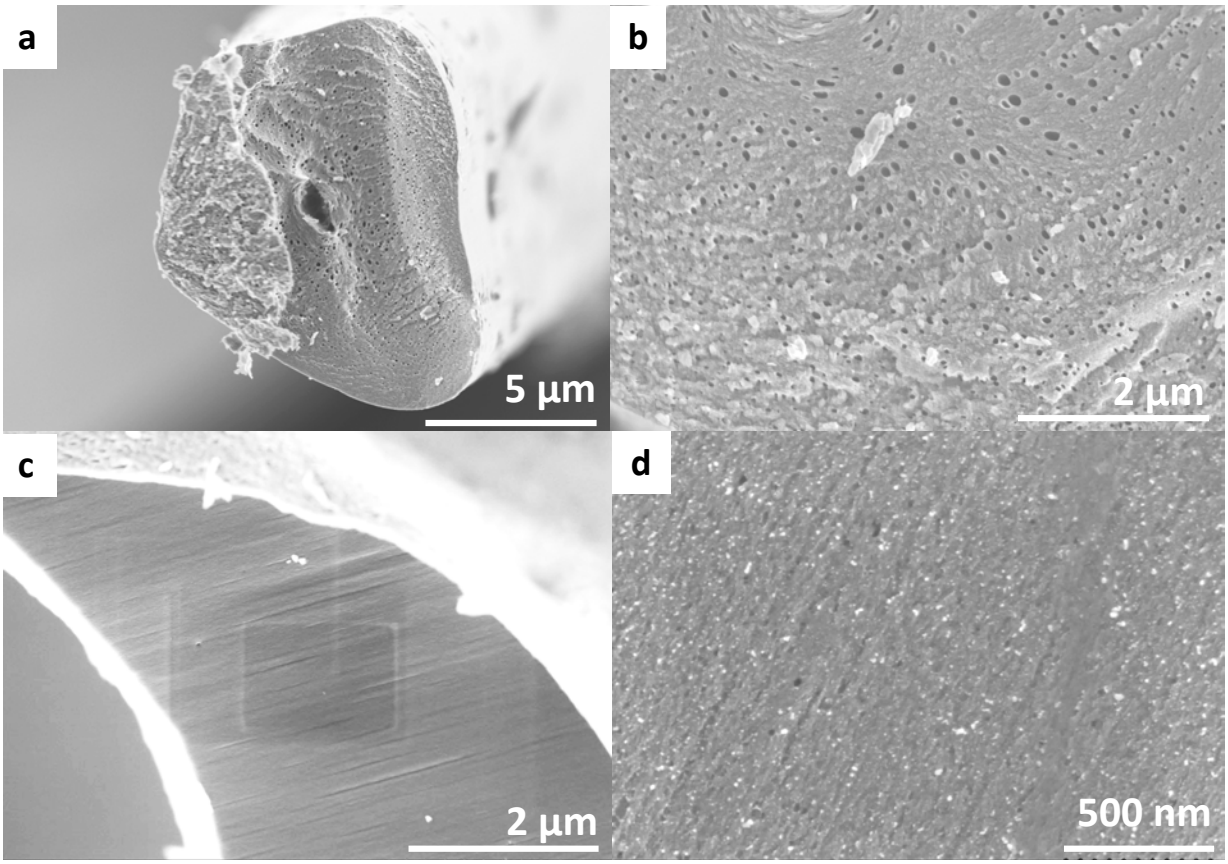

Figure 3.4. Representative SEM images of carbon fiber cross-section (a-b) and surface (c-d), carbonized at 1315 °C without tension.

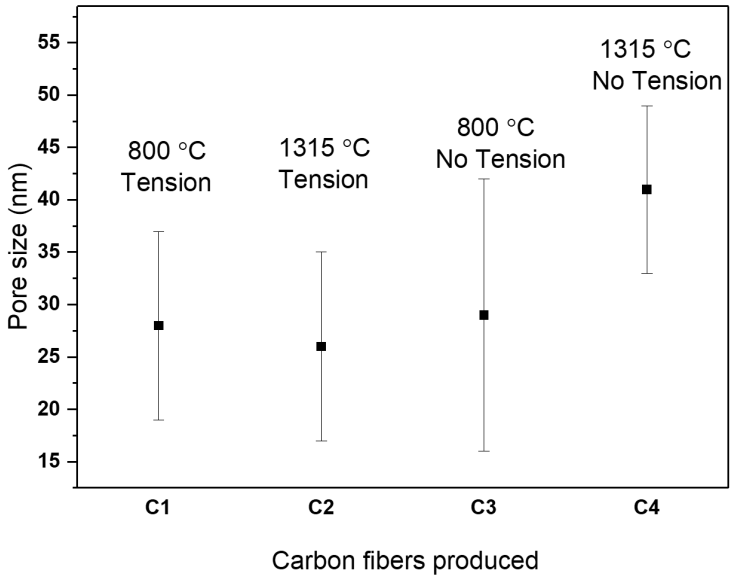

Figure 3.5. Comparison of pore sizes of different carbon fibers from PAN-SAN blend precursor fibers.

3.3.3. Mechanical and structural performance of porous carbon fibers

While the porous channel morphology of the PAN-SAN system was still observed in the four different carbon fibers, we studied if the change in the blend ratio indeed improved the tensile performance of carbon fibers derived from them (Table 3.2). Unlike in the case of carbon fibers from PAN-SAN (90/10) and PAN-SAN (80/20), the tensile properties of fibers from PAN-SAN (95/5) pyrolyzed with tension were measured successfully. The tensile properties of PAN-SAN (95/5) carbon fibers pyrolyzed without tension could not be measured. Thus, application of tension during stabilization and carbonization was critical to improving the tensile properties of the porous fibers. Increasing the carbonization temperature of the PAN-SAN fibers improved the tensile properties, with the fibers carbonized at 1315 °C exhibiting a tensile strength and

modulus of 0.9 GPa and 165 GPa, respectively. The tensile properties of the PAN-SAN derived fibers were compared with PAN-PMMA (90/10) based porous and PAN-based non-porous fibers, produced under similar conditions and, carbonized at ~1300 °C. PAN-SAN (95/5) derived carbon fibers had lower tensile strength and modulus when compared to both the PAN-PMMA (90/10) and PAN derived carbon fibers. Differences between the porous morphology could explain the above observation. Pores with average size of ~26 nm were observed both on the interior and exterior of the PAN-SAN fibers (Figure 3.2) unlike the case of PAN-PMMA fibers which showed elongated pores of 31 nm only on the interior of the fibers (Figure 2.7) with no visible pores on the exterior (Figure 2.11b). This difference in the pore distribution between the two systems of PAN-SAN (homopolymer-copolymer) and PAN-PMMA (homopolymer-homopolymer) arises due to the variation in the interaction of the sacrificial polymer with PAN. In the case of PAN-SAN blends, the common unit of acrylonitrile (AN) in the copolymer SAN has attractive interaction with surrounding PAN matrix and a repulsive interaction with styrene units that is counterbalanced by a covalent bond. As elucidated in section 1.4.2, such interactions between the copolymer and PAN-SAN system could render it a self-assembled morphology with well-distributed pores (uniform average pore size) unlike in the case of PAN-PMMA. This is also consistent with the study by Zhou et al where carbon fibers electrospun from di-block copolymer, PAN-b-PMMA, had well distributed pores of uniform size in comparison to the non-uniform pores from PAN-PMMA (homopolymer-homopolymer) blends.[129] PAN-PMMA (90/10) fibers with pore size of 31 nm in the interior and probable micropores (< 2nm) on the exterior possibly resulted in their comparable properties to non-porous PAN based fibers. Well-distributed pores with

uniform pore size across the interior and exterior decreased the tensile properties of PAN-SAN (95/5) derived fibers when compared to PAN-PMMA (90/10) and PAN based fibers. Comparing fibers carbonized ~1300 °C, porous PAN-SAN based carbon fibers had ~50-60% of the specific tensile strength and modulus of the non-porous PAN-based carbon fibers. We believe that the above properties are a great improvement from the prior study in Chapter 2 and future study along this route can bridge the gap between the porous and non-porous fibers to yield strong but lightweight fibers. In Chapter 2, we proposed a potential pathway to design structurally strong porous fibers utilizing the phase-separated morphology rendered by SAN and achieved that in this study by tuning the blend ratio. Decreasing the amount of SAN in the blend has proved to be one of the ways to impart structural integrity to carbon fibers with a porous channel morphology.

Table 3.2. Mechanical properties of carbon fibers from various precursors, as listed.

	PAN-SAN (95/5) 800 °C Tension	PAN-SAN (95/5) 1315 °C Tension	PAN-PMMA (90/10) [118]	PAN [117]
Diameter (μm)	10.8	9.8	9.4	8.2
Tensile Strength (GPa)	0.4 ± 0.2	0.9 ± 0.3	1.5 ± 0.3	2.1 ± 0.3
Tensile Modulus (GPa)	54 ± 8	165 ± 39	281 ± 22	288 ± 9
Specific Strength (N/tex)	0.3± 0.1	0.6 ± 0.2	1.2 ± 0.2	1.2 ± 0.2
Specific Modulus (N/tex)	34 ± 5	103 ± 25	192 ± 15	162 ± 5
Elongation at Break (%)	0.7 ± 0.3	0.6 ± 0.1	0.5 ± 0.06	0.8 ± 0.1

We further studied the structural parameters of the four groups of porous carbon fibers (Table 3.3 and Figure C.3). All the four groups of fibers showed the typical characteristic peaks of carbon fibers at ~26° (002) and ~43° (10). At a given temperature of carbonization, the fibers carbonized with tension had marginally higher orientation factor and L10 crystal size, aiding the improvement in their tensile properties. With the increase in temperature of carbonization temperature, the crystal size (L10) and orientation factor were higher for both the fibers carbonized with and without tension. The better mechanical performance of the fibers carbonized at 1315 ºC with tension compared to the 800 ºC (Table 3.2), aligned with their improved structural parameters. PAN-SAN and PAN fibers produced under similar conditions and carbonized at ~1300 ºC with tension had comparable structural parameters. Raman I_D/I_G ratio characterizing the graphitic ordering of carbon was obtained through Raman scattering by the defects (D-band at ~1330 cm^{-1}) and the graphitized plane (G-band at ~1560 cm^{-1}). Irrespective of the application of tension or not, PAN-SAN derived porous fibers at a particular temperature of carbonization showed comparable ratio. In parallel with the structural and tensile properties, fibers carbonized at higher temperature had higher graphitic ordering. Porous PAN-SAN fibers had higher graphitic ordering than the non-porous PAN based fibers produced under similar conditions, which is consistent with the I_D/I_G ratio of the porous fibers from blend precursors in Chapter 2. In another study, hollow PAN-PMMA based carbon fibers (I_D/I_G ratio: 1.88-2.0) had higher graphitic ordering than the commercially produced solid IM7 carbon fibers (I_D/I_G ratio 2.3).[130] Thus, fibers with pores seem to have a higher graphitic order when compared to solid fibers.

Table 3.3. Structural properties of carbon fibers from various precursors, as listed.

	PAN-SAN (95/5) 800 ºC Tension	PAN-SAN (95/5) 1315 ºC Tension	PAN-SAN (95/5) 800 ºC No Tension	PAN-SAN (95/5) 1315 ºC No Tension	PAN [91]
L002 (nm)[a]	1.43	1.48	1.51	1.51	1.36
L10 (nm)[b]	1.10	1.96	1.34	1.74	1.98
f_{002}[c]	0.70	0.77	0.66	0.71	0.75
d-spacing (nm)[d]	0.347	0.353	0.346	0.356	0.356
I_D/I_G	2.79 ± 0.03	1.77 ± 0.08	2.42 ± 0.08	1.71 ± 0.06	2.5 ± 0.20

[a and b] Crystal size of (002) plane at 2θ ~ 26°, and (10) plane at 2θ ~ 43°, according to Scherrer's equation with K = 0.9.
[c] Orientation factor of (002) plane.
[d] d-spacing of (002) plane at 2θ ~ 26°.

3.4. Conclusion

Through this study, a way to improve the tensile properties of porous morphology presented by PAN-SAN systems in Chapter 2, was established. This was achieved by gel-spinning PAN-SAN precursor blend fibers with just 5 wt% of the sacrificial component, SAN. Tensile properties of PAN-SAN (95/5) precursor blend fibers were comparable to that of PAN-SAN (90/10) and higher than the PAN-SAN (80/20) fibers. The structural parameters of PAN-SAN (95/5) precursor blend fibers were characteristic of the major component PAN in the blend. Four different carbon fibers were produced from the PAN-SAN (95/5) precursors by systematically varying the pyrolysis conditions: carbonization temperature and application of tension. Porous channeled morphology was exhibited all the four different carbon fibers, like the PAN-SAN carbon fibers in Chapter 2. The

average pore sizes of these fibers were in the range of 26-41 nm. The tensile properties of porous carbon fibers from PAN-SAN (95/5) produced with tension were measured in this study, unlike the carbon fibers obtained from PAN-SAN (90/10) and PAN-SAN (80/20) precursor blend fibers. Tensile strength and modulus of carbon fibers (carbonized at 1315 °C, with tension) from PAN-SAN (95/5) were 0.9 GPa and 165 GPa, respectively. By changing the blend ratio alone, porous PAN-SAN based carbon fibers with specific strength and modulus that was about half of the non-porous PAN based carbon fibers were obtained and studying this system further can bridge the performance gap between porous and nonporous fibers.

CHAPTER 4. POROUS CARBON FIBERS FROM DI-BLOCK COPOLYMER

This study was a collaborative effort with major contributions by the following authors Jyotsna Ramachandran (dissertation author, Georgia Tech), Joel Serrano (equal contributing author, Virginia Tech) and Jinwon Cho (Georgia Tech) advised by Dr. Satish Kumar, Dr. Guoliang Liu and Dr. Seung Soon Jang, respectively. Synthesis of the block copolymer, pyrolysis of carbon fibers without tension and their imaging, physisorption, electrochemical characterization, were performed at Virginia Tech. Gel-spinning of the block copolymer, characterization of precursor polymer fibers, pyrolysis with tension, mechanical, structural and morphological characterization of porous carbon fibers were done at Georgia Tech. Computational study was done by Dr. Jang's research group at Georgia Tech. Other contributors to this work include Pedro J. Arias-Monje, Mingxuan Lu, Mohammad Hamza Kirmani (Georgia Tech); Tianyu Liu, John Elliott (Virginia Tech).

4.1. Introduction

Much of the research into multifunctional porous carbon fibers have been conducted by electrospinning.[129,131–133] Gel-spinning, as opposed to electrospinning, provides a favorable route to obtain high strength and high modulus carbon fibers from PAN.[11] Hollow carbon fibers with a density of ~1.15 g/cm^3, tensile strength of 2.3-3.0 GPa, and tensile modulus of 202-234 GPa were previously obtained from gel-spun bicomponent polymer fibers containing PAN in the sheath and sacrificial PMMA in the

core, producing lightweight yet strong structural reinforcements.[105,134,135] The improved tensile moduli of these hollow carbon fibers were attributed to an enhanced graphitic order despite a low density. However, the potential of gel-spun fibers to serve as energy storage material was unaddressed. Carbon fibers with spherical, elongated and channel-like pores were gel spun from blends of PAN and sacrificial polymers including, poly(acrylic acid) (PAA), PMMA and poly(styrene-*co*-acrylonitrile) (SAN), respectively (Chapter 2).[118] Porous carbon fibers from these gel-spun blends had 15-40% higher specific tensile modulus than the non-porous PAN based fibers. Nevertheless, the electrochemical performance of these fibers was not characterized.

Tuning porosity to enhance the electrochemical performance of carbon fibers has been achieved through electrospinning a carbon precursor of poly(acrylonitrile) (PAN) blended with sacrificial polymers such as poly(methyl methacrylate) (PMMA) and poly(styrene) (PS).[60,78] By using block copolymers (BCP) of PMMA-*b*-PAN instead of polymer blends, Zhou *et al.* reported porous carbon fibers with uniform mesopores showing an ultrahigh surface-area-normalized capacitance of 66 μF/cm^2.[129] The tunability of BCP molecular weight, composition, and processing conditions provides additional mechanisms for controlling physical and electrochemical properties of porous carbon fibers.[131–133] Despite the excellent electrochemical energy storage performance, the mechanical properties of these fibers remain elusive. There are likely tradeoffs in the design of structural energy storage materials.[34]

Herein, the preparation of porous carbon fibers from gel-spun BCP fibers and their use as structural energy storage materials were studied. To mitigate the effect of porosity on the structural properties,[35,136] bicomponent fibers of BCP with a reinforcing high-molecular

weight PAN were designed. BCP enhanced the electrochemical performance owing to the development of mesopores from the sacrificial block, meanwhile PAN balanced the loss in mechanical properties through graphitic ordering during pyrolysis. The polymer fibers were subjected to varying stabilization and carbonization processes, allowing for investigation of the effects of processing conditions on the mechanical and electrochemical performance of the porous carbon fibers. Through structural, mechanical, and electrochemical characterizations, the tradeoff between structural support and electrochemical energy storage performance of the porous carbon fibers was elucidated.

4.2. Experimental

4.2.1. Materials

Poly(acrylonitrile-*co*-methacrylic acid) (PAN; viscosity average molecular weight, M_v, 500,000 g/mol) was obtained from Japan Exlan, Co. Acrylonitrile (AN, ≥99%), methyl methacrylate (MMA, ≥99%), azobisisobutyronitrile (AIBN, ≥98%), benzene (≥99.9%), aluminum oxide (activated, neutral, Brockmann Activity I), *N*,*N*-dimethylformamide (DMF, ≥99.7%), and dimethyl sulfoxide (DMSO, ≥99.9%) were obtained from Sigma-Aldrich. The chain transfer agent cumyl dithiobenzoate (CBD) was synthesized similar to that in a previous report.[63] Methanol was used for polymer coagulation and washing. Nickel foam was purchased from MTI (surface density = 350 g m^{-2}) and used as electrode substrates. AN and MMA monomers were passed through neutral alumina columns to remove inhibitors prior to use. All other chemicals were used as received without further modifications.

4.2.2. Synthesis of PMMA-b-PAN

Poly(methyl methacrylate)-*block*-poly(acrylonitrile) (PMMA-*b*-PAN) was synthesized *via* reversible addition-fragmentation chain transfer (RAFT) polymerization. First, a mixture of MMA (65.0 mL, 309 mmol), CDB (169 mg, 0.309 mmol), and AIBN (50.8 mg, 0.155 mmol) were dissolved in benzene (103 mL) in a 1-L Schlenk flask. The mixture was subjected to three cycles of freeze-pump-thaw (FPT) followed by back-filling with N_2 to remove any residual oxygen. The flask was placed in an oil bath at 60 °C for 20 h to synthesize PMMA macro-chain transfer agents (CTAs) with a number average molecular weight (M_n) of 60,000 g/mol. The resulting PMMA macro-CTAs were precipitated in methanol, filtered twice, and dried under vacuum for 12 h. The purified PMMA macro-CTA was used to synthesize PMMA-*b*-PAN. PMMA macro-CTA (2.60 g, 10.8 μmol), AN (10.4 mL, 43.3 mmol), AIBN (1.78 mg, 2.70 μmol), and DMSO (28.9 mL) were mixed in a 1-L Schlenk flask. The mixture was degassed by three FPT cycles and then heated in an oil bath at 65 °C under N_2 atmosphere. After 24 h of reaction, the BCP contained a PAN block with a M_n of 100,000 g/mol (Table 4.1). The resulting PMMA-*b*-PAN block copolymers were purified following the same procedures as PMMA macro-CTAs.

4.2.3. Polymer characterizations

Using size exclusion chromatography (SEC), number-average molecular weight (M_n) and polydispersity index (PDI) were measured on an EcoSEC HLC-8320GPC equipped with a DynaPro Nanostar photometer and light scattering detector. The mobile phase was DMF containing 0.05 M LiBr. The eluent flow rate was 0.5 mL min^{-1} with a column temperature of 50 °C. Each SEC trace consumed 100 μL of 1 mg mL^{-1} polymer solution.

4.2.4. Gel spinning of polymer fibers

To prepare spinning solutions, PAN (11.5 g) was dissolved in prechilled DMF (0 °C, 100 mL) and then heated to 70 °C for 3 h using a silicone oil bath. Separately, PMMA-*b*-PAN (20 g) was added to DMF (100 mL) at room temperature, then heated at 50 °C for 1 h using a silicone oil bath and finally at 70 °C for 3 h. The polymer fibers were gel-spun using a spinning equipment manufactured by Hills, Inc., which has two barrel-shaped reservoirs for co-extruding bicomponent fibers from two solutions (schematic reported in ref.[117]). The core and sheath spinning solutions were extruded through a single hole spinneret (diameter, 200 μm). The area ratio of the core and sheath components was adjusted by varying the flow rates of the two solutions (Table 4.2). The extrudate was passed through an air gap of 6 cm and then through a methanol coagulation bath at -50 °C. The as-spun fibers were collected on the take-up-roller and stored in methanol overnight. The fibers were subsequently drawn at room temperature and then passed through a glycerol bath at 160 °C. Draw ratio (DR) of the fibers is defined as the ratio of the collection speed at the take-up rollers to the feed speed. Fibers were assigned draw ratios at the stages of spinning (SDR), room temperature (RDR) and hot drawing (HDR) due to the difference of the feed and collection speeds. The total draw ratio (TDR) was then calculated as the product of the draw ratios at the three stages: SDR*RDR*HDR. For comparison, single component PAN fibers with total draw ratio (TDR) of 22 were also produced following the same protocol and similar processing parameters. Table 4.3 lists the processing parameters of the two solutions used for spinning bicomponent and single component fibers during the study.

Table 4.1. Polymer characteristics of synthesized PMMA-b-PAN.

	PMMA-*b*-PAN (BCP)	
	PMMA	PAN
Molecular Weight* (g/mol)	60,000	100,000
Weight Ratio	0.38	0.62
Total Molecular Weight* (g/mol)	160,000	
PDI	1.19	

*Based on number-average molecular weight as determined by SEC using a light-scattering detector.

Table 4.2. Configurations of gel-spun polymer fibers.

Designation	Core (A1)	Sheath (A2)	Area Ratio (A1:A2)	Overall PMMA content (wt.%)*
'BCP sheath'	PAN	PMMA-*b*-PAN	70:30	11
'BCP core'	PMMA-*b*-PAN	PAN	30:70	11
'BCP both'	PMMA-*b*-PAN	PMMA-*b*-PAN	-	38
'PAN both'	PAN	PAN	-	0

*For 'BCP both' fibers, the amount of PMMA in the PMMA-b-PAN is 38 wt.%, as obtained from Table 4.1. For the 'BCP sheath' and 'BCP core' fibers, the area of PMMA-b-PAN is 30 %. Using the relationship of Area % ≈ Volume % ≈ Weight % ($\rho_{PAN} \approx \rho_{PMMA}$= 1.18 g/cm^3), the amount of PMMA in the 'BCP sheath' or 'BCP core' fibers is calculated to be 11 %.

Table 4.3. Parameters of the PMMA-b-PAN and PAN solutions used for spinning polymer fibers in all three different configurations.

	PMMA-*b*-PAN	PAN
Solid Content (g/dL)*	20	11.5
Solvent	DMF	
Spinning Barrel Temperature (°C)	70	
Spinneret Temperature (°C)	80	
Coagulation Bath	Methanol (-50 °C)	

*Solid content of the spinning solution is the weight of polymer dissolved in a given volume of solvent (DMF).

4.2.5. Stabilization and carbonization of polymer fibers

Without tension throughout the process, the polymer fibers were first stabilized in air at 280 °C for 8 h (heating rate, 1 °C/min) in an electrical tube furnace (Model STF55433C-1, Lindberg/Blue M). Subsequently, the fibers were pyrolyzed at 800 °C for 1 h (heating rate, 10 °C /min) in a constant N_2 flow of 200 standard cubic centimeters per minute (sccm) under one atmosphere.

For comparison, another two groups of polymer fibers were stabilized and carbonized under tension in a tube furnace (Model H17HT2.5x24, Micropyretics Heaters International, Inc). The two groups of polymer fibers underwent two different thermal stabilization protocols (in air) before carbonization: one-step stabilization and two step-stabilization. In the first group, polymer fibers were heated from room temperature to 280 °C (heating rate, 3 °C/min) for 180 min, under a stress of 5-10 MPa, in air. The stabilized fibers were carbonized under N_2 atmosphere at 800 °C (heating rate, 10 °C/min) for 60 min under a constant stress of 5-10 MPa. The stress was based on the force over the overall cross-sectional area of the polymer fibers. In the second group, polymer fibers were stabilized at 265 °C for 170 min (heating rate, 3 °C/min) and 305 °C for 10 min (heating rate, 3 °C/min) in air and under constant stress of 10 MPa. The stabilized fibers were carbonized under N_2 by heating from room temperature to 1315 °C (heating rate, 5 °C/min) for 10 min, under a constant stress of 5-10 MPa.

4.2.6. Morphological characterizations

Morphologies of the fibers were characterized on two field-emission scanning electron microscopes (FE-SEM): one at Virginia Tech (LEO 1550) with an accelerating voltage of 2 kV and a working distance of ~3 mm and the other at Georgia Tech

(HITACHI SU8230) with an accelerating voltage of 1-5 kV and a working distance of ~5-7 mm. *ImageJ* software was used to analyze the SEM images and measure the average pore size of the carbon fibers.

4.2.7. Physical characterizations

Thermal gravimetrical analysis (TGA) was performed on a Discovery TGA5500 (TA instruments) analyzer by heating samples from room temperature to 700 °C at a ramp rate of 10 °C/min under ultrapure N_2 (flow rate: 25 mL/min). N_2 and CO_2 physisorption was conducted by a pore analyser (3Flex Pore Analyzer, Micromeritics Instrument Corp.) at 77 K and 273 K, respectively. Prior to physisorption, all carbon fibers were heated at 90 °C for 60 min and then at 350 °C for 900 min in N_2 to desorb any moisture and hydrocarbons. The ramp rates of both heating processes were 10 °C/min. The surface areas were calculated using Brunauer-Emmett-Teller (BET) theory, and the pore size distributions were derived from non-local density functional theory (NLDFT).[129]

4.2.8. Mechanical and structural characterization

Rheology characterization of the spinning solution was performed on an ARES Rheometer with parallel plate geometry (25 mm plate diameter and 1 mm gap between the plates) at room temperature. A constant strain of 1% was applied and the angular frequency varied from 0.1 to 300 rad/s. Tensile testing of all the polymer fibers, except 'BCP sheath', was done using a single filament testing equipment (FAVIMAT$^+$), at a strain rate of 1% /s and gauge length of 25.4 mm. At least 25 samples were tested for each type of fiber. 'BCP sheath' fibers, due to the crimp, were tested using RSA III solids

analyzer (Rheometric Scientific Co.), at a strain rate of 1% /s and gauge length of 25.4 mm by mounting single filaments on paper tabs. Temperature-sweep dynamic mechanical analysis (DMA) was conducted on fiber bundles with an effective cross-sectional area of 55 μm^2 at a frequency of 1 Hz and a heating rate of 1 °C/min from 30 to 180 °C using RSA III solids analyzer. Single filament tensile testing of carbon fibers was done using RSA III solids analyzer at a strain rate of 0.1% /s and gauge length of 12.7 mm by mounting single filaments on paper tabs. The tensile properties were calculated from stress-strain curves of the individual filaments based on the overall cross-sectional area. Wide-angle X-ray diffractions (WAXD) patterns were obtained on a Rigaku MicroMax 002 X-ray generator (Cu Kα radiation, λ = 1.5418 Å, 50 kV and 0.6 mA) equipped with a R-axis IV++ detector. The crystal size of PAN was calculated from the full width at half-maximum intensity (FWHM) of its crystalline peak from the equatorial scan using Scherrer's equation with k (a dimensionless shape factor constant) of 0.9.

4.2.9. Electrochemical characterizations

Electrochemical tests were performed on a PARSTAT 4000+ electrochemical workstation (Princeton Applied Research, AMETEK Inc.) with a three-electrode configuration. The working electrodes were made by ~1 mg of carbon fibers sandwiched between two pieces of nickel foam and pressed at 4 metric tons for 30 seconds with a benchtop hydraulic press (Stongway, Model 46269). An Ag/AgCl electrode (in saturated KCl aqueous solution) and a piece of nickel foam served as the reference and counter electrodes, respectively. The electrolyte was 3 M aqueous KOH solution. Cyclic voltammetry (CV) was carried out within a potential window from 0 to -0.8 V *vs.* Ag/AgCl. CV curves were collected at various scan rates between 10 and 1000 mV s^{-1}

and chronopotentiometry (CP) tests were performed at 10 A/g. The CV-based gravimetric capacitances were calculated using the following equation[29]:

$$C = \frac{1}{2(V_t - V_0)v} \int_{V_0}^{V_t} |I_m(V)| dV \quad (4.1)$$

where I_m (V) is the current density (A/g); v is the scan rate (mV/s); V_0 and V_t are the lower and upper potential limits of the potential window, respectively. Alternatively, CP capacitance was calculated using the discharging time (Δt) [137]:

$$C = \frac{I_m \Delta t}{\Delta V} \quad (4.2)$$

where I_m is the current density (A/g) and ΔV is the potential window. Electrochemical impedance spectroscopy (EIS) was conducted between 0.1 and 100 kHz with 10 mV perturbation at open-circuit potentials. The spectra were fit according to an equivalent circuit using *ZSimpWin* software.

4.2.10. Calculation of interaction parameter and characteristic correlation length

Computational methods were used to calculate the interaction parameter and the characteristic correlation length of PMMA-*b*-PAN. The interaction parameter χ, defined by Flory-Huggins solution theory, is key for determining the miscibility between two or more polymers. In previous studies, a computational method to estimate the χ-parameter was developed, and the results were well-agreed with several experimental systems.[138,139] The χ-parameter defined on the basis of mixing energy is expressed as follows:

$$\chi_{i,j} = \frac{\Delta E_{ij}}{RT} \quad (4.3)$$

where $\chi_{i,j}$ is the χ-parameter between polymer i and j, which in this case are PMMA and PAN, respectively, and ΔE_{ij} is the mixing energy of polymer i and j (Appendix D.2.1).

Initially, the interaction parameters of low molecular weight PMMA-*b*-PAN (monomer, dimer, and trimer) with various molecular conformations were computed through multiscale models before extending the calculation to synthesized BCP with molecular weight of ~160,000 g/mol. In this study, three different molecular conformations, namely syndiotactic (Syn), isotactic (Iso), and atactic (Ata) PMMA and PAN, were considered for the ΔE_{ij}calculations. Owing to the experimental conditions, both PMMA and PAN are likely to be randomly orientated in this study, and thus we calculated $\chi_{i,j}$ for PMMA Iso & PAN Syn and PMMA Syn & PAN Iso blocks to mimic the atactic nature of both the polymers.

Based on the $\chi_{i,j}$ calculations results, further dissipative particle dynamic (DPD; Appendix D.2.2) simulation was carried out to investigate the morphology of the synthesized PMMA-*b*-PAN by employing the following equation from our previous work and then calculated the characteristic correlation length *via* radial distribution function (RDF) analysis.[138,139] The characteristic correlation length defines the scale of a phase separation which can be directly compared to X-ray diffraction data.

4.3. Results and Discussion

The precursor to the carbon fibers, PMMA-*b*-PAN, was synthesized by RAFT polymerization with a M_n of 60,000-*b*-100,000 g/mol, as characterized by SEC (Figure D.1). The molecular weight was sufficiently high for gel-spinning, but significantly lower

than that of typical PAN (M_v = 500,000 g/mol) for synthesizing carbon fiber with high tensile strength and modulus.[11] To achieve good mechanical properties, PAN was used along with BCP to prepare polymer fibers of four different configurations: 1) BCP in sheath and PAN in core ('BCP sheath'); 2) BCP in core and PAN in sheath ('BCP core'); 3) BCP in core and sheath ('BCP both'); and 4) PAN in core and sheath ('PAN both' as a control) (Table 4.2). The amount of PMMA in the 'BCP both' and bicomponent fibers ('BCP sheath' and 'BCP core') were 38 and 11 wt.%, respectively.

4.3.1. Morphologies of carbon fibers

By varying the processing temperature and tension during pyrolysis, the polymer fibers were processed into porous carbon fibers with tunable mechanical and electrochemical properties. After pyrolysis at 800 °C without tension, the four types of carbon fibers showed different morphologies (Figures 4.1-4.2). The average pore size of the fibers was calculated based on SEM images using an image processing software, ImageJ. When BCP was extruded in the sheath, the exterior showed axially aligned mesopores with an average pore size of 27 ± 8 nm. When BCP was extruded in the core, the PAN sheath formed a solid carbon matrix and the BCP core yielded aligned mesopores with an average size of 30 ± 9 nm. For 'BCP both' carbon fibers, both cross section and the fiber surface exhibited well distributed and aligned pores of 21 ± 7 nm in size. The differences in the mesopore sizes in these three types of porous carbon fibers was not significant considering the relatively large error bars. Regardless, the BCP-derived mesopores in all cases were elongated (non-spherical) and axially aligned, owing to the multi-stage drawing and shearing in the fiber preparation process. As a control, the 'PAN-both' fibers showed no mesopores.

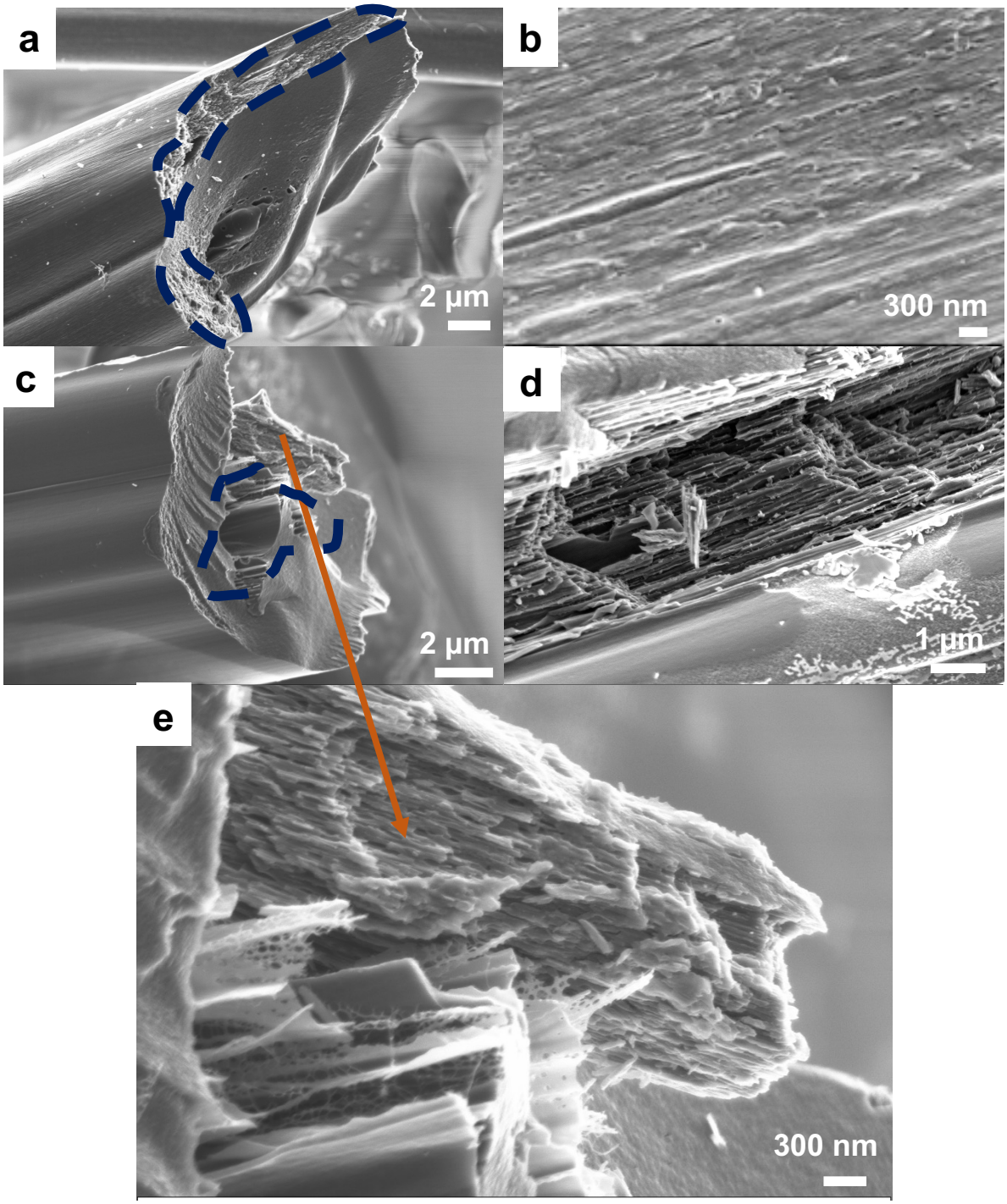

Figure 4.1. Representative cross-sectional (a, c, d, and e) and fiber-surface (b) SEM images of carbon fibers from varying polymer fibers: (a-b) 'BCP sheath', (c-e) 'BCP core'. All carbon fibers were pyrolyzed without tension at 800 °C.

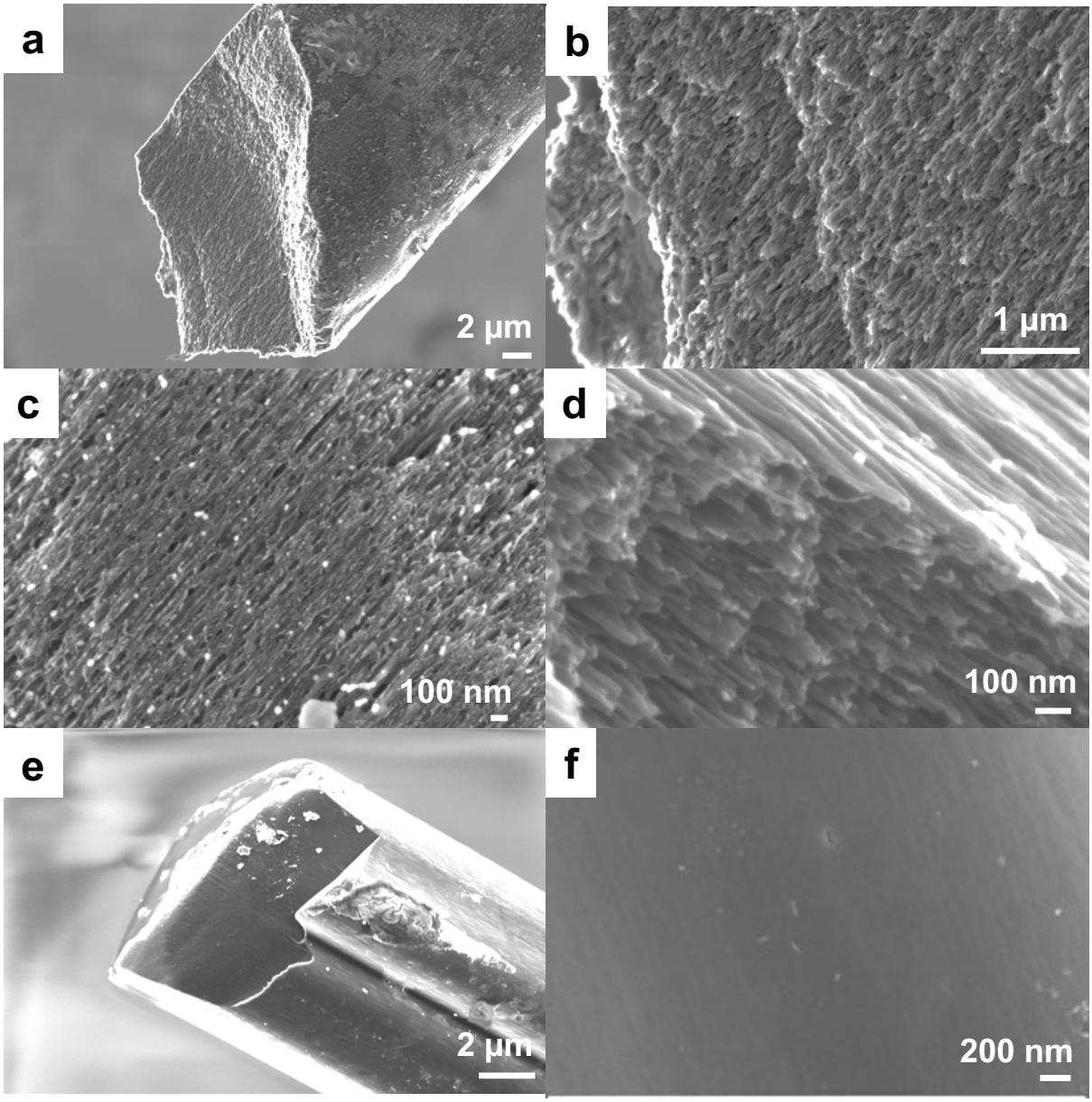

Figure 4.2. Representative cross-sectional (a, b, d, and e) and fiber-surface (c and f) SEM images of carbon fibers from varying polymer fibers: (a-d) 'BCP both', and (e-f) 'PAN both'. All carbon fibers were pyrolyzed without tension at 800 °C.

The porous structure and surface area were further characterized by CO_2 and N_2 sorption.[129,132] CO_2 physisorption probes micropores (< 2 nm) within the carbon fibers. For all three porous carbon fiber configurations, CO_2 sorption revealed type I isotherms and the hysteresis within the isotherms indicted the presence of micropores (Figure 4.3a). The micropore size distribution for all the three porous fibers exhibited multiple distinct peaks centered at ~0.53, 0.86, and 1.29 nm (Figure 4.3c). N_2 sorption showed type IV isotherm,[140] for 'BCP both', 'BCP sheath', and 'BCP core' carbon fibers, with hysteresis at $0.7<P/P_0<0.9$ indicating the presence of mesopores (Figure 4.3b). Based on NLDFT, the mesopore volume decreased in the sequence of 'BCP both', 'BCP sheath', and 'BCP core' (Figure 4.3c), with 'BCP both' showing a distinct peak at 23 nm. The same trend was reflected in the surface area of these fibers. 'BCP both' carbon fibers exhibited the highest surface area (264 m^2/g) followed by 'BCP sheath' (27 m^2/g) and 'BCP core' (2 m^2/g) carbon fibers. 'BCP both' based carbon fibers possessed the highest amount of PMMA (38 wt.%) and in addition, the mesopores were present in both the sheath and core portions which contributed to these fibers having the highest mesopore volume and surface area. 'BCP sheath' carbon fibers had a larger mesopore volume and surface area than the 'BCP core' carbon fibers, despite the same amount of PMMA (11 wt.%). This phenomenon might arise owing to the larger amount of PMMA derived pores along the surface of 'BCP sheath', thereby enhancing accessibility during physisorption. With BCP-derived mesopores in the sheath, the gas molecules could assess pores both near the surface and in the interior. However, with BCP-derived mesopores in the core, the PAN-derived non-porous carbon layer shielded the access to pores in the core, thereby reducing the effective mesopore volume and surface area of 'BCP core' fibers.

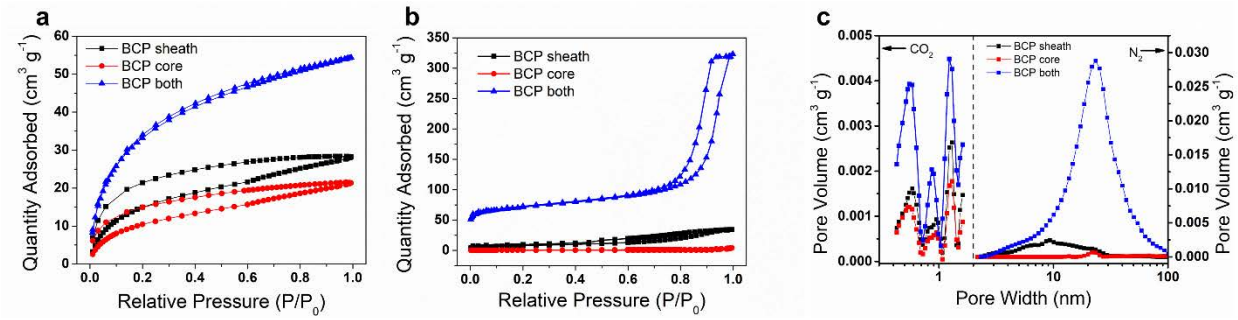

Figure 4.3. Gas physisorption of carbon fibers after pyrolysis at 800 °C without tension: (a) CO2-physisorption isotherms, (b) N2-physisorption isotherms, and (c) pore width distributions based on NLDFT.

The morphologies of carbon fibers after pyrolysis under tension were also investigated (Figures 4.4- 4.5, D.3-D.5). While axial alignment of mesopores was a consistent feature among all BCP-derived carbon fibers with or without tension, the mesopore size differed. As the pyrolysis temperature was increased from 800 to 1315 °C, the average mesopore size of 'BCP sheath' fibers marginally increased from 13 to 19 nm. 'BCP core' fibers displayed solid carbonized exteriors arising from the PAN sheath from both pyrolysis temperatures, 800 and 1315 °C.

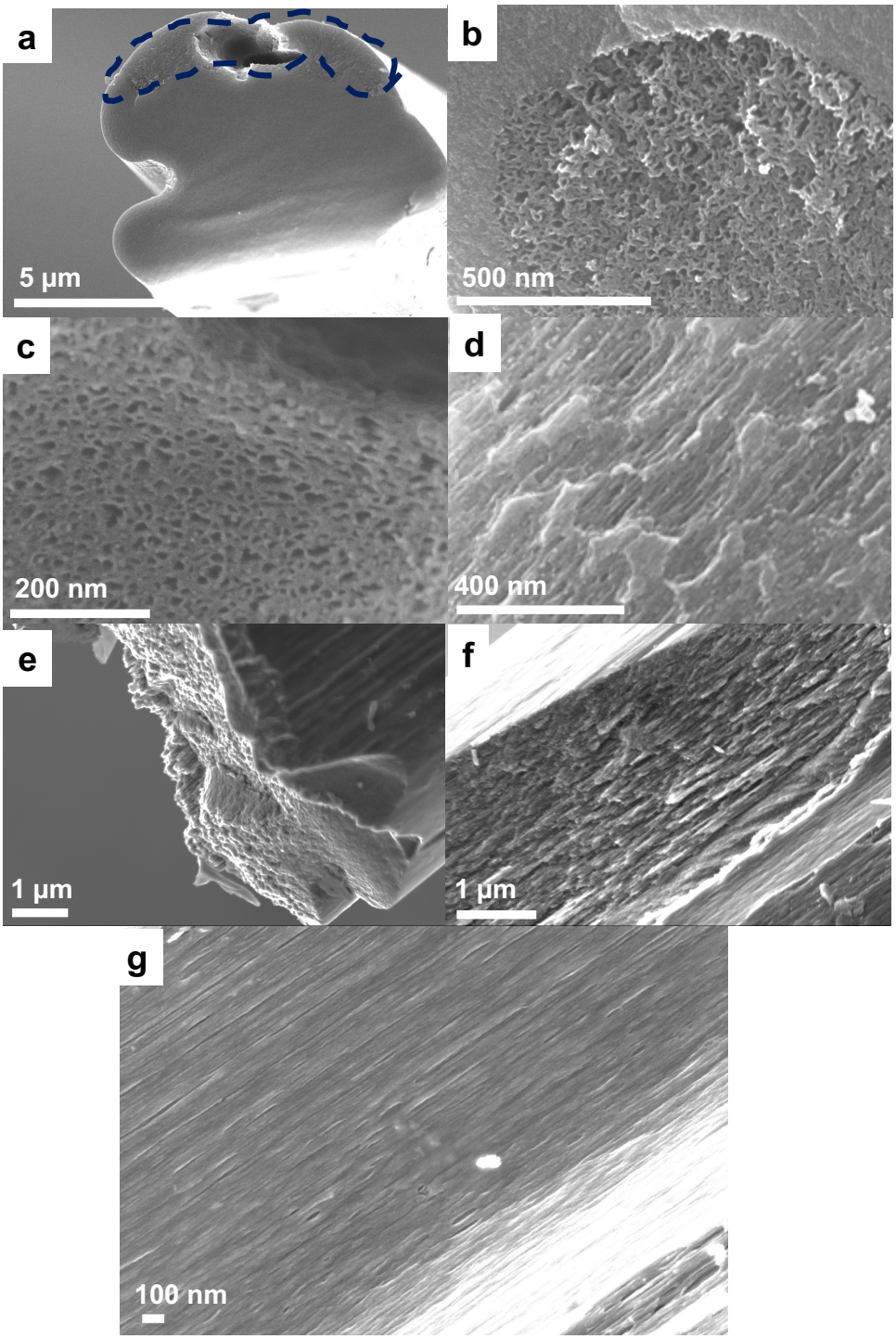

Figure 4.4. Representative SEM images of carbon fibers after pyrolysis of 'BCP sheath' polymer fibers at (a-d) 800 °C and (e-g) 1315 °C under tension. Panels a, b, c, e, and f are cross-sections. Panels d and g are the fiber surfaces.

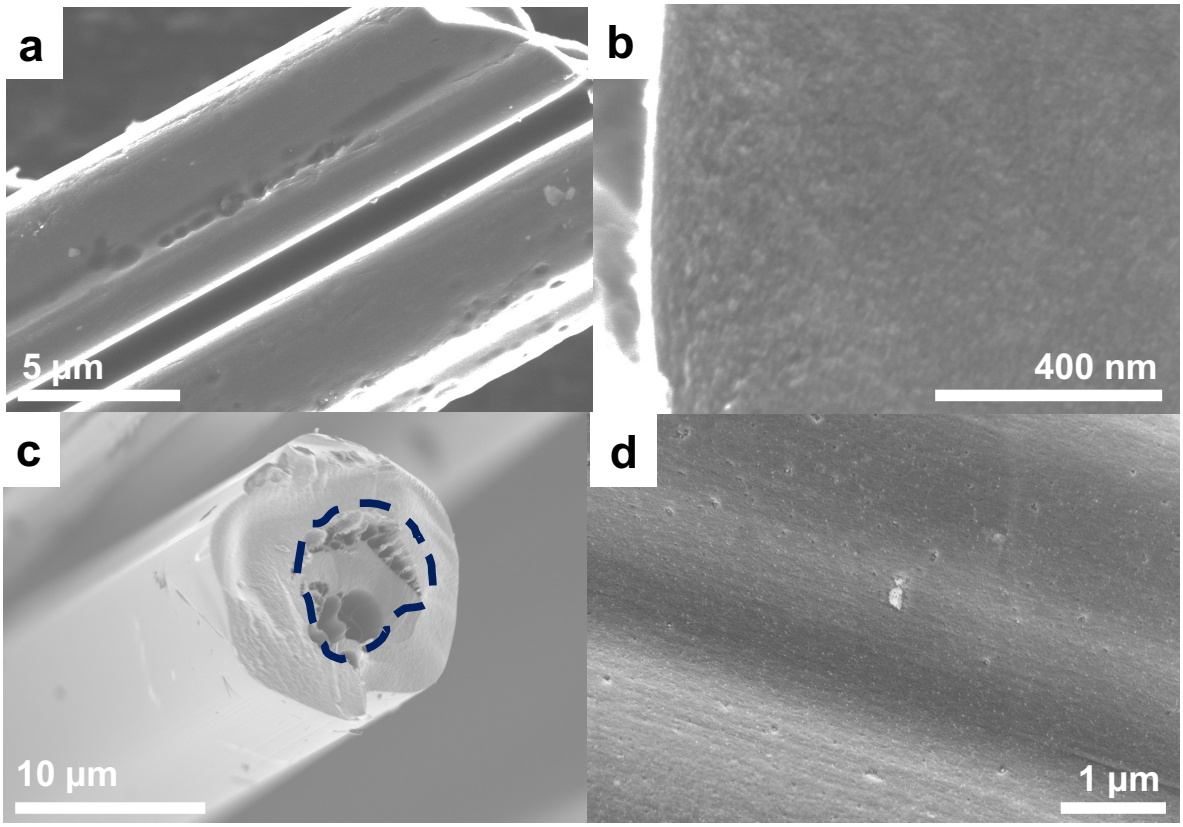

Figure 4.5. Representative SEM images of carbon fibers after pyrolysis of 'BCP core' polymer fibers at (a-d) 800 °C and (c-d) 1315 °C under tension. Panels a and d are the fiber surfaces. Panels b and c are cross-sections.

Based on the cross-sectional SEM images, the morphologies of the bicomponent fibers were analyzed. Coaxial core-sheath (C/S) morphology was expected for the bicomponent fibers after gel spinning through a single spinneret (Figures 4.6a, 4.6c), but interestingly the actual fibers showed different morphologies (Figures 4.1a, 4.1c, 4.4a, 4.5c). In the 'BCP sheath' fibers, the PAN core was not fully encompassed by the 'BCP sheath' and the latter was pushed to one side of the fibers, rendering a side-by-side (S/S) instead of C/S morphology (Figure 4.1a, 4.4a, 4.6b). In 'BCP core' fibers, the core shifted away from the center but still fully encompassed by the sheath (Figure 4.1c, 5c, 4.6d). These morphologies persisted in carbon fibers after pyrolysis, with or without tension.

To coaxially spin a stable C/S morphology with the sheath fully encapsulating the core, viscosity of the sheath solution must be lower than that of the core solution since the sheath experiences higher shear force.[141–144] In gel-spinning 'BCP core' polymer fibers, the viscosity of the BCP solution (20 g/dL) was higher than that of the PAN solution (11.5 g/dL) (Figure D.6a), thus rendering a C/S morphology. Upon switching the two components to prepare 'BCP sheath' polymer fibers, the lower viscosity of the PAN solution than that of BCP in the sheath solution drove the PAN from the core towards the edge to experience the higher shear force. Hence, BCP could not encapsulate PAN, leading to a S/S morphology.

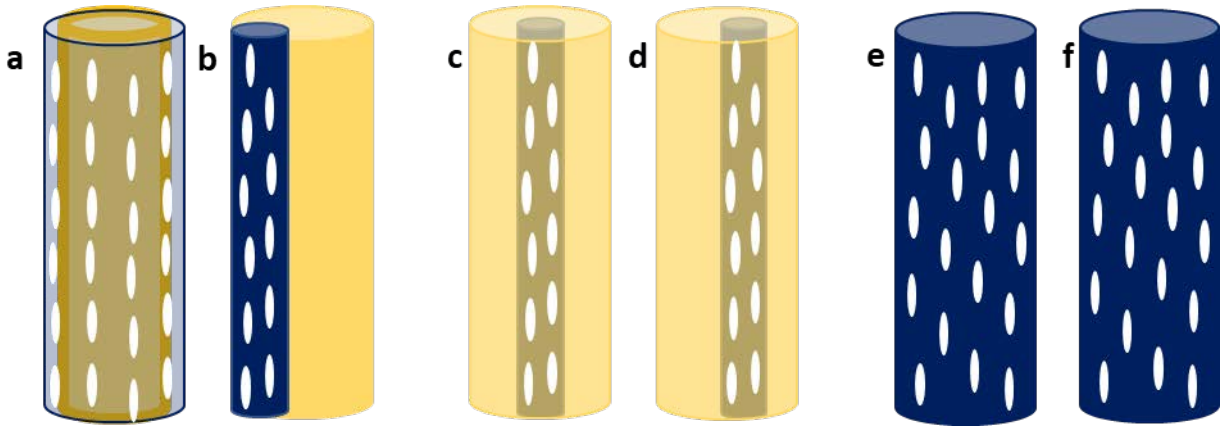

Figure 4.6. Schematics of the (a, c, e) expected and (b, d, f) experimentally obtained morphologies of 'BCP sheath' (a-b), 'BCP core' (c-d), and 'BCP both' (e-f), based on SEM images in Figures 4.1, 4.4 and 4.5.

4.3.2. Mechanical and structural characteristics of polymer fibers

Single component 'BCP both' and 'PAN both' polymer fibers showed different drawabilities of TDR=13.2 and 22, respectively. Due to the S/S morphology and different drawabilities, BCP and PAN in 'BCP sheath' polymer fibers were drawn to different degrees, and thus 'BCP sheath' carbon fibers exhibited a crimped behavior. Crimp is

prevalent in bicomponent fibers with the S/S morphology because the two components, if having differential characteristics like drawabilities and elasticity, are subjected to differential (imbalanced) force upon drawing.[145–148] Differently, in 'BCP core' polymer fibers that had a C/S morphology, the encapsulated BCP with lower drawability limited the drawability of the PAN sheath, resulting in the lowest TDR among the studied polymer fibers.

The mechanical properties of polymer fibers were influenced by the polymer constituents (BCP or PAN) and position of BCP (Table 4.4). Among the BCP-containing polymer fibers, 'BCP core' had the highest tensile strength and modulus, followed by 'BCP sheath' and 'BCP both'. Because BCP possessed a lower molecular weight (< PAN) and it contained PMMA,[105,134] all three BCP-containing polymer fibers exhibited inferior tensile properties to 'PAN both', which had a substantially higher molecular weight PAN as both the sheath and core components.

In a previous study, bicomponent PAN-carbon nanotubes (CNT) fibers with PAN (either in the sheath or core) as the reinforcement showed better tensile properties than single component PAN-CNT fibers.[149] In this study, the reinforcing effect of PAN was prevalent in the 'BCP core', which showed better tensile strength and modulus than 'BCP both' polymer fibers. Despite a higher draw ratio and reinforcing PAN core, the 'BCP sheath' polymer fibers showed mechanical properties inferior to 'BCP core' polymer fibers and similar to 'BCP both' polymer fibers. This was probably owing to the crimping effect arising from their S/S morphology, similar to previous reports.[146,150]

Table 4.4. Comparison of mechanical properties of polymer fibers.

	'BCP sheath'	'BCP core'	'BCP both'	'PAN both'
Total draw ratio (TDR)	19.8	10.8	13.2	22
Diameter (μm)	13.6	16 ± 3	21 ± 3	12 ± 0.2
Tensile Strength (MPa)	580 ± 50	760 ± 40	570 ± 20	902 ± 19
Tensile Modulus (GPa)	11 ± 1	16.8 ± 0.5	10.3 ± 0.3	18.5 ± 0.4
Elongation at Break (%)	5.2 ± 0.6	7.8 ± 0.4	9.7 ± 0.4	7.9 ± 0.9

Integrated WAXD graphs of the polymer fibers revealed peaks corresponding to the amount of PMMA in the fibers (Figure 4.7). Due to the low PMMA content (11%), the bicomponent polymer fibers of 'BCP sheath' and 'BCP core' showed two peaks at ~17° and 30°, both characteristic of PAN. In contrast, with a PMMA content of 38%, 'BCP both' polymer fibers exhibited another peak at ~12°, representative of PMMA.

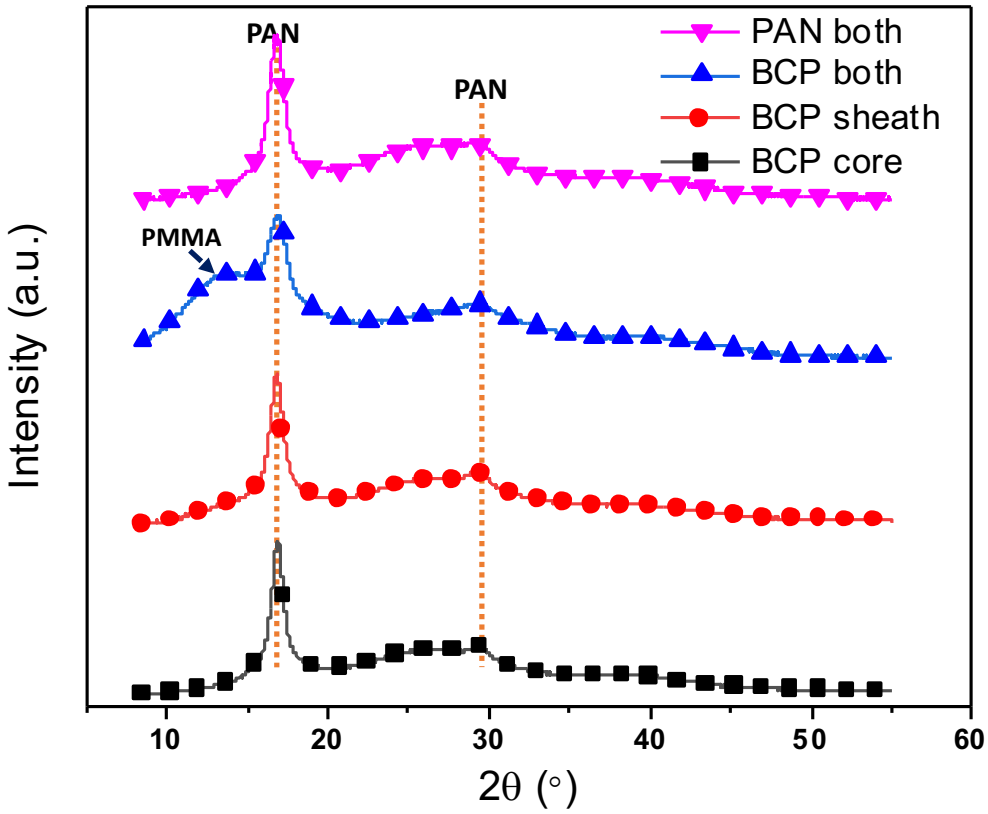

Figure 4.7. Integrated WAXD plots of 'BCP both', 'BCP sheath', 'BCP core', and 'PAN both' polymer fibers.

The crystalline structures in 'BCP both', 'BCP sheath', 'BCP core', and 'PAN both' polymer fibers were further analyzed (Table 4.5). 'BCP both' polymer fibers showed the lowest crystallinity and crystal size due to the highest content of amorphous PMMA (38 wt.%) and the absence of high molecular weight PAN. 'BCP core' polymer fibers exhibited the highest crystallinity and crystal size among the three BCP-containing systems, resulting in their highest tensile modulus of 16.8 GPa. Crimped 'BCP sheath' polymer fibers, despite a higher draw ratio than 'BCP core' polymer fibers exhibited lower crystallinity, smaller crystal size, poorer crystal orientation, and thus lower

mechanical properties. 'PAN both' fibers with the highest orientation exhibited the highest tensile strength and modulus than all the BCP-containing polymer fibers.

The amount of PMMA also influenced the packing of PAN crystals, as indicated by the d-spacing ratio determined from the peaks at ~ 17º and ~ 30º ($d_{17^\circ}/d_{30^\circ}$). 'BCP sheath', 'BCP core' and 'PAN both' polymer fibers had ratios of 1.731, 1.731 and 1.734, respectively, all closer to the value of 1.732 for hexagonally packed PAN crystals.[90] The low content of PMMA (11 wt.%) in these bicomponent polymer fibers was insufficient to substantially affect the PAN crystallization and packing, and thus they exhibited structural parameters characteristic of PAN (Figure 4.7 and Table 4.5).

Table 4.5. Structural properties of polymer fibers.

	'BCP sheath'	'BCP core'	'BCP both'	'PAN both'
Crystallinity (%)[a]	50	54	42	58
Crystal size (nm)[b]	8.9	10.5	6.7	8.4
f_{PAN}[c]	0.71	0.75	0.49	0.85
$d_{17^\circ}/d_{30^\circ}$[d]	1.731	1.731	1.727	1.734

[a] Crystallinity is calculated by excluding the amorphous peaks of PAN and BCP from the PAN crystalline peaks (Appendix D.1).
[b] Crystal size of PAN at 2θ ~17° (200) and (110) planes.
[c] Herman's orientation factor of PAN calculated from the azimuthal scan of PAN (200) and (110) planes (and adding the contribution after deconvolution of meridional peak at 2θ ~17°).
[d] Ratio of d-spacing of diffraction peaks at 2θ ~17° and ~30°.

The dynamic mechanical behaviors including storage modulus and tan δ were studied as a function of temperature (Figure 4.8). The storage moduli of 'BCP both', 'BCP sheath', and 'BCP core' polymer fibers decreased with temperature. 'BCP core'

polymer fibers showed the highest moduli in the range of 30 – 180 °C. At room temperature, the storage modulus decreased in the order of 'BCP core' > 'BCP sheath' ~ 'BCP both', similar to their tensile moduli (Table 4.4).

PAN exhibits tan δ peaks arising from thermo-mechanical transitions including: 1) α transition related to molecular motion in amorphous region (~140-160 °C) and 2) β_c transition corresponding to molecular motion in para-crystalline region of PAN (~75-110 °C).[91–93,151] The glass transition temperature for PMMA is around 110-115 °C.[152] In this work, the bicomponent fibers revealed tan δ peak at ~ 90 °C, which is attributed to the β_c relaxation of PAN. Contrastingly, the tan δ peak of 'BCP both' polymer fibers showed at ~135 °C, which is attributed to two characteristics: 1) the increased glass transition temperature of PMMA due to an interfacial augment effect of block copolymers and 2) the α transitions of amorphous PAN with lower crystallinity.[63] In short, 'BCP both' polymer fibers showed thermomechanical behaviors characteristic of both PMMA and PAN, whereas 'BCP core' and 'BCP sheath' polymer fibers presented dominantly PAN characteristics.

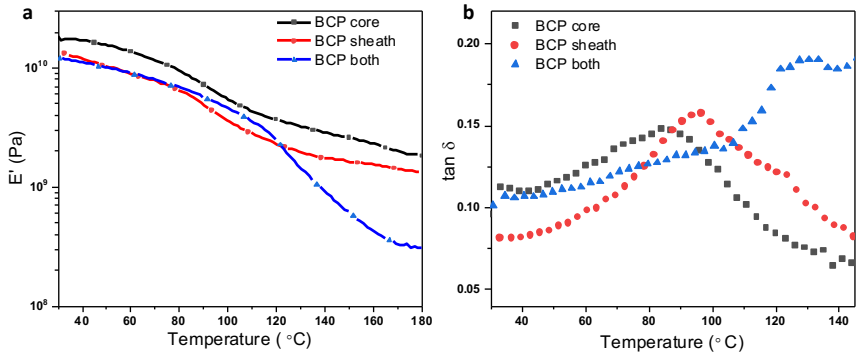

Figure 4.8. Dynamic mechanical analysis of 'BCP both', 'BCP sheath', and 'BCP core' polymer fibers at 1 Hz: a) storage modulus and b) tan δ.

4.3.3. Mechanical and structural properties of carbon fibers

Without tension, all polymer fibers were pyrolyzed successfully at 800 °C to produce carbon fibers. With tension, 'BCP both' polymer fibers broke after stabilization, and 'BCP sheath' and 'BCP core' polymer fibers were mechanically strong to survive the stabilization and carbonization at either 800 °C or 1315 °C to produce porous carbon fibers. The different mechanical strengths of these fibers are due to three reasons. First, unlike 'BCP core' and 'BCP sheath' polymer fibers, 'BCP both' polymer fibers lacked a high molecular weight PAN to reinforce the structure. Second, the dynamic storage modulus of 'BCP both' polymer fibers decreased rapidly with temperature (Figure 4.8a), indicating a significant reduction in the mechanical integrity during thermal treatment. Third, due to the high PMMA content of 38 wt.%, 'BCP both' polymer fibers would produce carbon fibers with a high degree of porosity, much higher than those of the 'BCP core' and 'BCP sheath' carbon fibers (Figure 4.3c). Thus, a combination of low polymer molecular weight, reduced mechanical strength upon thermal treatment, and high porosity caused 'BCP both' fibers to fracture during stabilization.

The influence of pyrolysis temperature and BCP position on the mechanical properties of the bicomponent fibers pyrolyzed under tension were assessed. As expected, the mechanical properties of carbon fibers pyrolyzed at 1315 °C were higher than those at 800 °C (Table 4.6).[3,14] Irrespective of BCP in the core or sheath, bicomponent 'BCP core' and 'BCP sheath' carbon fibers after pyrolysis at 1315 °C showed similar tensile strengths and tensile moduli (Table 4.6). Their tensile strengths and moduli, however, were lower than the non-porous carbon fibers from pure PAN (tensile strength of 2.08 GPa and tensile modulus of 288 GPa for PAN derived carbon fibers at 1315 °C).[117]

Similar to a previous report by Chen *et al*., the modulus decreased due to the loss of load bearing area, and the tensile strength decreased due to the non-uniform stress concentration around pores.[42] Owing to the 'crimping effect' and low pyrolysis temperature of 800 °C, 'BCP sheath' carbon fibers did not even withstand the sample preparation required for tensile testing.

In previous reports,[34,42] porous carbon fibers from electrospun PAN/PMMA blends had tensile modulus of ~70 GPa when pyrolyzed at 1100 °C. Notably, 'BCP core' carbon fibers from gel-spinning herein showed a similar tensile modulus of ~70 GPa at a lower pyrolysis temperature of 800 °C, and more than twice the modulus at 1315 °C.[34,42] Porous carbon fibers carbonized at 1315 °C, from gel-spun blends of PAN-PAA and PAN-PMMA (~10 wt%) had tensile strength of ~1.6 GPa and modulus of 280 GPa, closer to the non-porous PAN fibers.[118] Comparing the blends and BCP derived fiber, the significant difference lay in the molecular weights of PAN while the remaining factors including weight percent of sacrificial polymer and pyrolysis conditions were the same. BCP derived fibers used a combination of lower molecular weight PAN (100 kDa in the BCP) and higher molecular PAN (500 kDa) while the blends solely used the higher molecular weight PAN (500 kDa). Tuning the molecular weight of the BCP could be one of the potential paths forward to improve the tensile properties of these fibers. Thus, gel-spinning PAN/PMMA-*b*-PAN fibers in a core-sheath manner provides a promising means for designing good mechanical property porous carbon fibers.

Table 4.6. Mechanical properties of carbon fibers from bicomponent polymer fibers carbonized under tension. *

	800 °C	1315 °C	
	'BCP core'	'BCP sheath'	'BCP core'
Tensile Strength (GPa)	0.3 ± 0.1	1.1 ± 0.3	1.2 ± 0.6
Tensile Modulus (GPa)	70 ± 60	190 ± 20	179 ± 17
Elongation at Break (%)	0.4 ± 0.1	0.6 ± 0.1	0.7 ± 0.3

*'BCP sheath' carbon fibers after pyrolysis at 800 °C under tension were too brittle and could not be tested for mechanical properties.

Variables including the pyrolysis temperature, position of BCP, and the tension during pyrolysis influenced the structural parameters of carbon fibers. Integrated WAXD plots of all porous carbon fibers (Figure D.8) showed typical PAN-derived carbon peaks at ~ 26° corresponding to (002) and 43° corresponding to (10) planes. The structural parameters are summarized in Table 4.7. First, at the carbonization temperature of 1315 °C under tension, 'BCP sheath' and 'BCP core' carbon fibers did not differ significantly in their structural parameters, consistent with their mechanical properties. For bicomponent polymer fibers, the position of BCP affected the orientation of the turbostratic planes after pyrolysis at 800 °C without tension. 'BCP sheath' carbon fibers had no preferential orientation while the 'BCP core' fibers had a modest orientation factor of 0.37. Excluding the orientation factor, their other structural parameters were similar. Second, the application of tension during pyrolysis at 800 °C improved the orientation factor of the turbostratic planes from zero to 0.74 and from 0.37 to 0.72 for 'BCP sheath' and "BCP core' carbon fibers, respectively. Lastly, the crystal sizes and orientation factor increased with the carbonization temperature due to a higher degree of

turbostratic ordering. Comparing the fibers carbonized under tension, the higher relative intensity of the 43° peak and the lower FWHM of the fibers pyrolyzed at 1315 °C than those at 800 °C corroborated the higher crystallite size (L_{10}) and mechanical performance.

Table 4.7. Comparison of structural properties of carbon fibers from bicomponent polymer fibers.

Condition	Configuration	L_{002} (nm)[a]	L_{10} (nm)[b]	f_{002}[c]
800 °C, Tension	'BCP sheath'	1.33	1.21	0.74
	'BCP core'	1.65	1.30	0.72
1315 °C, Tension	'BCP sheath'	1.51	2.11	0.78
	'BCP core'	1.76	2.70	0.79
800 °C, No tension	'BCP sheath'	1.23	1.30	0
	'BCP core'	1.28	1.33	0.37

Crystal size of [a](002) plane at $2\theta \sim 26°$ and [b] (10) plane at $2\theta \sim 43°$, according to Scherrer's equation with K = 0.9.
[c] Orientation factor of (002) plane.

4.3.4. Electrochemical energy storage performance

Owing to the mechanical strength and porosity, these carbon fibers have dual functions of structural support and energy storage. To evaluate their capability of storing electrochemical energy, the fibers were tested by cyclic voltammetry (CV) in a three-electrode configuration using a reference electrode of Ag/AgCl. After pyrolysis at 800 °C under no tension, 'BCP sheath' carbon fibers exhibited the highest capacitance of 49 F g^{-1} (Figure 4.9). Under tension, however, the capacitance reduced to 19 F g^{-1} and 11 F g^{-1}

after pyrolysis at 800 and 1315 °C, respectively. The application of tension reduced the energy storage capability, which is explained by the increase in turbostractic ordering compared to the fibers produced without tension (Table 7). The phenomenon is attributed to factors including reduced quantum capacitance, screening of ions due to highly ordered turbostratic planes, as observed in previous studies.[127,153–155] Further, the reduced capacitance of fibers pyrolyzed at 1315 °C under tension was due to decreased pseudocapacitance from elimination of heteroatoms at high pyrolysis temperatures.[131] Nevertheless, the capacitance of porous carbon fibers from 'BCP sheath' produced under tension at 1315 °C was 70-90% higher than the commercially produced non-porous carbon fibers including T300 and IM7 (1 F g^{-1} and 3 F g^{-1}, respectively).[156] Thus, this study has opened potential pathway to satisfy the dual requirements of structural energy storage materials by deriving porous carbon fibers from gel-spun PMMA-b-PAN precursors.

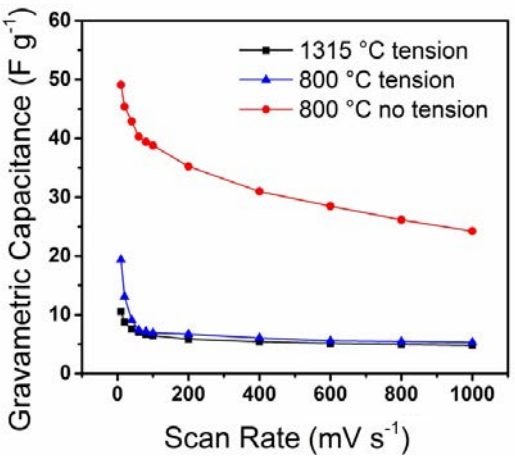

Figure 4.9. Capacitive rate capability for 'BCP sheath' carbon fibers after pyrolysis at 1315 and 800 °C with or without tension.

Considering the capacitance reduction upon tension, the electrochemical properties of non-tensioned carbon fibers prepared at 800 °C were focused upon. 'BCP

both' carbon fibers showed the highest capacitance followed by 'BCP sheath', 'BCP core', and 'PAN both', with gravimetric capacitances of 70, 49, 33, and 20 F g^{-1} at 10 mV s^{-1}, respectively (Figure 4.10a). To evaluate the rate capability, *i.e.*, the capacitance retained at higher charge/discharge rates, the scan rate was tested in the range 10 – 1000 mV s^{-1}. 'BCP sheath' carbon fibers displayed the highest retention rate (49%), followed by 'BCP both' (46%), 'BCP core' (35%), and 'PAN both' (18%) (Figure 10a) as the scan rate was increased from 10 to 1000 mV s^{-1}. Based on the Nyquist plot (Figure 4.10b) from electrochemical impedance spectroscopy (EIS), combined series resistances (R_s) were all low for 'PAN both' (0.6 Ω), 'BCP core' (0.8 Ω), 'BCP both' (1.2 Ω), and 'BCP sheath' (1.3 Ω) carbon fibers. Using the resistive perturbation of the carbon fibers, the diffusion resistance (σ) (Figure 4.10c) was also calculated for 'BCP sheath', 'BCP both', 'BCP core', and 'PAN both' corresponding to 5.3, 3.5, 2.5, and 6.2 Ω $s^{-0.5}$, respectively.

Within the potential window of 0.0 – 0.8 V *vs*. Ag/AgCl in an electrolyte of 3 M KOH, the electrodes were stable, showing no discernible redox peaks.[157] The absence of redox peaks suggests that electrical double layer dominates the energy storage process.[158] 'BCP both' carbon fibers showed the highest capacitance, owing to the largest surface area for adsorbing ions (264 m^2 g^{-1}) (Figure 4.3c). 'BCP sheath' possess the second highest pore surface area (27 m^2 g^{-1}) and thus second highest capacitance. 'BCP core' follows suit (2 m^2 g^{-1}) and finally 'PAN both', as expected, devoid of mesopores and thus the lowest capacitance.

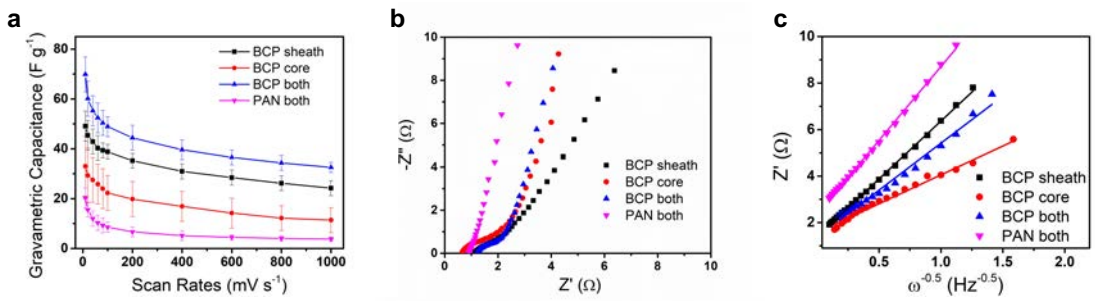

Figure 4.10. (a) Scan rate dependence of gravimetric capacitance, (b) Nyquist plots, and (c) diffusion resistance plot for 'BCP core', 'BCP sheath', 'BCP both', and 'PAN both' carbon fibers after pyrolysis at 800 °C without tension.

4.3.5. Factors influencing pore size

Tailoring the pore size of the carbon fibers is an effective way to balance the mechanical and electrochemical performance of the resultant porous carbon fibers. The pore sizes of carbon fibers produced in this study had a range from 13-30 nm, depending on the carbonization temperature and application of tension. While the gel-spinning of 'BCP both' polymer fibers in our study yielded carbon fibers with average pore size of ~ 25 nm, carbon fibers with average pore size of ~11 nm were derived from electrospun BCP fibers.[15] Another study of carbon film obtained through pyrolysis of BCP (molecular weight 161,000 g/mol) reported pore sizes in the range of 40 - 50 nm.[63] The pore sizes of these films differed based on either the solvent or temperature used for annealing. Table D1 lists the pore sizes of carbon fibers of a specific molecular weight obtained from the different configurations and conditions. Electrospun carbon fibers of BCP obtained by varying the molecular weight of BCP and the volume fraction of PAN

in the BCP, had pore sizes in the range of 10.9 - 18.6 nm (measured using N_2 physisorption).[132]

In effect, experimental factors including molecular weight and composition of BCP, method of obtaining the porous carbon fibers (electrospinning *vs* gel-spinning), processing conditions of BCP starting from the initial stages of polymeric fibers to the final steps of carbonization, seem to affect the pore size in the resultant carbon fibers. Pore size of the carbon fibers are driven by kinetically driven processing parameters, in addition to the thermodynamically driven phase separation between PMMA and PAN blocks. A computational study to discern the thermodynamic factor (interaction parameter) and subsequently the domain/pore size (characteristic correlation length) of PMMA in the BCP, for comparison with the experimentally observed pore sizes, was conducted.

4.3.6. Results of Computational Study

As shown in Figure 4.11, a decreasing $\chi_{i,j}$ with increasing molecular weights was observed, which agrees well with the previous reports.[159,160] For dimers of PMMA-*b*-PAN, $\chi_{i,j}$ was the highest for the PMMA Iso & PAN Iso pair (1.377) and the lowest for the Syn PMMA & Syn PAN pair (0.363). For trimer of PMMA-*b*-PAN, the atactic configuration was constructed, and the $\chi_{i,j}$ was calculated as 0.677, which fell between PMMA Iso & PAN Syn (0.830) and PMMA Syn & PAN Iso (0.494) pairs. Consequently, different molecular conformations produced different free energy of mixing for PMMA-*b*-PAN due to different conformational entropies, thus resulting in varied $\chi_{i,j}$ values. Following the calculation of $\chi_{i,j}$ for the trimer Ata PMMA-*b*-PAN, the extrapolated

value for the synthesized BCP with molecular weight ~160,000 g/mol resulted in 0.2932 (Figure D.9).

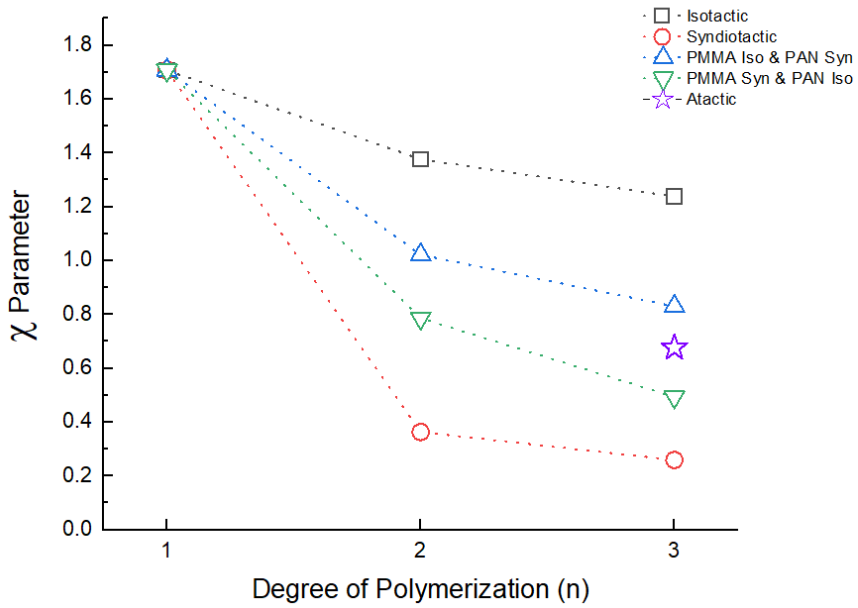

Figure 4.11. Calculated $\chi_{i,j}$ parameters for varied degree of polymerizations of PMMA and PAN blocks.

The phase separation between PMMA and PAN blocks of BCP was simulated using DPD simulation method as observed (Figure 4.12a), which agrees with earlier studies.[129,161,162] For the sake of simplicity in the simulations, the kinetic factors involving solvent evaporation effects, crosslinking of PAN during stabilization, thermal shrinkage during pyrolysis, *etc*., were not considered in the current study. Based on the predicted morphology, the RDF analysis and structure factor S(k) were implemented, which revealed the characteristic correlation length of PMMA-*b*-PAN to be ~20 nm.

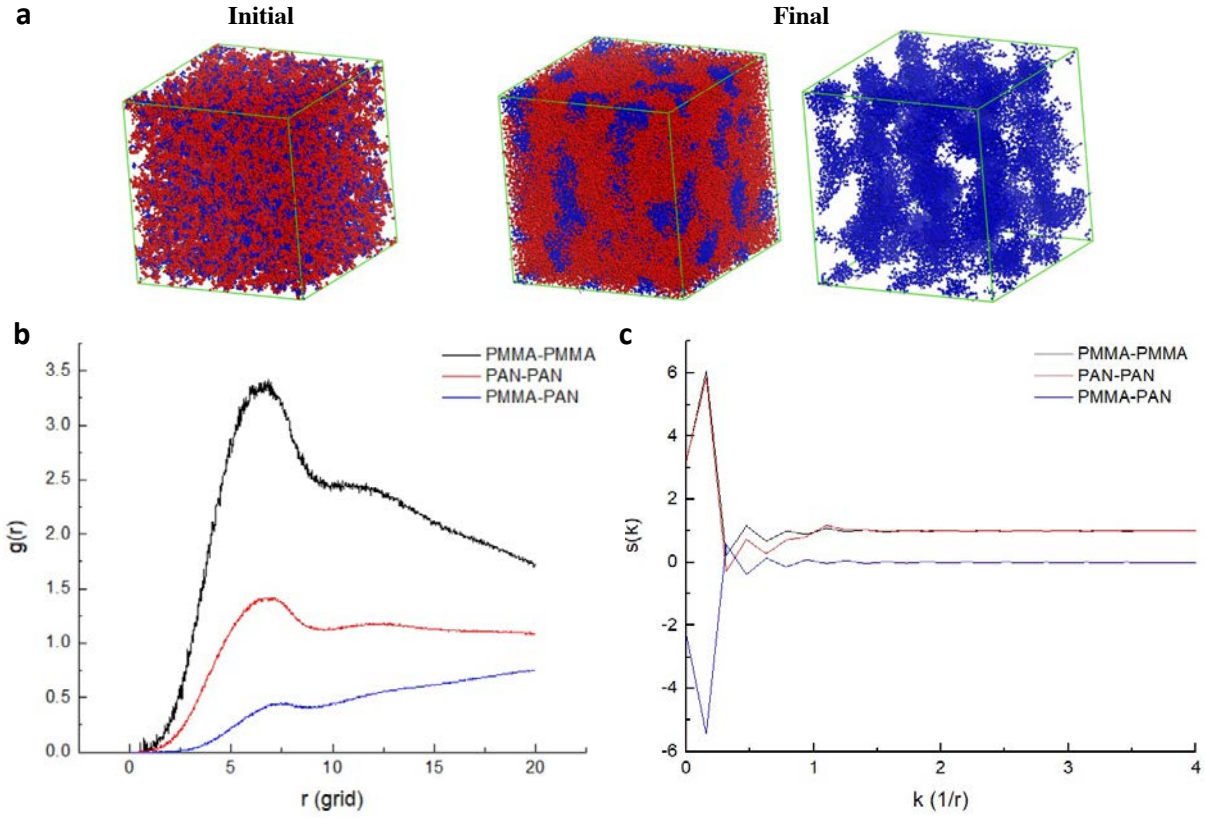

Figure 4.12. (a) Initial and final structures of PMMA-b-PAN after phase separation. Red and blue beads denote PMMA and PAN, respectively. For better visualization, PMMA beads were removed, (b) Radial distribution function (RDF) and (c) Structural Factor of PMMA-PMMA, PAN-PAN, and PMMA-PAN beads displayed in black, red, and blue line, respectively.

The characteristic correlation length of PMMA-*b*-PAN calculated from DPD simulations is in a good agreement with the experimentally determined pore sizes (10-30 nm), which were generated with decomposition of the sacrificial PMMA block. Although, in the experiments in this study, the phase separation of PAN and PMMA blocks may start during their dissolution process in solvent, and the domain size of PMMA could be further altered during the gel-spinning process (solvent removal in the coagulation bath, drawing of the polymer precursor fibers, crosslinking of PAN during stabilization, shrinkage accompanying pyrolysis *etc*.), please note that the DPD

simulations in this study pursue the thermodynamic equilibrium for phase separation only, to give an estimate of the pore sizes in the resultant BCP-derived carbon fibers.

4.4. Conclusion

Herein, four polymer fiber configurations utilizing both PMMA-*b*-PAN and PAN, including 'BCP sheath', 'BCP core', 'BCP both', and 'PAN both', were gel-spun. By systematically varying the carbonization temperature (800 and 1315 °C) and processing tension (tension and non-tensioned), the morphological, mechanical and electrochemical properties of the resultant carbon fibers were elucidated. Owing to the different rheological properties of PMMA-*b*-PAN and PAN, and their position in the polymer fibers, they revealed different cross-sectional and porous morphologies. Upon pyrolysis without tension, 'BCP sheath' carbon fibers showed a side-by-side morphology with elongated pores confined to a side; 'BCP core' carbon fibers exhibited elongated pores only in the interior encapsulated by non-porous exterior carbon sheath; 'BCP both' carbon fibers displayed well distributed elongated pores both on the interior and exterior; 'PAN both' carbon fibers were non-porous. Without tension, all BCP-containing fibers successfully produced porous carbon fibers after pyrolysis at 800 °C, with an average mesopore size of ~23 nm. Mechanically, 'BCP sheath' fibers showed tensile strength of 1.1 GPa, tensile modulus of 190 GPa, and electrochemical capacitance of 11 F g^{-1}, after pyrolysis at 1315 °C under tension. At a reduced pyrolysis temperature of 800 °C, the electrochemical capacitance increased slightly from 11 to 19 F g^{-1}. Among the BCP-derived carbon fibers, 'BCP both' carbon fibers after pyrolysis at 800 °C without tension achieved the best capacitance of 70 F g^{-1} at 10 mV s^{-1} among all gel-spun carbon fibers. In general, the application of tension and a high pyrolysis temperature improve the

mechanical properties but reduce the electrochemical performance of the carbon fibers. Pore size of the carbon fibers is influenced by kinetically driven processing conditions (type of spinning to get polymer precursor fibers, solvent evaporation effects, crosslinking of PAN during stabilization, thermal shrinkage during pyrolysis, *etc.)*, in addition to the thermodynamic phase separation between PMMA and PAN blocks. Interaction parameter, χ, (0.2932) and characteristic correlation length (~20 nm) of PMMA-*b*-PAN, as calculated from thermodynamically governed computational calculation, provide an estimate of the pore sizes observed in the experimentally obtained carbon fibers. Thus, gel-spinning of bicomponent fibers of PMMA-*b*-PAN and PAN provides an effective means for designing porous carbon fibers with controlled mechanical and electrochemical properties. Tailoring the pore size of BCP-derived carbon fibers by intertwining the thermodynamic and kinetic parameters could be focused in future studies for balancing their mechanical and electrochemical performance.

CHAPTER 5. PROCESSING CARBON FIBERS THROUGH GEL-SPINNING OF ASPHALTENES

5.1. Introduction

In Chapter 1, the motivation for using asphaltenes as carbon fiber precursor and their background were outlined. To the best of our knowledge, there are no prior studies on solution or gel spinning of asphaltenes with PAN, to obtain carbon fibers with good tensile properties. Solution or gel-spinning blend fibers of asphaltenes and PAN requires the preparation of homogeneous spinning solutions through the dissolution of both the components in a common solvent such as dimethylformamide (DMF), dimethylacetamide (DMAc), or dimethyl sulfoxide (DMSO) that have been used for solution or gel spinning of PAN fibers. Based on the solubility parameters reported in the literature, asphaltene solubility in DMAc or DMF is expected.[163] However, experimentally, it was found that as-received Alberta oil asphaltenes did not fully dissolve in these solvents, and instead created a suspension. Toluene dissolved the as received asphaltene, but it does not dissolve PAN. To enhance asphaltene's solubility in DMAc, controlling their dispersion or aggregation was studied from the perspective of creating functional groups on asphaltenes.[164,165] Asphaltenes have been chemically functionalized using ozone[164,166], nitric acid, and sulfuric acid.[165,167] Nitric and sulfuric acid functionalization has also been used for carbon nanotubes.[168,169]

In this study, functionalization in nitric acid was chosen over sulfuric acid, as it would result in the addition of polar groups that improve the compatibility of asphaltenes with polar solvents and polymers, and remove peripheral alkyl groups without increasing the

sulfur content.[165] Nitric acid functionalized asphaltenes (f-Asp) were soluble in DMAc and formed a homogeneous solution in PAN/DMAc. Blends of f-Asp/PAN with 30 and 60 wt% of f-Asp were successfully used to derive carbon fibers. Mechanical and structural properties of the precursor and carbon fibers were studied.

In addition to Asp/PAN blends, blend polymer fibers of Asp-polypropylene (PP) may be used for concrete reinforcement and other applications where the use of low-cost filers is beneficial (Appendix F).

5.2. Experimental

5.2.1. Materials

Alberta oil asphaltene, a solid powder (referred to as Asp), was provided by Alberta Innovates. Based on the safety data sheet (SDS), this sample was described as a 'mixture of (water) poly-aromatics & other hydrocarbons containing carbon (C), hydrogen (H), nitrogen (N), oxygen (O), Sulfur (S) and traces of metals with the following elemental composition: C 70-79%, H 7-8%, N 1.26-1.4%, S 7-8%, O 1.4-1.6%'. Poly(acrylonitrile-*co*-methacrylic acid) (PAN; viscosity average molecular weight, Mv: 500, 000 g/mol; 4% MAA content) was obtained from Japan Exlan, Co. Dimethylacetamide (DMAc) and nitric acid (HNO_3) purchased from Sigma Aldrich and methanol from VWR Chemicals, were used as received.

5.2.2. Functionalization of asphaltenes

10 g of as received asphaltene powder (Asp) was added to a 1 L round bottom flask along with 250 mL of nitric acid and 250 mL of de-ionized water (DIW). A stirrer

was added to the flask before setting up a reflux using a condenser and circulating water. The round bottom flask contents were refluxed at 120°C for 1, 2, 3, 6, 12 and 24 h. After functionalization, the contents were filtered and washed with DIW until a neutral pH of 7 was reached. The nitric acid functionalized asphaltenes were labeled as f-Asp. Asphaltene (2 h f-Asp) was used for spinning fibers, and then converting them to carbon fibers.

f-Asp was further functionalized using methanol (Appendix E.1) and labelled as f1-Asp. f1-Asp was not used in this study to spin fibers but is considered potentially a viable system for future studies.

5.2.3. Spinning of f-Asp/PAN blend fibers

Three fiber spinning trials (referred to as trials A, B, and C) were conducted using the f-Asp/PAN blends. In Trial A, bi-component fibers with two different spinning solutions for the core and sheath were prepared. Core solution was made by adding 17.25 g of f-Asp powder and 11.5 g of PAN powder in 100 mL of pre-chilled (~ 0 ºC) DMAc. f-Asp/PAN/DMAc slurry was gradually heated to 90 ºC in a silicone oil bath while being continuously stirred at 200 rpm. Upon reaching the temperature of 90 ºC, it was brought down to 70 ºC and stirred for 2h. This solution was degassed in vacuum at 70 ºC and had a pasty texture. After degassing, the solution was loaded into the spinning barrel. For the sheath solution of PAN, a slurry of 11.5 g PAN in 100 mL of pre-chilled (~ 0 ºC) DMAc was first prepared in a glass reactor. The slurry was then heated to 90 ºC using a silicone oil bath and stirred at 200 rpm for 2 h. The solution was then degassed in vacuum at 70 ºC and poured into the barrel of the spinning system.

For Trial B, 7.7 g of f-Asp was added to 15 mL of DMAc and then stirred at room temperature. In a glass reactor, 18 g of PAN was slowly added to 150 mL of pre-chilled (~ 0 ºC) DMAc. PAN/DMAc slurry was slowly heated to 70 ºC using a silicone oil bath and stirred for 2h at 200 rpm. f-Asp/DMAc solution was slowly added to the PAN/DMAc solution. Blend solution of f-Asp/PAN/DMAc was left to be heated at 45 ºC overnight, with continuous stirring at 50 rpm. Next day, the temperature of the blend solution was increased to 70 ºC and stirred for 1h. The blend solution of f-Asp/PAN/DMAc was then degassed in vacuum at 70 ºC and loaded into the spinning solution barrel.

The spinning solution for Trial C was prepared in a manner similar to Trial B. 22.5 g of f-Asp was dissolved in 45 mL of DMAc at room temperature with continuous stirring. To 100 mL of pre-chilled (~ 0 ºC) DMAc, 15.2 g of PAN was added. PAN/DMAc slurry was gradually heated to 70 ºC using a silicone oil bath and stirred for 2h at 200 rpm. Further, the f-Asp/DMAc solution was added to the PAN/DMAc solution and the temperature of the blend solution was reduced to 45 ºC. The blend was stirred overnight at 50 rpm and the temperature increased to 60 ºC the next day and stirred for 1h. Then, the solution was degassed in vacuum at 60 ºC before being poured into the barrel for spinning.

For Trial A spinning, a bi-component sheath-core fiber cross-section geometry was used, and the single component fiber geometry was used for Trials B and C. The core and sheath solutions, in the case of Trial A, were coaxially extruded through a 350 μm spinneret. The flow rates of the core and sheath solutions were 2.35 and 2 mL/min, respectively, that resulted in the core to sheath area ratio of ~72:28 For spinning Trials B and C, a 200 μm spinneret was used. The extruded filament passed through an air gap of

~ 5 cm, coagulated in a chilled methanol bath (maintained at about ~ -40 ºC) and then finally taken up on the plastic spools. In all the three trials, some leaching of asphaltenes (f-Asp) into the methanol coagulation bath was observed. These as-spun fibers were stored overnight in a chilled methanol vapor environment. As-spun fibers were then hot drawn in a glycerol bath at 160 - 167 º C (Trials A and B) and at 140-148 ºC (trial C) and referred to as the precursor fibers. The spinning parameters for all the three trials are listed in Table 5.1.

Table 5.1. Parameters used for spinning blend solutions of f-Asp/PAN in Trials A, B, and C.

Parameters	Trial A f-Asp/PAN (43/57) †	Trial B f-Asp/PAN (30/70) †	Trial C f-Asp/PAN (60/40) †
Solid Content (g/dL)	Core: 28.75 (f-Asp/PAN) Sheath: 11.5 (PAN)	16	26
Spinneret (μm)	350	200	200
Spinning Barrel temperature (ºC)	70	63	60
Spinneret temperature (ºC)	70	65	60
Viscosity at 1 rad/s (Pa.s)	Core: 38 Sheath: 254	72	64
Spin draw ratio (SDR)*	0.4 – 0.6	3	1.5
Hot draw ratio (HDR)	8	6	4
Total Draw ratio (TDR)*#	3.2 – 4.8	18	6
Precursor fiber designation	A-P	B-P	C-P

†Components in the blend are represented in terms of their weight %: f-Asp/PAN (wt. %/ wt.%).
*For Trial A – the fibers were collected over a range of collection speeds and hence the SDR and TDR are also reported as a range.
#TDR= SDR * HDR.

5.2.4. Stabilization and Carbonization

In a tube furnace (Model H17HT2.5x24, Micropyretics Heaters International, Inc), precursor blend fibers of f-Asp/PAN from the three trials (A-P, B-P, C-P) were stabilized in air and carbonized in nitrogen. The stabilization and carbonization protocols are summarized in Table E.1.

5.2.5. Characterization

Rheological behavior of the f-Asp/PAN blend solutions was characterized using ARES Rheometer, in a parallel-plate configuration (50 mm plate diameter and 1 mm gap between the plates). Dynamic frequency sweeps from 0.63 rad/s to 300 rad/s were performed on the solutions at a constant strain of 1% and room temperature. Asp, f-Asp and f1-Asp powders were dried in vacuum at 90 °C for several days. Thermogravimetric analysis (TGA) was performed on these samples at a heating rate of 10 °C/min under a nitrogen atmosphere using a TA Instruments TGA Q500. Thermo Scientific Nicolet iS5 Spectrometer in the attenuated total reflectance (ATR) mode was used for FTIR study. The FTIR data was collected at a resolution of 4 cm^{-1} over the range of 400 to 6000 cm^{-1}.

2-5 mg of Asp, f-Asp, and f1-Asp powder samples were each mixed with 200 µL of HPLC grade toluene, and 1µL of the solution was placed on a stainless-steel target plate. Laser desorption ionization mass spectrometry was performed using a Bruker Daltonics 12T SolariX Fourier Transform Ion Cyclotron Resonance (FT-ICR) mass spectrometer. The data was collected in positive mode with an average of 24 spectra at 30% laser power and 1 million resolution. The data was smoothed to 0.05 m/z and peaks were picked using a threshold of Signal/Noise (S/N) > 10 and a minimum absolute intensity of 100,000 counts.

Tensile properties of the drawn precursor and the carbon fibers were measured on the RSA III solids analyzer, by mounting the individual filaments on paper tabs with a gauge length of 25.4 mm for the precursor fibers and 12.6 mm for the carbon fibers. Strain rates of 1 %/s and 0.1%/s for the tensile test of the precursor and carbon fibers,

respectively were used. Cross-sectional and surface morphologies of the carbon fibers were imaged on a HITACHI SU8230 scanning electron microscope (SEM) (accelerating voltage of 2 kV and working distance of ~ 4 -6 mm). Wide-angle X-ray diffractions (WAXD) patterns of asphaltene powders, asphaltene solutions (in DMAc), precursor and carbon fibers were obtained on a Rigaku MicroMax 002 X-ray generator (Cu Kα radiation, λ = 1.5418 Å, 50 kV and 0.6 mA) equipped with a R-axis IV++ detector.

5.3. Results and Discussion

5.3.1. Properties of functionalized asphaltenes

The chemical structures of the as-received asphaltenes (Asp), nitric acid functionalized asphaltenes (f-Asp), and transesterified asphaltenes (f1-Asp) were studied from their FTIR spectra (Figure 5.1). Upon functionalization, f-Asp showed peaks of C═O stretching (1625–1800 cm^{-1}), C–O stretching (1000–1260 cm^{-1}), and NO_2 (1533, 1340 cm^{-1}), that were absent in Asp. The absorbance intensity of these peaks increased as the time of nitric acid functionalization increased. In addition, the spectra of f-Asp showed absorption bands at 1715 and 1005 cm^{-1}, associated with stretching and bending vibrations of ester and carboxy groups.[164] On the other hand, the intensity of the aromatic C–H peak (2850–2950 cm^{-1}) and the $-CH_2$/$-CH_3$ asymmetric deformation peak (1452 cm^{-1}) were reduced by nitric acid functionalization consistent with the results of Ignatenko et al.[165] The modification of the chemical structure of the as-received asphaltenes through functionalization in nitric acid resulted in their dissolution in DMAc, and in a homogeneous solution with PAN.

f1-Asp showed reduction in the 1005 cm^{-1} peak absorbance intensity associated with stretching and bending vibrations of ester and carboxy groups in addition to an increase in the 1193 cm^{-1} and 1452 cm^{-1} peaks responsible for the O−C stretch and the CH_3 asymmetric deformation of the O−CH3 group, respectively.[170] f1-Asp was not soluble in methanol but was soluble in DMAc.

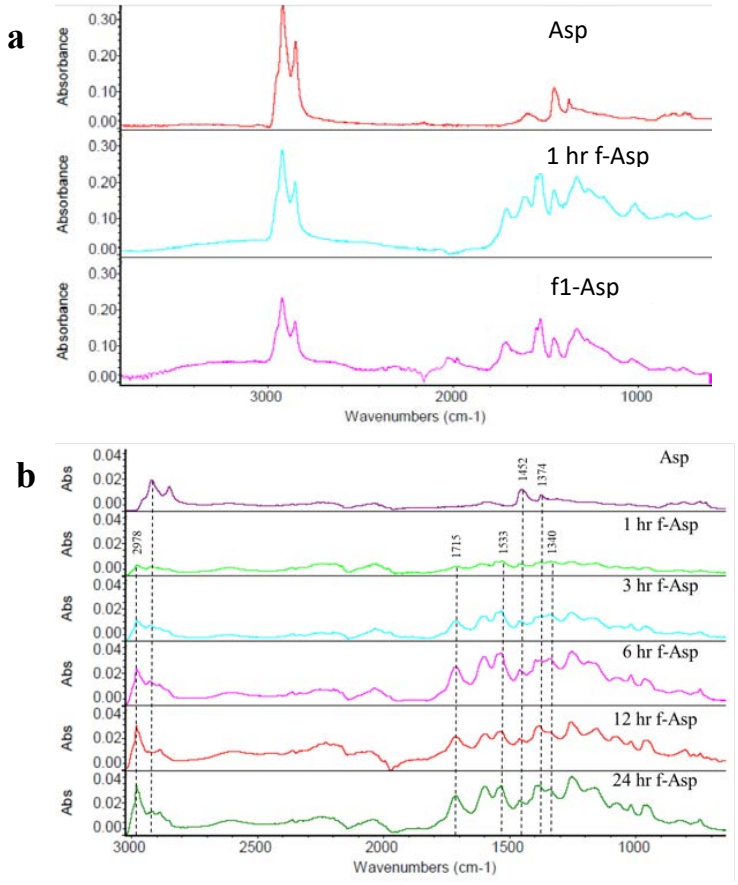

Figure 5.1. FTIR spectra of (a) Asp and f-asp after various times of functionalization in nitric acid and, b) Asp, f-Asp, and f1-Asp.

MALDI was used to evaluate the molecular weights of the as-received, nitric acid and methanol functionalized asphaltenes. Figure 5.2 shows that some degradation in molecular weight occurred during nitric acid functionalization, as Asp's molecular

weight was 1402 g/mol while for 1 h and 6 h f-Asp samples, the values were 1210 and 1170 g/mol, respectively. On the other hand, the 24 h f-Asp sample had a marginally higher molecular weight of 1303 g/mol than the other f-Asp. The asphaltene after 24 h methanol functionalization showed an increase in molecular weight to 1997 g/mol, offering further evidence of successful transesterification as -OH groups were replaced with $-OCH_3$ groups.

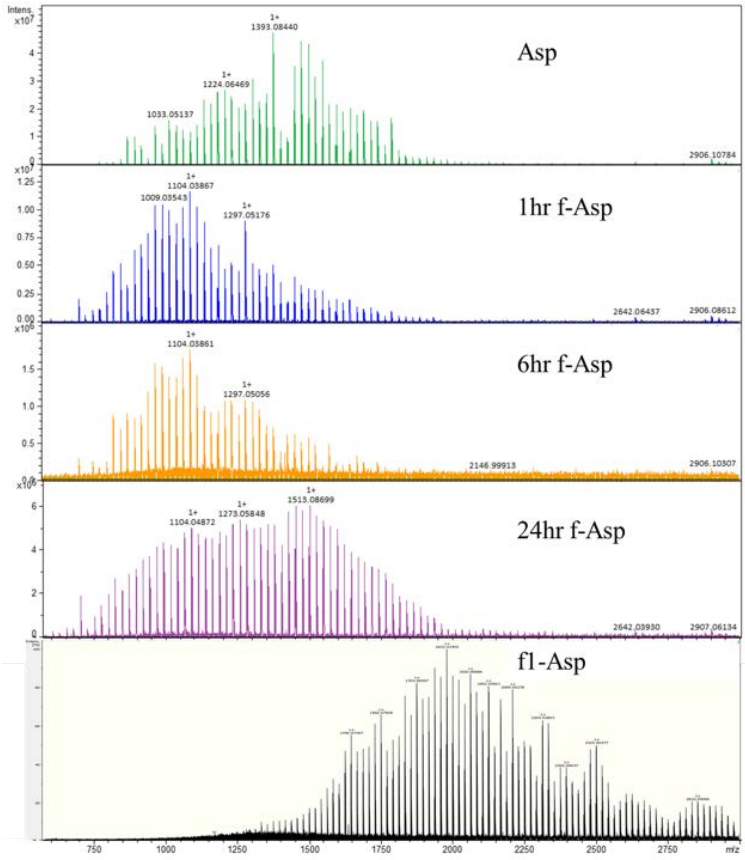

Figure 5.2. MALDI spectra of the as-received (Asp), nitric acid treated (f-Asp) and methanol treated (f1-Asp) samples.

Figure 5.3 shows the thermal degradation of Asp, f-Asp, and f1-Asp. As-received Asp lost less than 10% of the weight before 350 °C and ~ 52% of the weight between 350 and 500 °C. The degradation of all f-Asp and f1-Asp started at a lower temperature, just

above 100 °C and continued steadily thereafter, due to the added functional groups. Overall, f-Asp and f1-Asp retained higher weight above 500 °C, than the Asp.

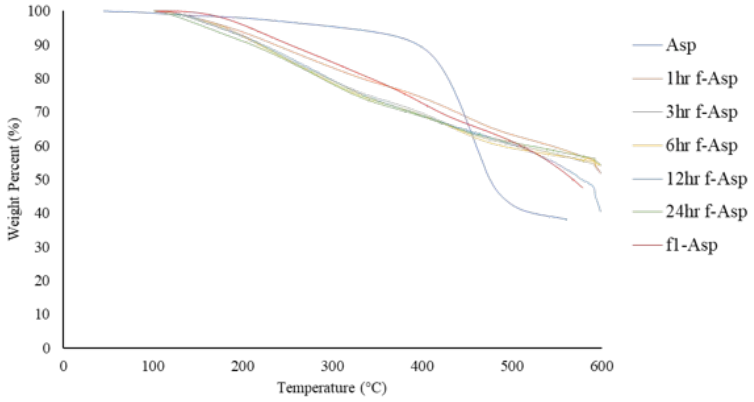

Figure 5.3. TGA of Asp, f-Asp, and f1-Asp samples.

5.3.2. Structural characterization of asphaltenes and their solutions

Literature reports of asphaltenes show three wide angle X-ray diffraction (WAXD) peaks at 2θ of ~11 – 20° (referred to as γ band), ~ 26° (002 plane), and ~43° (10 plane).[171,172] Asphaltene molecules with aromatic cores and aliphatic side chains tend to form nano aggregates due to stacking of the aromatic core molecules through π-π interactions, and this gives rise to the WAXD peaks at 2θ of ~ 26° (aromatic core stacking) and ~11 – 20° (aliphatic chain stacking).[173,174] These stacked nanoaggregates further form clusters and the behavior of these clusters is altered due to interaction with surrounding environment, like solvents.[175] As received asphaltene powder showed all the three peaks distinctly, while the f-Asp exhibited a merged peak of the gamma band and 002 plane (Figure 5.4a). Figure 5.4b shows the WAXD scans of asphaltene solutions in DMAc. Integrated WAXD scans for the powders and solutions were obtained by

subtracting the diffraction from a background of the glass capillary that was used for holding the samples for WAXD study.

The structural parameters are listed in Table 5.2. Interestingly, the stacking size of the aromatic cores (L002) decreased from 2.2 to 0.8 nm upon functionalization and the solutions of asphaltenes also presented cluster sizes ~0.7 – 0.8 nm. This suggests that aromatic stacking of cores is reduced as they are broken due to functionalization.

Another parameter, aromaticity (Ar*) in equation 5.1, defined as the ratio of 002 peak area to that of the area of γ and 002 peaks, is typically used to indicate the fraction of aromatic carbon in asphaltenes that are capable of stacking.[173] This study uses the designation of Ar* for aromaticity instead of the commonly used literature designation, f_{ar}. This is done to avoid confusion with the use of the term '*f*' (f_{PAN} *or* f_{002}) denoting orientation in this dissertation.

$$Ar^* = \frac{A_{002}}{A_{002}+A_{\gamma}} \tag{5.1}$$

It is important to note that the aromaticity Ar* is not based on all the aromatic carbon in asphaltene but instead based exclusively on the stacked aromatic cores that contributes to the 002 peak. As-received asphaltene's aromaticity of 0.19 increased to 0.27 upon nitric acid functionalization (f-Asp). Aromaticity of f-Asp and f1-Asp further increased marginally to ~0.31-0.35 on dissolution in DMAc.

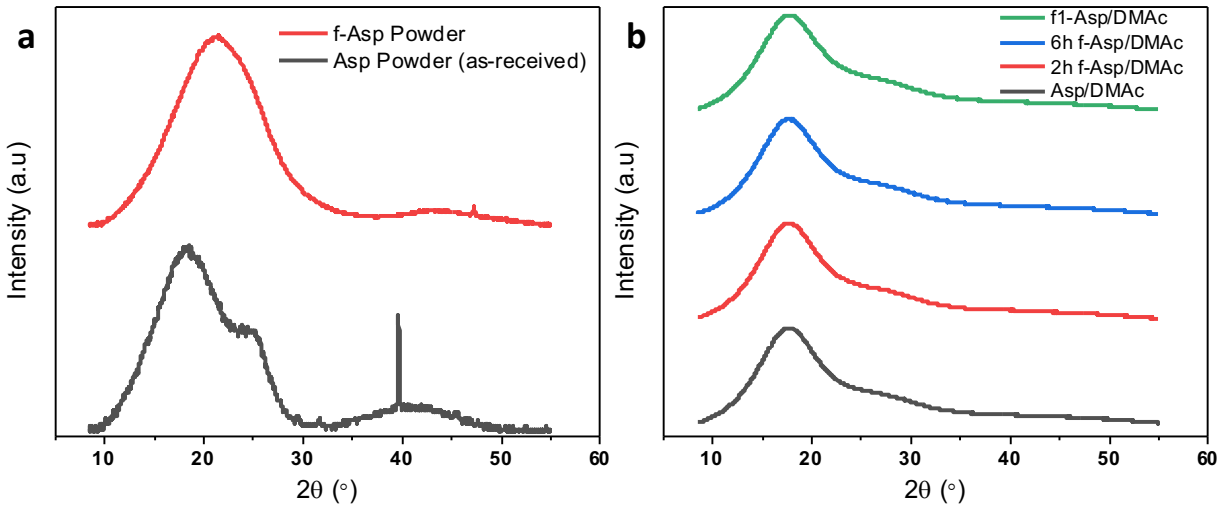

Figure 5.4. Integrated WAXD scans. (a) as received Asp and f-Asp powders, (b) Asp, f-Asp and f1-Asp solutions (1 g/10 mL) in DMAc.

Table 5.2. Structural parameters of asphaltene powders and solutions in DMAc (1 g/10 mL).

	Asp	f-Asp	Asp/DMAc	2 h f-Asp /DMAc	6 h f-Asp /DMAc	f1-Asp/ DMAc
d_{γ} (nm)	0.478	0.426	0.506	0.505	0.506	0.505
d_{002} (nm)	0.354	0.366	0.347	0.347	0.349	0.352
L10 (nm)[a]	1.0	0.9	0.4	0.4	0.4	0.5
L002 (nm)[b]	2.2	0.8	0.7	0.8	0.7	0.7
Ar*	0.19	0.27	0.31	0.31	0.32	0.35

[a] Crystal size of (10) plane at 2θ ~ 43°, and [b] (002) plane at 2θ ~ 26°, according to Scherrer's equation with K = 0.9.

5.3.3. Rheological behavior of asphaltene solutions

The terminal slope (when test frequency $\omega \rightarrow 0$) of log G′ (storage modulus) versus log G″ (loss modulus) curve, also known as a modified Cole-Cole plot (Figure 5.5a), can be used quantitatively to study the solution homogeneity, and a slope ~2 indicates the upper limit.[85,176,177] Slopes calculated for f-Asp/PAN solutions of Trials A (core solution), B, and C are 0.9, 1.5 and 1.4, respectively. Higher slope value suggests higher degree of solution homogeneity. The core solution of Trial A with the lowest slope of 0.9, was the least homogenous solution. During the solution preparation, the maximum temperature of f-Asp/PAN blend solutions was 90 °C for Trial A while it was 70 °C for Trials B and C. Exposure to higher temperature of the spinning solution in Trial A likely reduced the solubility of some of the asphaltene clusters in DMAc and induced their phase.[178] This phase separation of the asphaltene clusters lead to pasty texture of the solution of Trial and the resulting inhomogeneity. Figure 5.5b shows the complex viscosity of f-Asp/PAN and PAN solutions as a function of angular frequency. Viscosity of core solution with f-Asp/PAN blend of Trial A was lower than both trial B and C. Reduction in viscosity of asphaltene solutions was observed in an earlier study due to decreased solubility of saturate/aliphatic components and an increased cluster size.[174] Similar phenomenon could explain the reduced viscosity and the phase separation of such components leading to inhomogeneity in the f-Asp/PAN solution of Trial A.

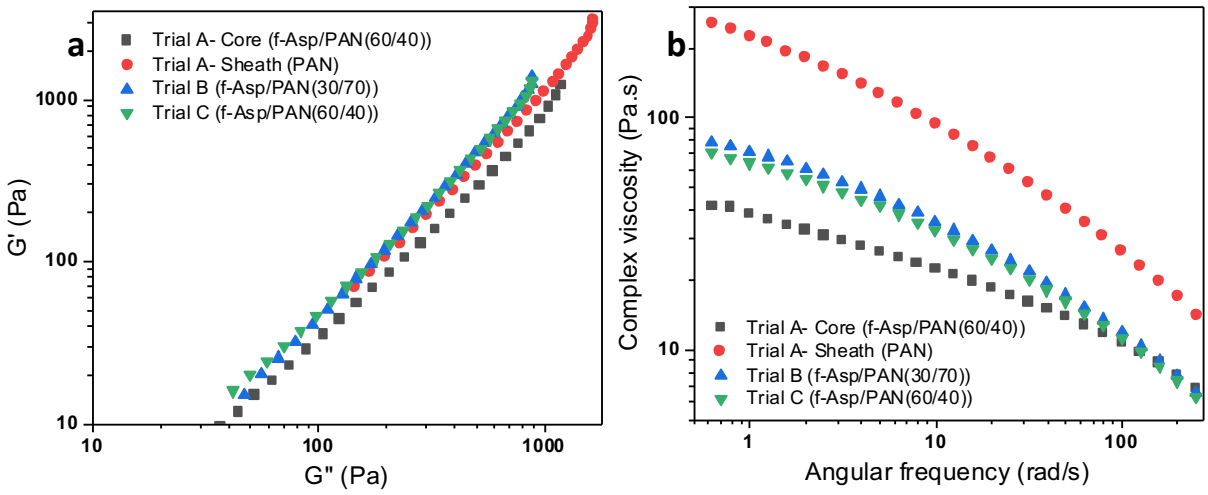

Figure 5.5. Rheological behavior of f-Asp/PAN blend solutions. (a) Modified Cole-Cole plot, (b) complex viscosity as a function of angular frequency.

5.3.4. Mechanical properties and structural parameters of precursor fibers

The mechanical properties and structural parameters of the drawn precursor fibers were first evaluated and are listed in Table 5.3. The inhomogeneity of the spinning solution, as elucidated by the slope of the modified Cole-Cole plot for Trial A, was translated into the precursor fibers, as well. Consequently, amongst the three spinning trials, A-P fibers presented the largest variation in their diameters, tensile strength and modulus. A-P fibers, with the highest solid content and the larger spinneret diameter, had the highest diameter and the lowest draw ratio of the three fibers. C-P fibers with twice the asphaltene content as B-P fibers, showed 45 % and 40 % reduction in the tensile strength and modulus, respectively, compared to B-P fibers. Differently, A-P fibers with ~43 wt.% f-Asp overall had tensile strength comparable to the C-P fibers which contained 60 wt.% f-Asp. This is likely a result of higher degree of solution

inhomogeneity in trial A. The precursor tensile modulus was also highest for trial B, and was comparable for trials A and C.

Structural parameters of the precursor fibers were influenced by the overall amount of f-Asp in the fiber (Table 5.3). B-P fibers with the lowest amount of amorphous f-Asp showed the highest crystal size, and orientation, supporting the trend of the tensile modulus. Ratio of the d-spacing of 2θ ~17° and 30° peaks of PAN ($d_{17°}/d_{30°}$), closer to 1.732, indicated a hexagonal packing structure of the PAN crystal for A-P and B-P fibers with <50 wt% of f-Asp and orthogonal structure in C-P fibers with >50 wt% of f-Asp.[90] Thus, amount of f-Asp in the blend influenced the PAN crystal structure.

PAN's characteristic WAXD peaks at 2θ ~17° and ~30° were present in all the three precursor fibers as expected (Figures 5.6). A-P also showed a peak at 2θ ~13° (d-spacing: 0.671 nm) with no preferential orientation and appears to be characteristic of the asphaltene gamma band (2θ ~11-20°, d-spacing ~0.5 nm) than arising due to PAN. This peak was absent in the B and C precursor fibers. This is likely due to the phase separation of aliphatic/saturate clusters of f-Asp, consistent with the inhomogeneity of the solution and its lowered viscosity.

Table 5.3. Mechanical properties and structural parameters of various drawn precursor fibers.

	A-P f-Asp/PAN (43/57)	B-P f-Asp/PAN (30/70)	C-P f-Asp/PAN (60/40)
TDR	3.2 - 4.8	18	6
Diameter (μm)	77 ± 7	15.7 ± 0.6	31.7 ± 0.7
Tensile strength (MPa)	205 ± 44	361 ± 29	197 ± 13
Tensile modulus (GPa)	7.8 ± 1.6	11.7 ± 0.7	7.0 ± 0.5
Elongation at Break (%)	7.1 ± 0.9	6.4 ± 0.6	9.2 ± 0.6
PAN Crystallinity (%)[a]	50	55	39
PAN Crystal size (nm)[b]	7.9	8.6	6.7
f_{PAN}[c]	0.75	0.78	0.55
$d_{17°}/d_{30°}$[d]	1.728	1.727	1.722

[a] Crystallinity is calculated by excluding amorphous contributions from both PAN and f-Asp (γ band) from PAN's crystalline peaks.
[b] Crystal size of PAN at 2θ ~17° (200) and (110) planes.
[c] Herman's orientation factor of PAN calculated from the azimuthal scan of PAN (200) and (110) planes (and adding the contribution after deconvolution of the 2θ ~17° peak from the meridional scan in the case of C-P fiber).
[d] Ratio of d-spacing of diffraction peaks at 2θ ~17° and ~30°

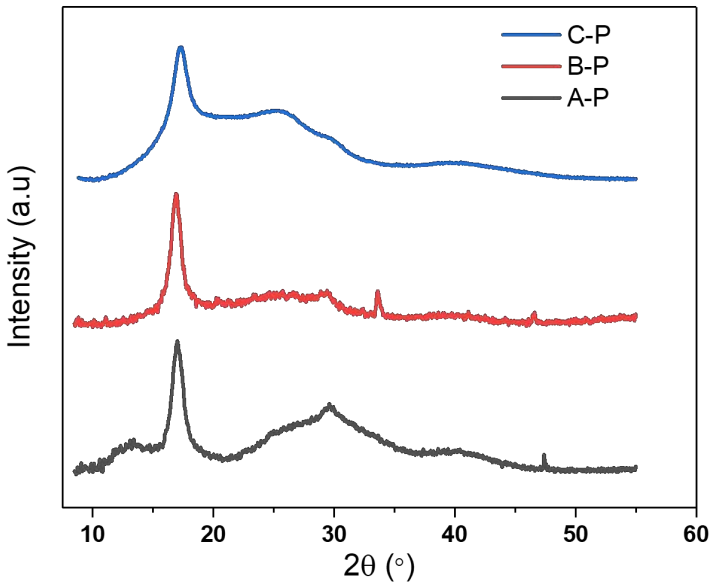

Figure 5.6. Integrated WAXD scans of drawn precursor f-Asp/PAN fibers, as indicated.

5.3.5. Structural characterization of stabilized fibers

Common characteristics in the WAXD (Figure 5.7) of all the stabilized fibers, excluding A-S fibers, were the high intensity 2θ ~26° peak and the relatively low intensity 2θ ~43° peak. Strong peak around 2θ ~13°, that was also present in their precursor fibers, was observed in the A-S fibers. Further aggregation of the phase separated aliphatic clusters of f-Asp seemed to have become more dominant with the increase in temperature during the stabilization protocol. PAN's characteristic 2θ ~17° peak was absent in all the stabilized fibers, indicating a complete stabilization.

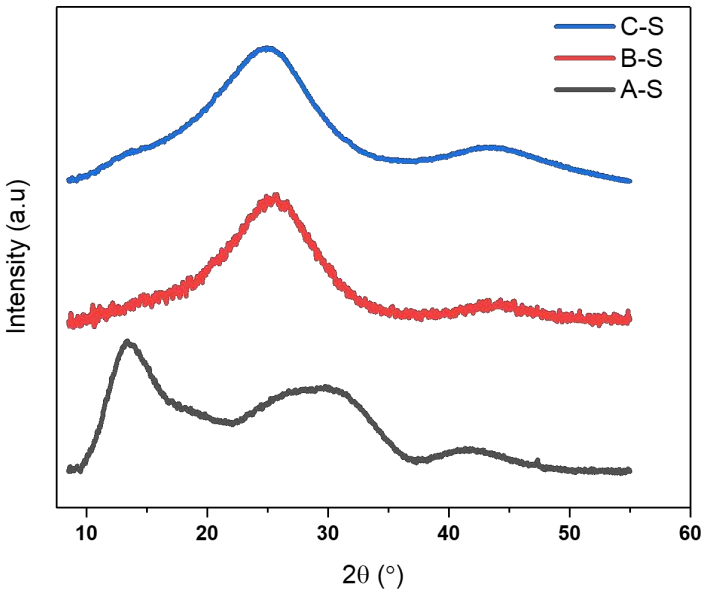

Figure 5.7. Integrated WAXD scans of stabilized fibers, as indicated.

5.3.6. Morphology of carbon fibers

SEM cross-sections of B-C carbon fibers did not exhibit significant porosity (Figure 5.8a-d). On the other hand, while certain sections of the surface were smooth and non-porous, other surface sections showed some porosity (Figure 5.8e-h). Pores with average diameters of 0.6 μm were observed in the cross-section and surface of C-C (Figure 5.9) fibers. Porous morphology played a role in reducing the mechanical properties of these fibers and suggest that further optimization is needed for processing these precursor and carbon fibers.

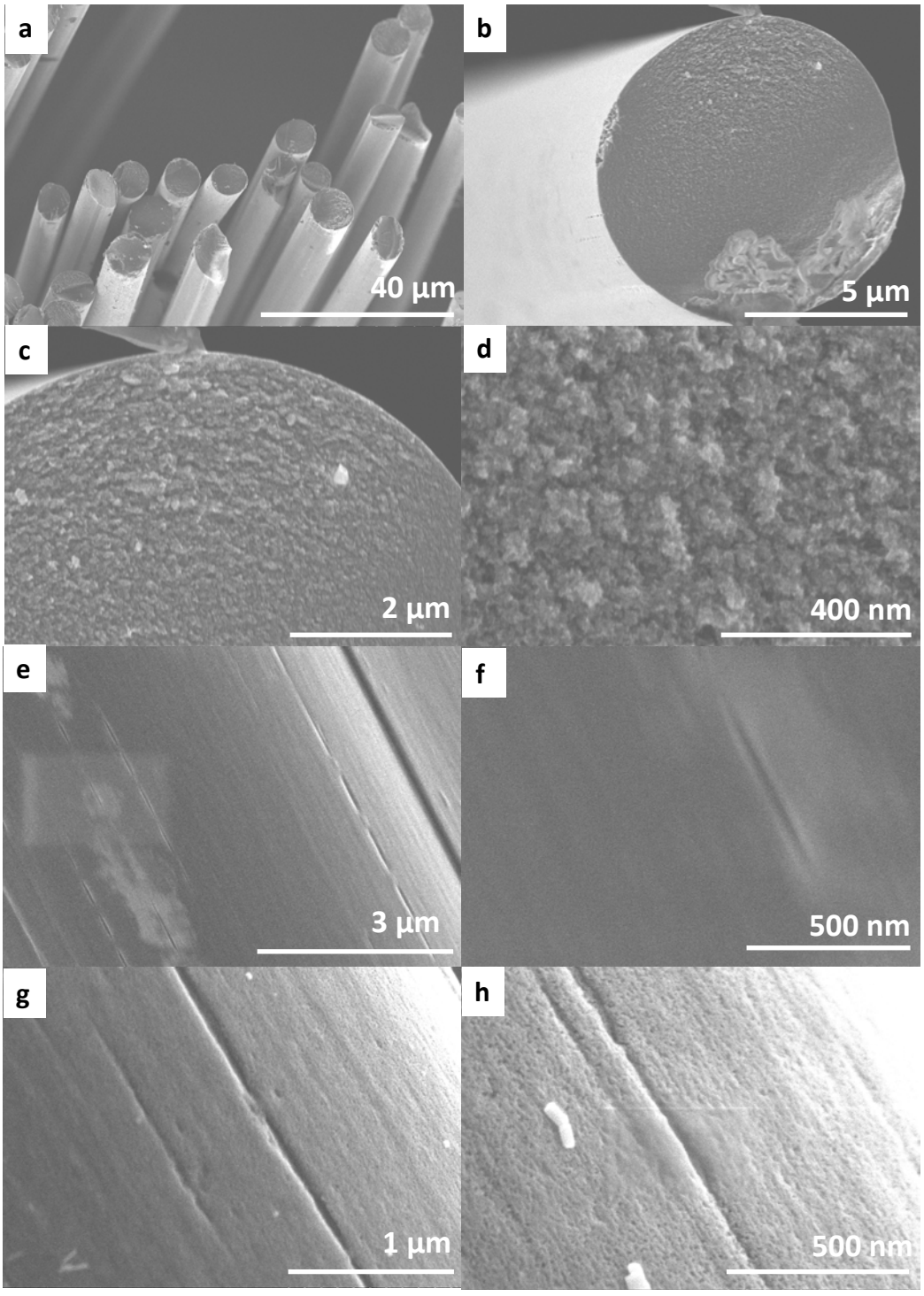

Figure 5.8. Cross-sectional (a-d) and surface (e-h) SEMs of B-C fibers.

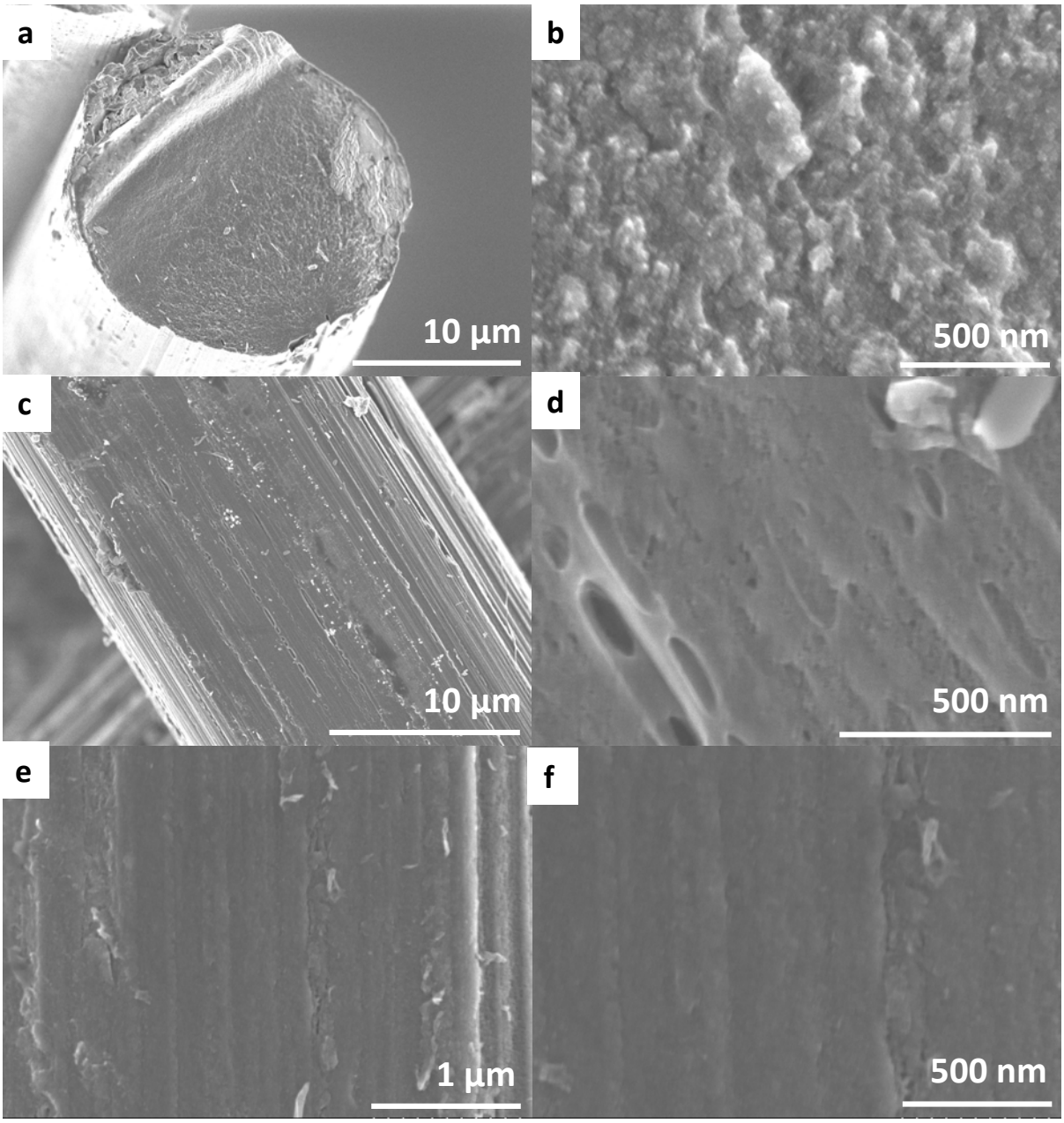

Figure 5.9. Cross-sectional (a-b) and surface (c-f) SEMs of C-C fibers.

5.3.7. Mechanical properties and structural parameters of carbon fibers

Carbon fibers with good structural integrity were not produced from the A-P precursor fibers. A-C fibers were found to be broken and crimped at the end of the carbonization, and their mechanical properties could not be measured. With a tensile

strength as high as 1.1 GPa and tensile modulus as high as 181 GPa, B-C fibers showed the best mechanical properties of the carbon fibers produced in this study. Better mechanical properties of B-C in comparison to C-C fibers are attributed to higher content of PAN in the B-P fibers than in C-P fibers along with the absence of significant porosity in B-C fibers (Table 5.4). Carbon fibers from coal sourced asphaltenes that were converted to mesophase pitch, melt spun and pyrolyzed at 1000 °C had tensile strength in the range of 0.8-1.1 GPa.[73,74] There is further scope to improve the tensile properties of carbon fibers obtained by solution or gel spinning of petroleum based asphaltenes. B-C fibers showed higher orientation of the turbostratic graphitic planes than the C-C fibers, consistent with their tensile modulus (Table 5.4). Optimizing the influencing factors including purity of the as-received asphaltenes, tension, stabilization protocol and content of f-Asp in the blends are to be considered for improving the mechanical properties of carbon fibers from asphaltene precursors.

Table 5.4. Mechanical properties and structural parameters of f-Asp/PAN blend carbon fibers.

	B-C f-Asp/PAN (30/ 70)	C-C f-Asp/PAN (60/ 40)
Diameter (μm)	8.1 ± 0.2	19.7 ± 0.8
Tensile strength (GPa)	1.1 ± 0.5	0.5 ± 0.3
Tensile modulus (GPa)	181 ± 33	123 ± 69
Elongation at break (%)	0.6 ± 0.3	0.6 ± 0.3
L002 (nm)[a]	1.45	1.56
L10 (nm)[b]	1.91	2.2
f_{002}[c]	0.73	0.68

[a] Crystal size of (002) plane at 2θ ~ 26°, according to Scherrer's equation with K = 0.9.
[b] Crystal size of (10) plane at 2θ ~ 43°, according to Scherrer's equation with K = 0.9.
[c] Orientation factor of (002) plane calculated from the azimuthal scan

Characteristic WAXD carbon fiber peaks at 2θ ~26° (002) and 43° (10) were observed in the carbon fibers produced in the study (Figure 5.10). Some B-C fibers occasionally showed additional peaks in their WAXD scans (Figure E.6). As-received asphaltenes were reported to contain ~8% of sulfur along with trace quantities of metals. The non-carbon diffraction peaks could arise from sulfur, trace metals, and other residual impurities remaining after pyrolysis. Some B-C fibers also showed particles (average diameter: 26 nm) or fibrils (average diameter: 17 nm) (Figure E.7). These particles or

fibrils are most likely composed of some of the impurities and likely result in some of the WAXD peaks in these fibers. Further elemental analysis of the B-C fibers is required to isolate the source of these additional peaks and ascertain the hypothesis. Some morphological features were also occasionally found on the surface of C-C (Figure E.8), but they did not manifest themselves in non-carbon WAXD peaks (Figure E.10), unlike in the case of some of B-C fibers. Hence, further work may be needed in purifying and treating asphaltenes, to improve their mechanical performance and structural properties.

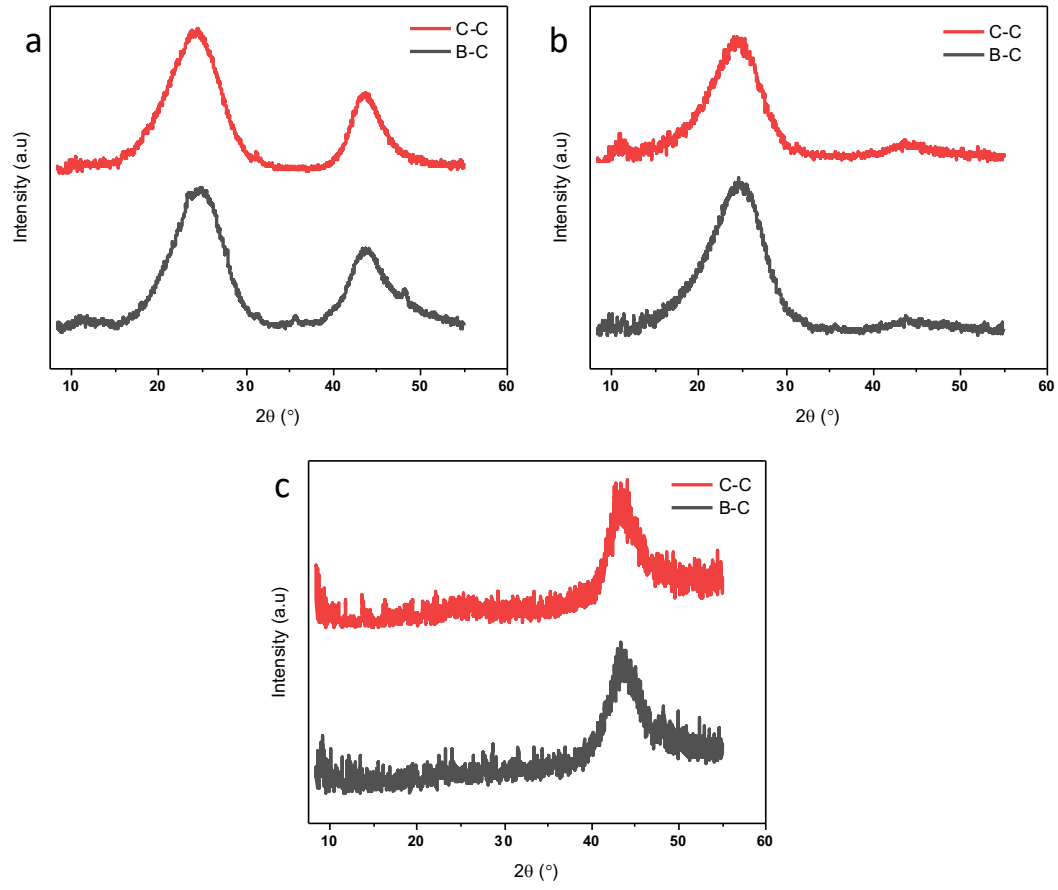

Figure 5.10. (a) Integrated, (b) equatorial and (c) meridional WAXD scans of carbon fibers, as indicated.

5.4. Conclusion

The as-received Alberta oil asphaltenes (S1; Asp), were not fully soluble in DMAc, DMF or DMSO. Functionalization of asphaltenes through nitric acid resulted in successful asphaltene dissolution in DMAc and further aided in the preparation of relatively homogenous blend solutions with PAN. Asphaltenes (f-Asp) functionalization was confirmed using FTIR. Fibers were spun from f-Asp/PAN blends. Carbon fiber tensile strength and modulus from the f-asp/PAN blends were in the range of 0.5 to 1.1 GPa, and tensile modulus was in the range of 123 to 181 GPa. This study opens avenues to use asphaltenes as carbon fiber precursors through potentially scalable route of solution/gel spinning of functionalized asphaltenes while blending with polyacrylonitrile. Using higher purity asphaltenes, tuning the blend ratio of functionalized asphaltene and PAN, using methanol functionalized asphaltenes, spinning bicomponent fibers with homogeneous solutions and optimizing stabilization/carbonization conditions, are some of the potential pathways to improve the properties of the asphaltene based carbon fibers, beyond what has been done in this study.

CHAPTER 6. CONCLUSIONS AND RECOMMENDATIONS FOR FUTURE WORK

6.1. Conclusions

The objective of this dissertation was to study the development of high-performance, lightweight and low-cost carbon fibers to achieve SDGs of clean energy, climate change and infrastructure. Two different approaches were taken towards light weighting automobiles by designing carbon fibers with the potential to replace steel/aluminum. First, porous carbon fibers from gel-spun precursors of PAN-sacrificial polymer blends and PAN-block copolymer systems studied for light weighting and energy storage applications. The second approach involved the use of precursor blends of asphaltene and PAN, to design strong carbon fibers from low-cost precursors.

In Chapter 2, blends of PAN with sacrificial polymers were first studied for their potential to derive porous carbon fibers with density lower than solid fibers but having mechanical performance equivalent to that of their non-porous counterparts. Out of five different sacrificial polymers, three systems including PAA, PMMA and SAN were particularly chosen based on their intermediate and higher degree of compatibility with PAN, deduced from their UV- Visible spectroscopy. Choice of sacrificial polymer and blend ratio affected the viscosity of blend solutions, and draw ratio, tensile strength, crystallinity, and crystal packing of the precursor blend fibers. Pore size and pore shape of resulting carbon fibers differed based on the choice of sacrificial polymer and blend

ratio. The following porous morphologies were revealed by the carbon fibers derived from the three different sacrificial polymer systems: PAA- nearly circular and non-elongated pores; PMMA: elongated pores; SAN- porous channels. The average pore diameter in carbon fibers obtained from PAN-PAA (90/10), PAN-PMMA (90/10) and PAN-SAN (90/10) were 15 nm, 31 nm and 37 nm, respectively. Degree of compatibility between the polymer pairs in the blend evaluated through both an experimental viscosity study and theoretical study of interaction parameters, yielded the same result. Polymer blends with higher viscosity and lower interaction parameter had higher degree of compatibility. It was further established that pore size was inversely proportional to the degree of compatibility between PAN and the sacrificial polymer. Pore size increased from 37 nm to 115 nm upon increasing the amount of SAN from 10 wt% to 20 wt% in the blend. Porous carbon fibers from PAN-PAA and PAN-PMMA had tensile strength (~1.6 GPa) and tensile modulus (~280 GPa) closer to that of the non-porous carbon fibers obtained from PAN (~2.0 GPa and ~270 GPa) processed under comparable conditions. Specific tensile modulus of the porous carbon fibers from PAN-PAA and PAN-PMMA was 15 to 40 % higher than that for the PAN based carbon fibers, and the electrical conductivity was as high as 74 kS/m due to high graphitic ordering.

Carbon fibers from PAN-SAN systems with unique porous morphology were produced in Chapter 2 but their mechanical properties could not be measured. In Chapter 3, the tensile properties of porous fibers from PAN-SAN system were improved by gel-spinning precursor fibers with 5 wt% of SAN. Four different carbon fibers were produced from PAN-SAN (95/5) precursor fibers by varying the conditions of pyrolysis: carbonization temperature and application of tension. All the four different porous carbon

fibers exhibited porous channeled morphology, as observed in PAN-SAN derived carbon fibers of Chapter 2. Application of tension was critical to improving the tensile performance as the properties of only PAN-SAN (95/5) fibers carbonized under tension could be measured. Tensile strength and modulus of carbon fibers (carbonized at 1315 °C, with tension) from PAN-SAN (95/5) were 0.9 GPa and 165 GPa, respectively. Porous PAN-SAN derived carbon fibers with specific strength and modulus that was about half that of the non-porous PAN based carbon fibers were obtained by adjusting only the blend ratio.

Next, in Chapter 4, the morphological, mechanical and electrochemical properties of a series of porous carbon fibers from PAN and PMMA-*b*-PAN were studied. Four configurations of polymer fibers were first gel-spun using both PAN and PMMA-*b*-PAN, including 'BCP sheath', 'BCP core', 'BCP both', and 'PAN both'. Thermomechanical and structural performance of polymer precursor fibers were dictated by the composition of BCP and its configuration. Then, a series of carbon fibers were produced from the polymer fibers by systematically varying the carbonization temperature and the application of tension. Morphology of resulting carbon fibers (side by side vs core-sheath) was influenced by viscosity of PAN and BCP as an encapsulated core sheath morphology was only observed when the core solution had higher viscosity than the sheath. Position of BCP in the polymer precursor fibers dictated the porous morphology. The following morphologies were observed: 'BCP sheath' carbon fibers showed a side-by-side morphology with elongated pores confined to a side; 'BCP core' carbon fibers exhibited elongated pores only in the interior encapsulated by non-porous exterior carbon sheath; 'BCP both' carbon fibers displayed well distributed elongated pores both on the

interior and exterior; 'PAN both' carbon fibers were non-porous. All BCP-containing fibers produced porous carbon with an average mesopore size of ~23 nm when pyrolyzed at 800 °C without tension. Under tension, porous carbon fibers were successfully obtained only from 'BCP sheath' and 'BCP core'. 'BCP sheath' fibers showed the best mechanical properties with tensile strength of 1.1 GPa, tensile modulus of 190 GPa, and electrochemical capacitance of 11 F/g at 10 mV/s when pyrolyzed at 1315 °C under tension. Without tension and at a pyrolysis temperature of 800 °C, the fibers with BCP as both the sheath and core components achieved the highest electrochemical capacitance of 70 F/g at 10 mV/s and highest surface area of 264 m^2/g. among all gel-spun carbon fibers. Thus, carbon fibers pyrolyzed at higher temperature under tension rendered the best mechanical performance but reduced the electrochemical performance. Interaction parameter and characteristic correlation length of PMMA-*b*-PAN was calculated through thermodynamically governed computational method. The computationally calculated correlation length of PMMA-*b*-PAN provided an estimate of the pore sizes observed in the experimentally obtained carbon fibers. Pore size in the carbon fibers was found to be driven by processing parameters (type of spinning to get polymer precursor fibers, solvent evaporation effects, crosslinking of PAN during stabilization, thermal shrinkage during pyrolysis, *etc*.) in addition to the thermodynamic phase separation between PAN and PMMA-*b*-PAN blocks.

Chapter 5 showcased the processing parameters to blend low-asphaltenes with PAN through functionalization, gel-spin the blends and derive carbon fibers from them. Functionalization of asphaltenes using nitric acid (f-Asp) was confirmed through FTIR and the molecular weight of f-Asp characterized using MALDI. While, the as-received

Asp powder was not completely soluble in DMAc, f-Asp was found to be soluble in DMAc and formed relatively homogeneous spinning solutions with PAN. Precursor blend fibers with f-Asp/PAN blend ratios in the range of 30/70 to 60/40 were spun. Carbon fiber tensile strength and modulus from the f-asp/PAN blends were in the range of 0.5 to 1.1 GPa, and tensile modulus was in the range of 123 to 181 GPa. Carbon fibers with 30 wt% f-Asp and no significant porosity had better mechanical properties (tensile strength of 1.1 GPa and modulus of 181 GPa) compared to the ones with 60 wt% f-Asp. The study paved a pathway to derive carbon fibers from low-cost asphaltene precursors through potentially scalable route of solution/gel-spinning and further recommendations are elucidated in the following section.

6.2. Recommendations for future work

Porous carbon fibers are excellent candidates for realizing the concept of structural energy materials and bringing about light weighting in the electric and hybrid transportation, and renewable energy sectors. Further understanding of the porous morphology exhibited by blend or block copolymer systems including the change in pore size right from the solution stage till the carbonization, distribution of these pores, would help balance the electrochemical and mechanical performance of the resulting carbon fibers. Quantitative methods to predict the pore size in the carbon fibers using a combination of computational and experimental study of phase separation kinetics (type of spinning used to obtain the precursors, effect of drawing, stabilization reactions) and thermodynamics (phase diagram) should be pursued to help select the appropriate sacrificial polymer or block copolymer for blending with PAN. Modeling the effect of the

different porous shapes and their distribution on the fracture mechanics of porous carbon fibers could be done to optimize the factors influencing their mechanical properties.

To realize the concept of structural energy storage materials, structural battery or supercapacitor composites with the porous carbon fibers from gel-spun precursors need to be designed and characterized for both their mechanical and electrochemical efficiency. In terms of the mechanical performance of these structural energy storage composites with porous carbon fibers, it is imperative to study their multidirectional tensile, compressive and impact properties, so that it meets the standards of being used in automobiles. To balance the mechanical and electrochemical properties of porous carbon fibers from polymer precursors of PAN/sacrificial polymers or block copolymers, studies to optimize the temperature and tension applied during stabilization and carbonization are required. For such an optimization, the relationship among microstructure of porous carbon fibers, mechanical and electrochemical properties due to variation of temperature and tension, could be discerned through in-situ Raman and simultaneous mechanical and electrochemical (cyclic voltammetry, impedance spectroscopy) characterizations. Owing to the use of the porous carbon fibers in energy storage materials, electromechanical characterization to study the mechanical performance while the device is in use (charge/discharge cycle) should be conducted. One of the approaches to increase the electrochemical capacitance at higher carbonization temperature that also aids in better mechanical performance, could be to introduce heteroatoms like nitrogen that can increase the pseudo capacitance of these porous carbon fibers. Multifilament spinning, continuous stabilization and carbonization of gel-spun PAN/ sacrificial polymer block

copolymer precursors would need to be pursued for widespread use of the structural energy storage composites in automobiles.

Previous study by Zhou and Kumar have used fillers like SWNT in PAN-sacrificial polymer blends, to control the pore size of carbon fibers, that affects both the electrochemical and mechanical properties. Likewise, using fillers like CNT, graphene, carbon black, which have good electrical conductivity, in the PAN-sacrificial polymer blend or PAN/block copolymer systems could lead to improving mechanical and electrochemical performance that is desired for the energy storage composites. Alternatively, tailoring the surface of the porous carbon fibers with CNTs or graphene also presents a plausible pathway for designing cathodes and anodes for advanced energy storage composites. Surface area of these porous carbon fibers play a major role in enhancing the electrochemical performance. In Section 1.3.1, porous carbon materials with surface area as high as 2500 m^2/g were reported from highly ordered mesoporous silicon-based templates. Deriving porous carbon fibers from gel-spun precursors of PAN/sacrificial polymers or block copolymers along with mesoporous silicon templates, could increase the surface area and thus the resultant electrochemical performance of structural energy storage composites.

The method of functionalizing asphaltenes employed in the current study needs further optimization in terms of time, the type of functional groups added, molecular weight of functionalized asphaltenes, so that a pathway to scalable process for production of asphaltenes that are compatible with organic solvents (DMAc and DMF) commonly used for gel-spinning, is established. Improving the process parameters of f-Asp/PAN blends including the optimization of blend ratio, stabilization and carbonization

conditions, pre-treatment to enhance the purity of Asp, would help move closer to the objective of obtaining carbon fibers from low-cost precursors. In addition, blending asphaltene, a low-cost filler, with thermoplastic like PP could find applications in the concrete industry and more. Further study of carbon fibers derived from blends of asphaltene/PAN/sacrificial polymer or block copolymer would combine the two approaches used in this study and render structural energy storage materials with low-cost precursors for light weighting automobiles.

As described in section 1.2, reducing the cost of carbon fibers is one of the criteria set by DOE for their widespread use in automobiles. The cost of carbon fibers developed in the current study was not estimated and this is recommended for perusal in further studies. Other approaches for reducing carbon fiber costs include the following. (i) Using textile grade PAN with along with sacrificial blend or block copolymers in future studies could yield cost savings for obtaining porous carbon fibers. (ii) In addition to the cost of precursors, the conventional technique of thermal pyrolysis used in the current study contributes significantly to the carbon fiber cost. Use of techniques such as joule heating, microwave, plasma assisted processing for pyrolysis, could decrease the production cost of carbon fibers, and accelerate their widespread use in the automobile industry.[179,180]

APPENDIX A. SUPPLEMENTARY INFORMATION FOR CHAPTER 2

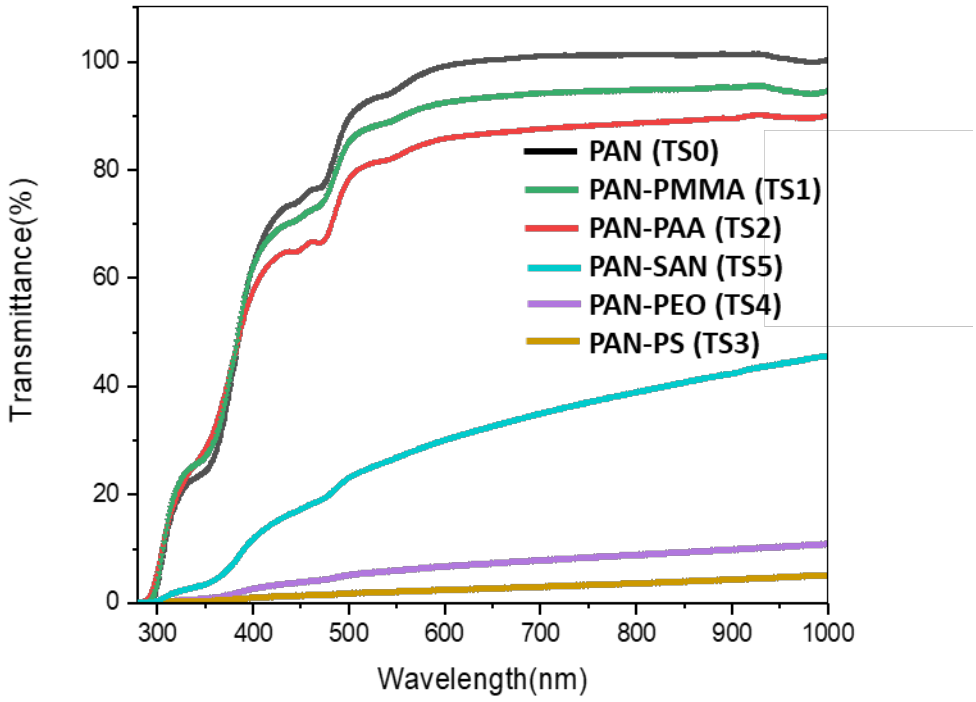

Figure A.1. UV-visible spectra of blend solutions of PAN with sacrificial polymers.

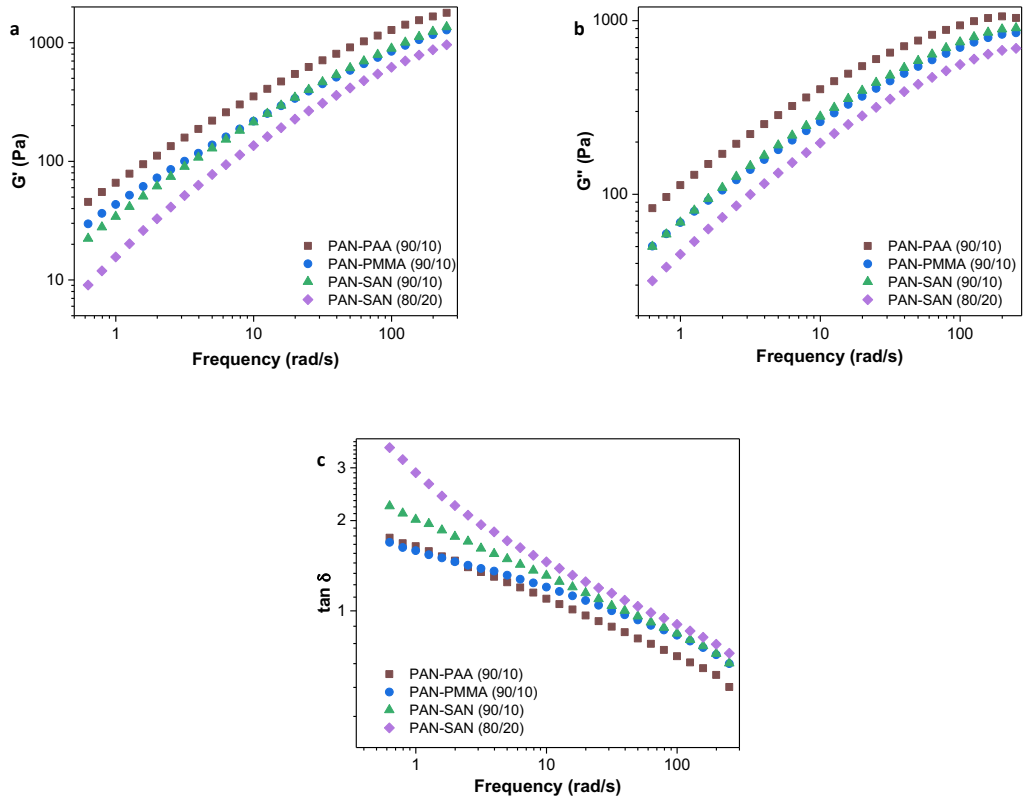

Figure A.2. Plots of a) storage modulus (G'), b) loss modulus (G''), and c) tan δ as a function of frequency for various spinning solutions.

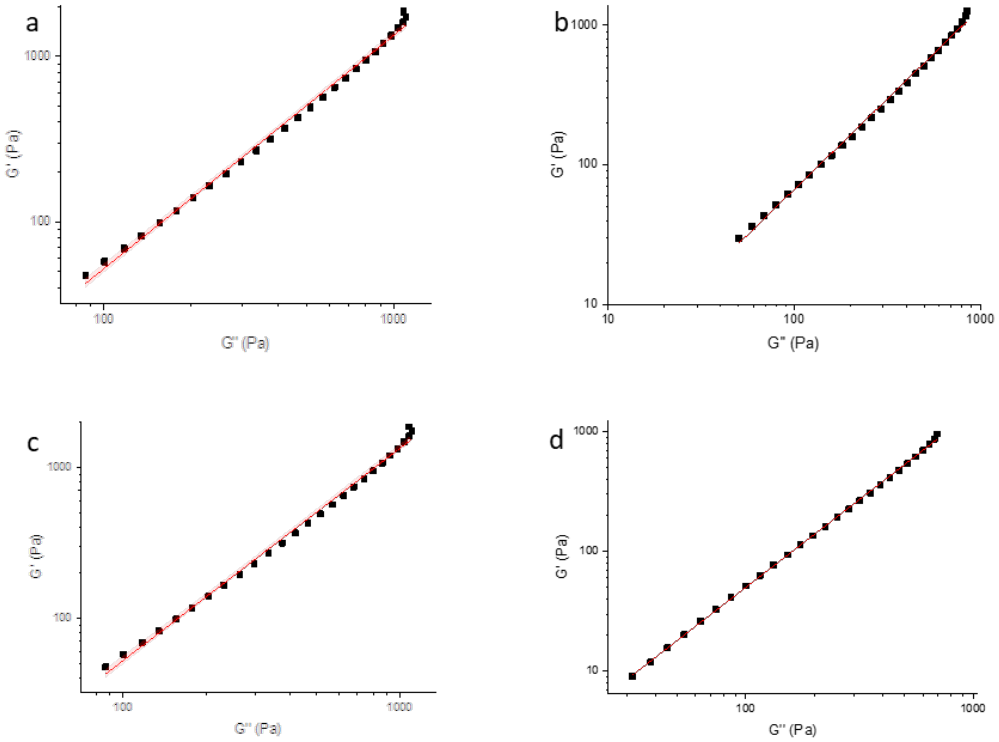

Figure A.3. Modified Cole-Cole plot of various spinning solutions: (a) PAN-PAA (90/10), (b) PMMA (90/10), (c) SAN (90/10) and (d) SAN (80/20).

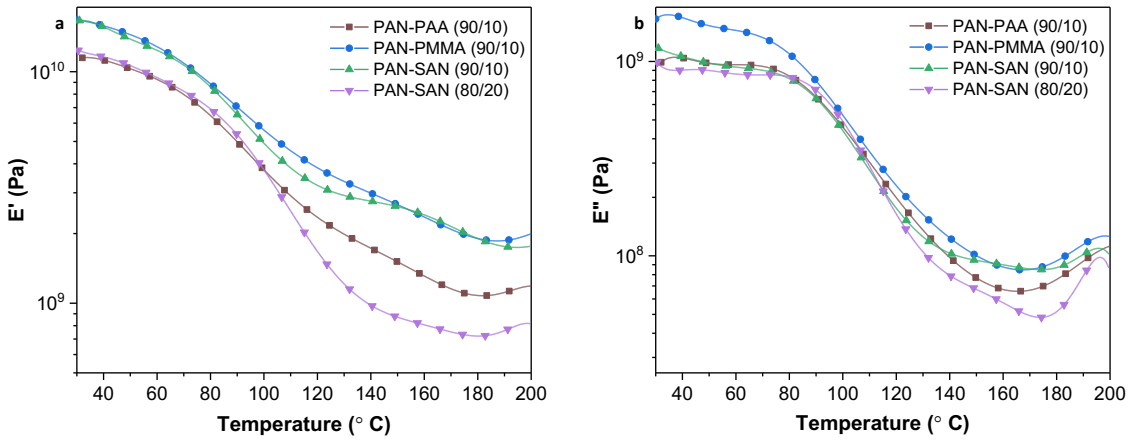

Figure A.4. Temperature sweeps of dynamic mechanical (a) storage modulus (E′), (b) loss modulus (E″), at a frequency of 0.1 Hz for the precursor blend fibers.

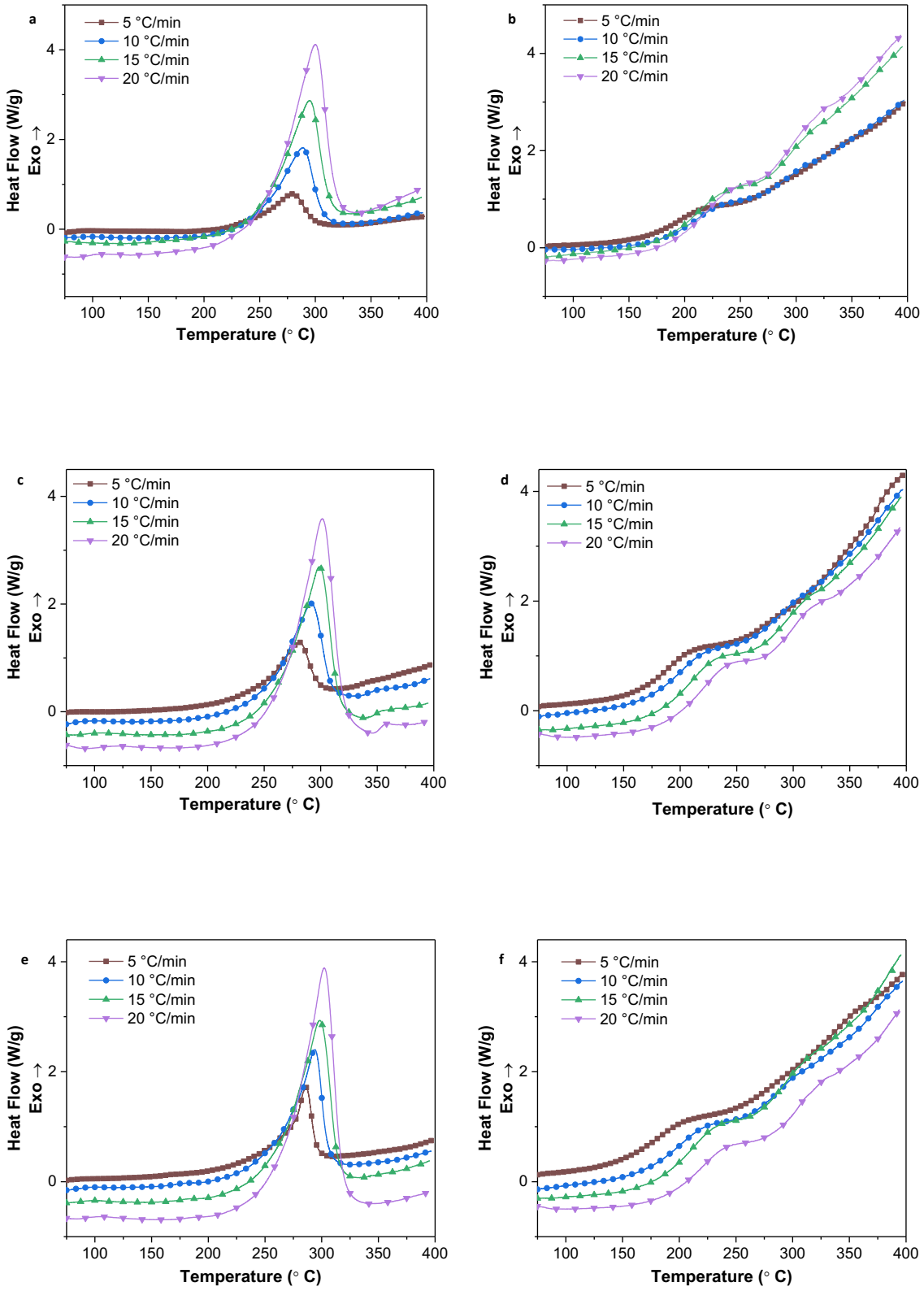
a
b
c
d
e
f
5 °C/min
10 °C/min
15 °C/min
20 °C/min
Heat Flow (W/g)
Exo →
Temperature (° C)

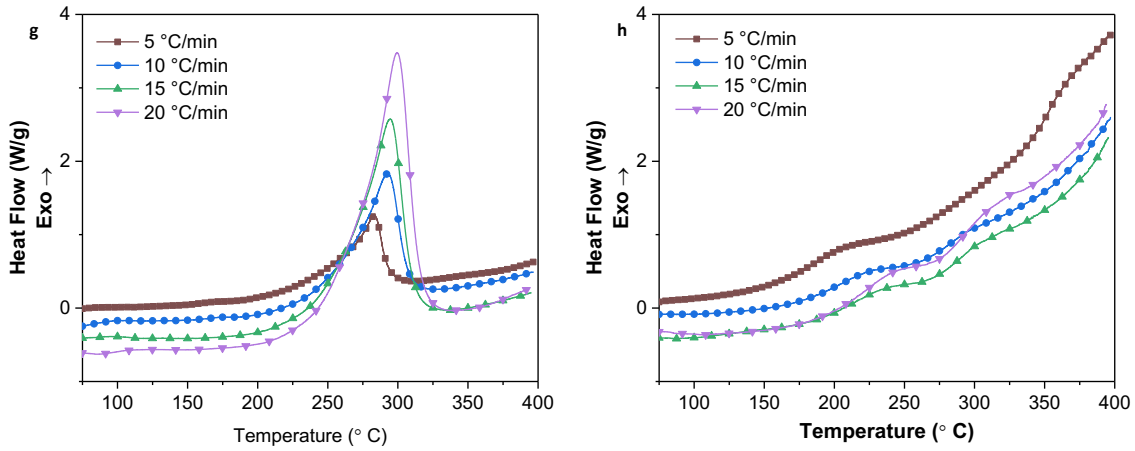

Figure A.5. DSC curves at various heating rates with (a) PAN-PAA (90/10), (c) PMMA (90/10), (e) PAN-SAN (90/10) and (g) PAN-SAN (80/20) fibers run in nitrogen; (b) PAN-PAA (90/10), (d) PAN-PMMA (90/10), (f) PAN-SAN (90/10) and (h) PAN-SAN (90/10) fibers rerun in air after runs in nitrogen.

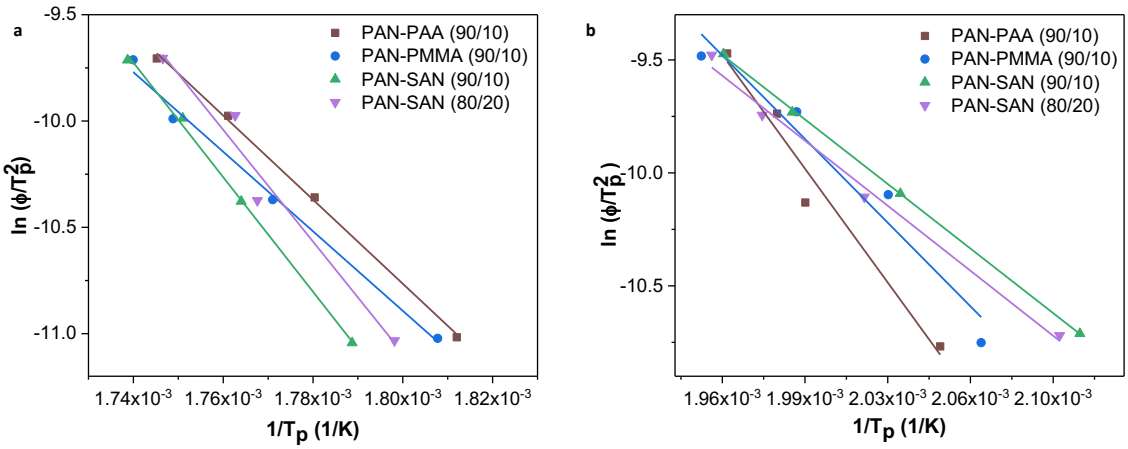

Figure A.6. Plots for calculating activation energies of (a) cyclization and (b) oxidation of the precursor blend fibers through Kissinger's method.

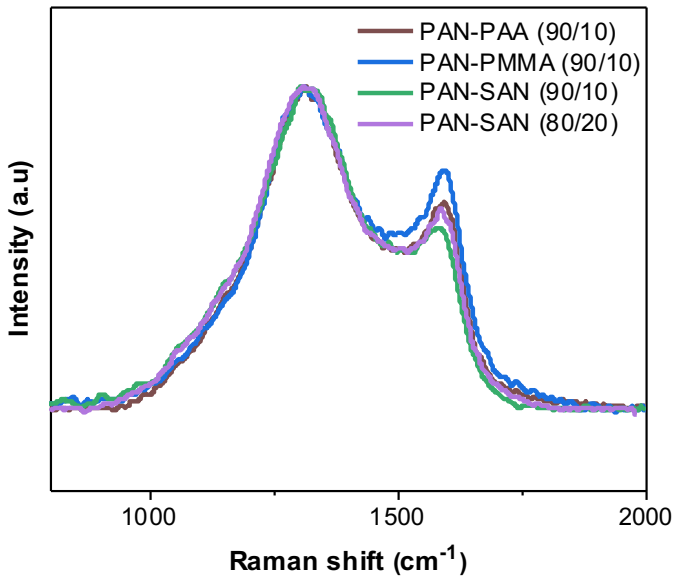

Figure A.7. Representative Raman spectra of carbon fibers from various precursor blends.

Table A.1. Spinning parameters for blends of PAN-co-MAA (Mol. wt: 500,000 g/mol) with PAA, PMMA and SAN.

	PAA	PMMA	SAN	SAN
Mol.wt (g/mol)	500,000	350,000	165,000	165,000
Solvent	DMAc	DMAc	DMAc	DMSO
Total solid content (g/dL)	11	11	11	11
Weight ratio of PAN: Sacrificial Component	90:10	90:10	90:10	80:20
Spinneret Temperature (°C)	80	80	70	70
Coagulation bath	Methanol at -50 °C	Methanol at -50 °C	Methanol at -50 °C	Methanol at RT
Hot drawing	Glycerol at 165 °C	Glycerol at 165 °C	Glycerol at 160 °C	Glycerol at 160 °C
As spun Draw Ratio (SDR)	1.5	1.5	3	3
Cold Draw Ratio (CDR)	1.5	1.5	1.5	1.3
Hot Draw Ratio (HDR)	4.5	6	3.8	4
Total Draw Ratio (TDR)*	10	13.5	17.1	15.6

*TDR = SDR x CDR x HDR

Table A.2. Details pertaining to polymer blend solutions prepared. *

Carbon Source	Sacrificial Polymer	Molecular Weight (g/mol)	Sample ID
PAN Mol.wt: 500,000 Sample ID: TS0	PMMA	350,000	TS1
	PAA	450,000	TS2
	PS	350,000	TS3
	PEO	200,000	TS4
	SAN	165,000	TS5

*PAN and the sacrificial polymer powder in the ratio of 80/20 were added to 20 ml of dimethylacetamide (DMAc) at room temperature. The slurry being continuously stirred was heated at 70 ºC for about 3.5 hours. The solid content of the solutions was 5 g/ 100 ml of DMAc. The solutions were characterized in the wavelength range of 300-1000 nm, with DMAc as the reference.

Table A.3. Activation energies and reaction kinetics parameters of precursor blend fibers.

	PAN-PAA (90/10)	PAN-PMMA (90/10)	PAN-SAN (90/10)	PAN-SAN (80/20)
Cyclization				
E_a (kJ/mol)[a]	164	156	224	218
A(s^{-1})[b]	1.2×10^{15}	1.5×10^{14}	3.7×10^{20}	1.4×10^{20}
$k_{250\ °C}$ (s^{-1})[c]	0.046	0.043	0.016	0.021
Oxidation				
E_a (kJ/mol)[a]	120	88	68	68
A(s^{-1})[b]	2.0×10^{12}	8.2×10^{8}	5.5×10^{6}	5.7×10^{6}
$k_{250\ °C}$ (s^{-1})[c]	2.203	1.349	0.924	0.852

[a] Activation energy obtained from Kissinger's plots (Figure A.3)
[b] Pre-exponential factor
[c] Reaction rate constant calculated at 250 °C

Table A.4. Solubility parameters of polymers used for calculating interaction parameters.

	PAN[a]	PAA[a]	PMMA[a]	SAN[b]	PS[a]
Solubility parameter (cal/ cm^{-3})$^{1/2}$	12.5	12	9.3	9.9	9.1

[a] Solubility parameter reported from [60]
[b] Calculated using the following: $\delta_{SAN} = 0.75\delta_{PS} + 0.25\ \delta_{PAN}$

Table A.6. Electrical conductivities of carbon fibers from various precursors, as listed.

	From PAN-PAA (90/10)	From PAN-PMMA (90/10)	From PAN-SAN (90/10)	From PAN-SAN (80/20)	IM7 [181]
Electrical conductivity (kS/m)	67 ± 35	74 ± 11	52 ± 5	40 ± 21	59.6

APPENDIX B. CALCULATION OF PORE FRACTION AND DENSITY OF CARBON FIBERS FROM PAN-SACRIFICIAL BLENDS

The following are the density values used in the calculation of the volume fraction: PAN -1.18 g/cm^3; PAA - 1.15 g/cm^3; PMMA - 1.18 g/cm$^{3;}$ SAN - 1.08 g/cm^3; carbon fiber IM7 (non-porous) - 1.78 g/cm^3 [182]. The density of the IM7 carbon fiber is used for further calculation of the porous carbon fibers produced in the study, and difference in the density due to variation in the processing conditions are discounted for simplifying the calculation. The conversion of PAN precursor to carbon fibers leads to reduction in volume, as calculated from the densities:

$$\text{Volume reduction} = ((1.78 - 1.18)/\ 1.18) = 0.51$$

We assume that the SAN domains do not undergo any change in volume fraction during the process of conversion from precursor to carbon fibers, as they are completely burnt away giving rise to pores. Using the value of volume fraction reduction for PAN, the volume fraction of pores due to burning-off of sacrificial polymer, is estimated using the rule of mixtures, and the values are reported in Table B1.

Table B.1. Calculation of volume fraction of pores in carbon fibers from polymer blends.

	Precursor	Carbon Fiber	
	Volume (ml)[a]	Volume (ml)[b]	Volume fraction (%)[c]
PAN-PAA (90/10)			
PAA (pores)	8.7	8.7	18
PAN (solid)	76.3	40.4	82
PAN-PMMA (90/10)			
PMMA (pores)	8.5	8.3	18
PAN (solid)	76.3	40.4	82
PAN- SAN (90/10)			
SAN (pores)	9.3	9.3	19
PAN (solid)	76.3	40.4	81
PAN-SAN (80/20)			
SAN (pores)	18.5	18.5	35
PAN (solid)	67.8	35.9	65
PAN-SAN (95/5)			
SAN (pores)	4.8	4.8	11
PAN (solid)	80.5	41.1	89

[a]Voulme calculated using the density and weight of the corresponding component in the blend
[b]Volume of sacrificial polymer is assumed constant while the volume reduction factor of 0.53 is used to calculate the volume of non-porous/solid part of carbon fibers from PAN
[c]Volume fraction of pores/solid = (Volume of pores/solid) / (Volume of pores + Volume of solid)

Further, the density of the porous carbon fibers is estimated as follows, based on the assumption that the volume of sacrificial polymer (pores) remains constant as the precursors are stabilized and carbonized:

$$\text{Density of porous carbon fiber} = 1.78\ g/cm^3 * \text{Volume fraction of the solid}$$

The lower bound of the densities of carbon fibers from the blend precursors are listed in Table B.2.

Table B.2. Calculated densities of carbon fibers from polymer blend precursors.

	From PAN-PAA (90/10)	From PAN-PMMA (90/10)	From PAN-SAN (90/10)	From PAN-SAN (80/20)	From PAN-SAN (95/5)
Density (g/cm^3)	1.46	1.46	1.44	1.16	1.59

APPENDIX C.SUPPLEMENTARY INFORMATION FOR CHAPTER 3

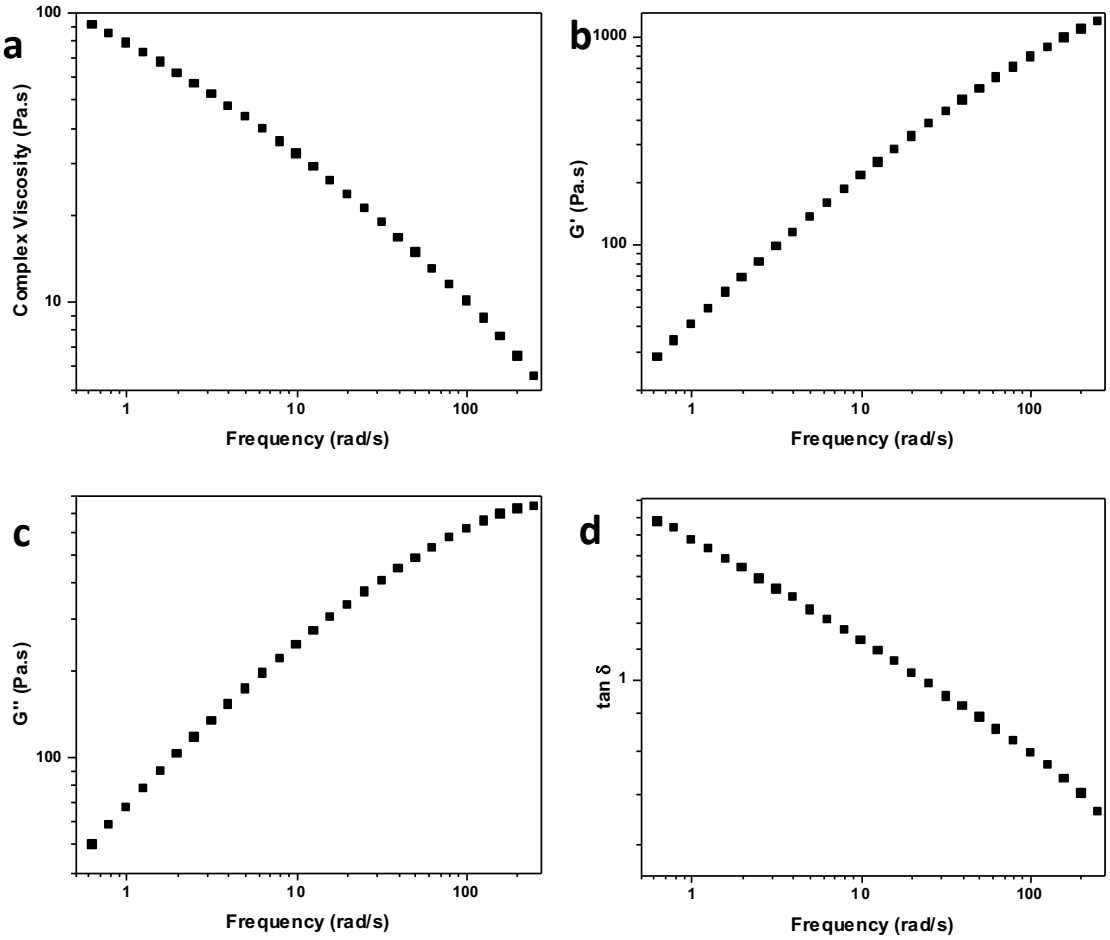

Figure C.1. Rheology of PAN-SAN (95/5) blend spinning solution. Plots of (a) Complex viscosity, (b) Storage modulus (G') and (c) Loss modulus (G'') as a function of angular frequency.

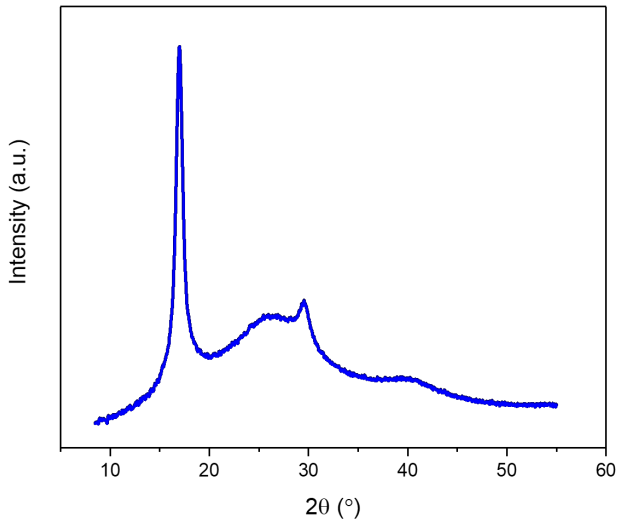

Figure C.2. WAXD plot of PAN-SAN (95/5) precursor blend fiber.

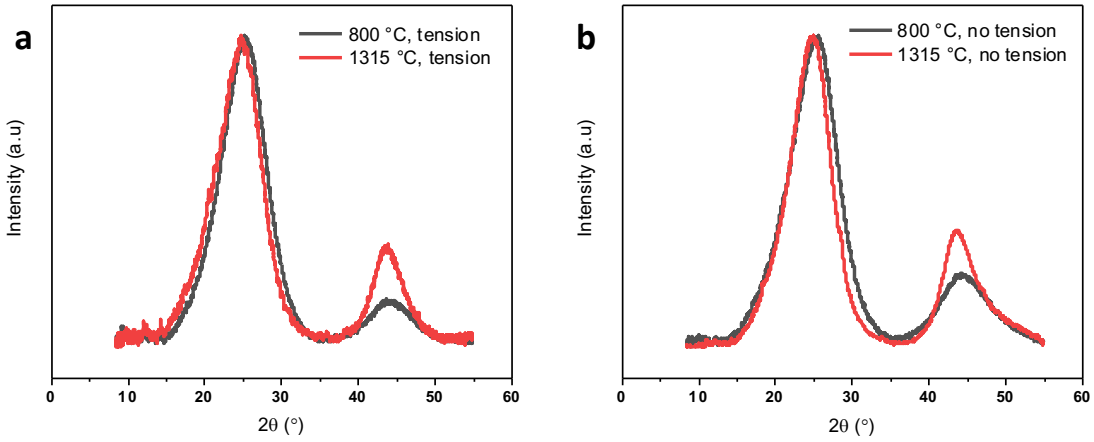

Figure C.3. WAXD plots of PAN-SAN derived porous carbon fibers. (a) With tension and (b) without tension at different temperatures of carbonization.

APPENDIX D.SUPPLEMENTARY INFORMATION FOR CHAPTER 4

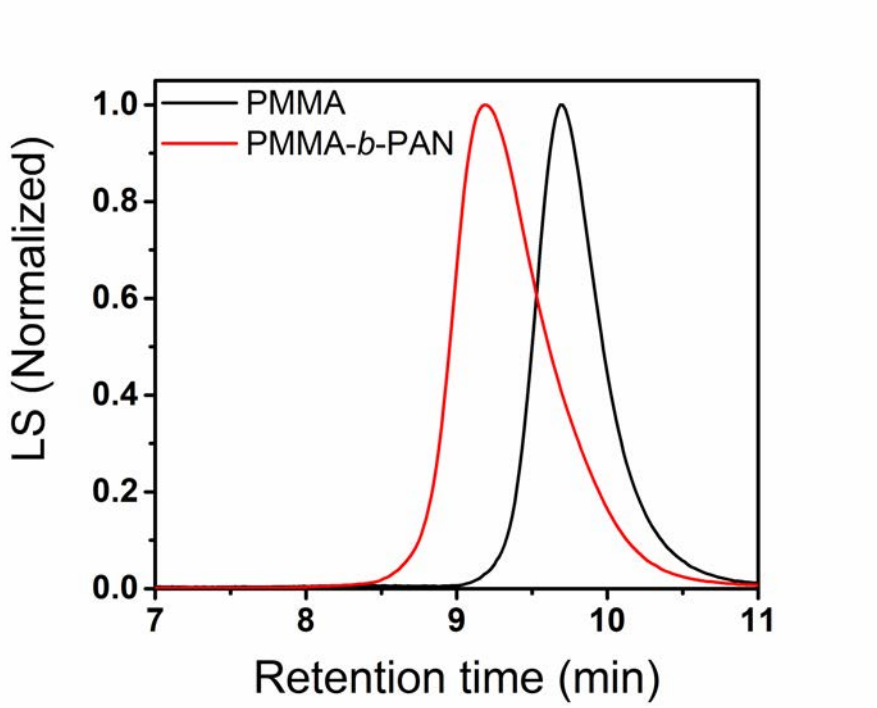

Figure D.1. Size exclusion chromatogram (SEC) normalized traces of poly(methyl methacrylate) (PMMA) and block copolymer (BCP) poly(methyl methacrylate)-*block*-poly(acrylonitrile) (PMMA-*b*-PAN) using a light scattering (LS) detector.

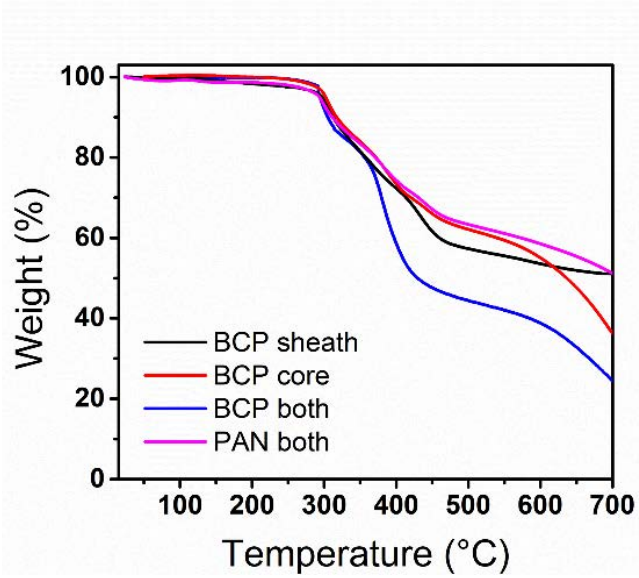

Figure D.2. Thermal gravimetric analysis traces of polymer precursor fibers in various spinning configurations.

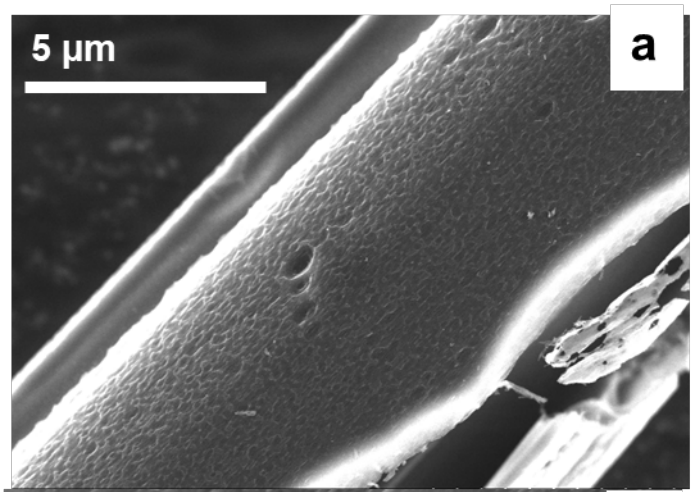

Figure D.3. Additional SEM image of carbon fiber-surface from 'BCP sheath' polymer fibers after pyrolysis under tension at 800 °C.

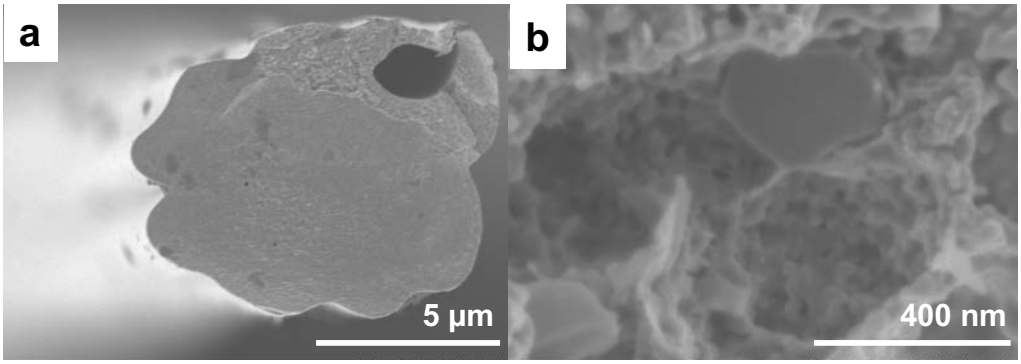

Figure D.4. Additional cross-sectional SEM images of carbon fibers from ‘BCP sheath’ polymer fibers after pyrolysis under tension at 1315°C.

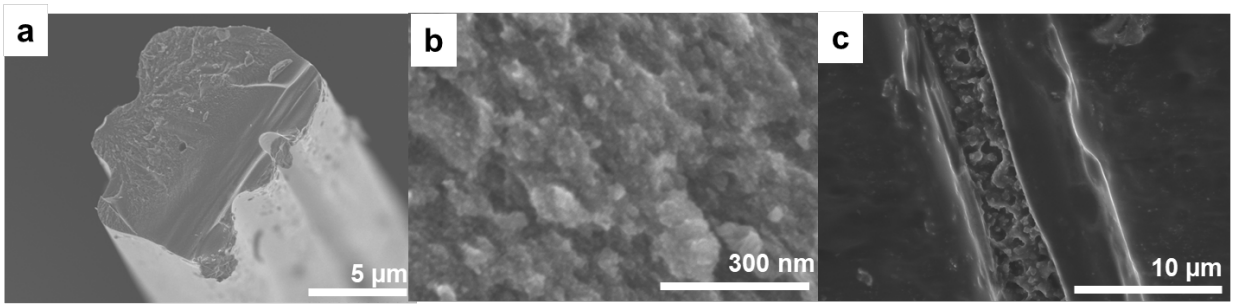

Figure D.5. Additional SEM images of carbon fibers from ‘BCP core’ polymer fibers after pyrolysis under tension at 800 °C. Panels a and b are cross-sections. Panel c is the fiber-surface.

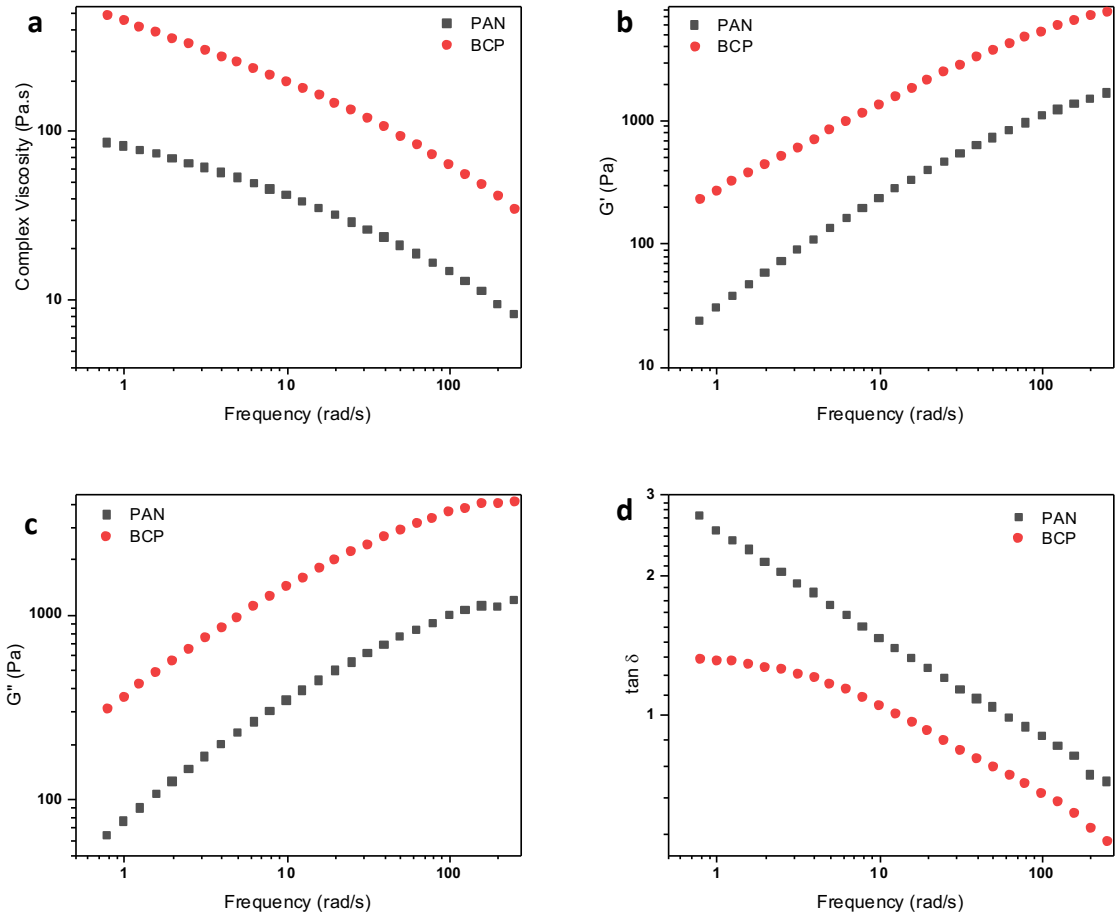

Figure D.6. Frequency-sweep (a) complex viscosity, (b) storage modulus (G'), (c) loss modulus (G") and (d) tan δ showing the rheological behaviors of spinning solutions of PAN (11.5 g dL^{-1}) and BCP (20 g dL^{-1}) in DMF.

D.1. Peak fitting for precursors fibers

MDI Jade 9 software was used to fit the crystalline and amorphous peaks in the wide-angle X-ray diffraction (WAXD) patterns of the polymer precursors: 'BCP sheath', 'BCP core', 'BCP both' and 'PAN both'. Figure S8 shows the deconvoluted peaks labelled 'amorphous' and 'crystalline'. The total crystallinity in each case was calculated by including the contribution from all the crystalline peaks of PAN and excluding all the amorphous peaks from both PAN and BCP.

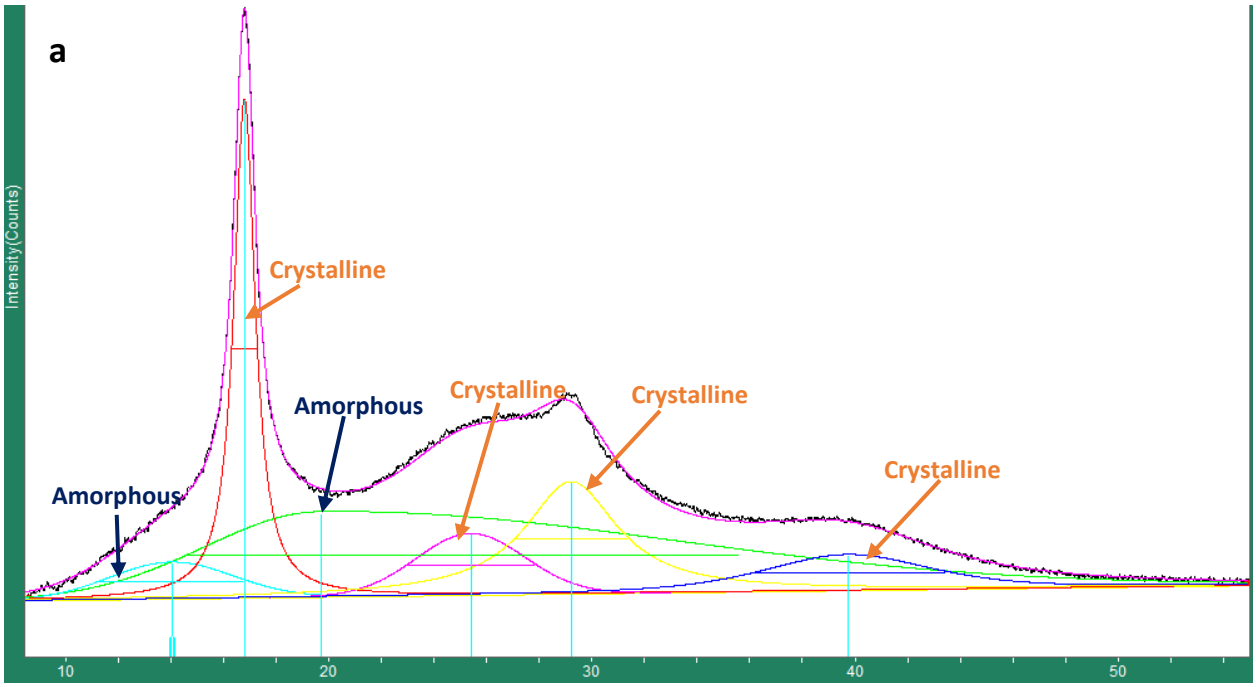
a
Intensity(Counts)
Crystalline
Amorphous
Crystalline
Crystalline
Amorphous
Crystalline
10
20
30
40
50

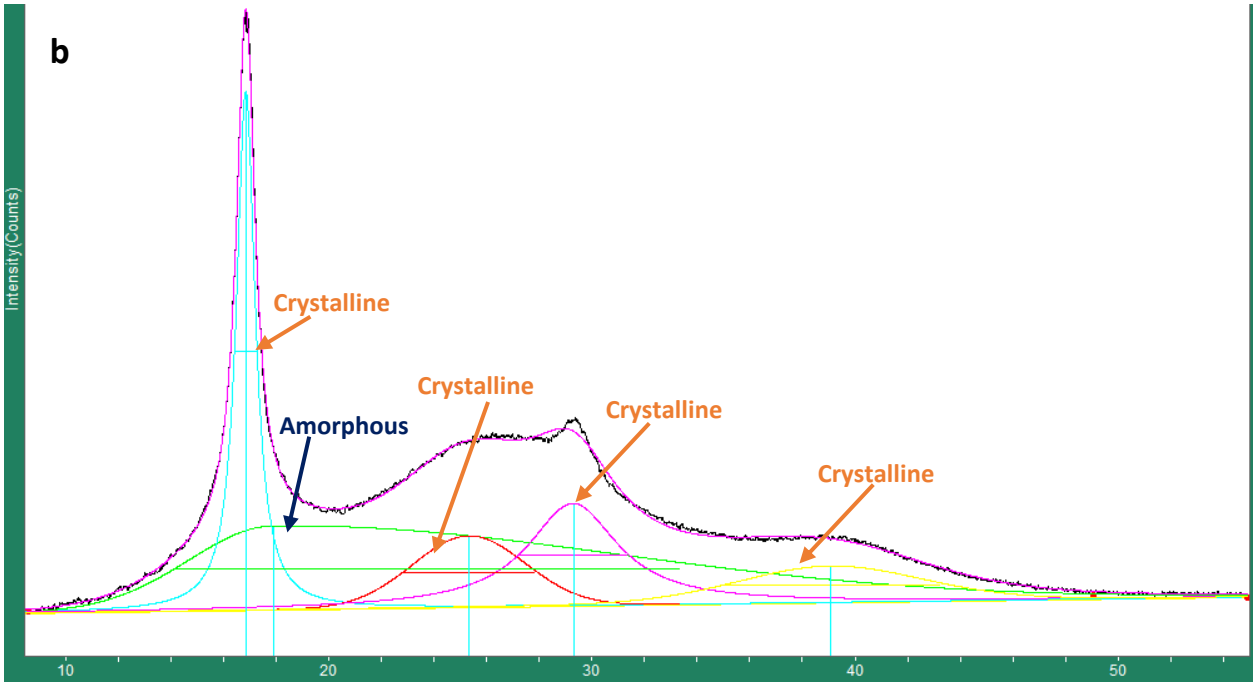
b
Intensity(Counts)
Crystalline
Crystalline
Crystalline
Amorphous
Crystalline
10
20
30
40
50

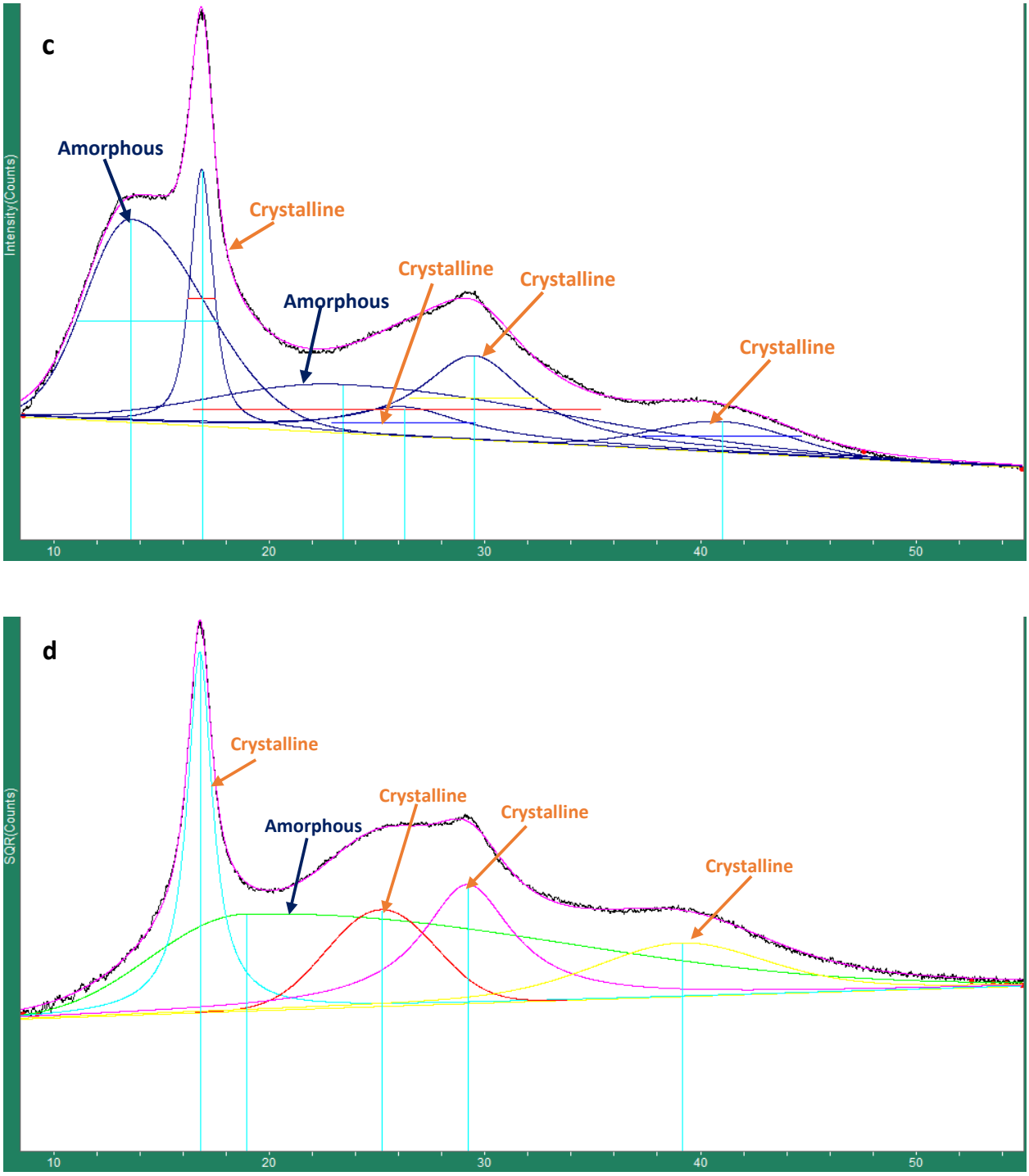

Figure D.7. Fitting of integrated WAXD graphs of polymer fibers: (a) 'BCP sheath', (b) 'BCP core', (c) 'BCP both' and (d) 'PAN both'. (X-Axis: 2θ (°); Y-axis: Intensity (counts))

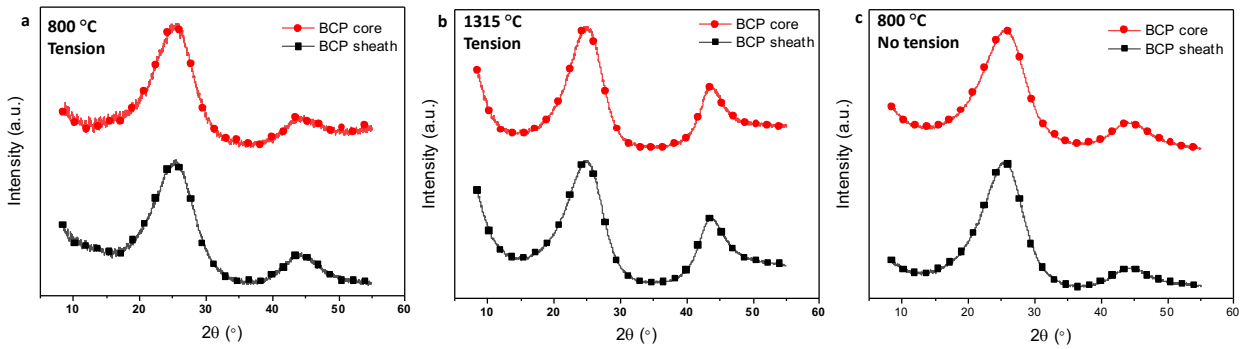

Figure D.8. WAXD graphs of porous carbon fibers after pyrolysis of the bicomponent polymer fibers (a) 800 °C Tension, (b) 1315 °C Tension and (c) 800 °C No tension.

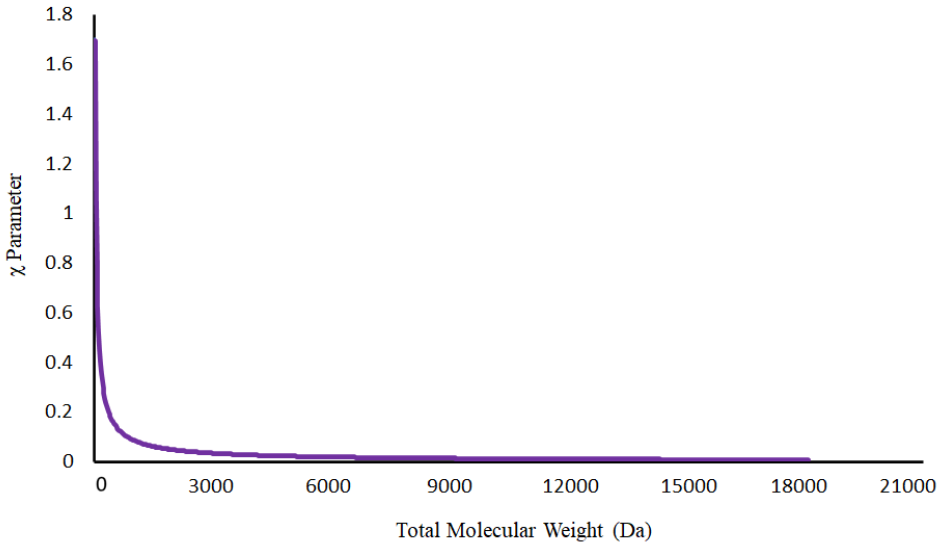

Figure D.9. Extrapolated χ parameter calculation for PMMA-*b*-PAN.

Table D.1. Average pore size of carbon fibers and films derived from BCP (M_n ~160, 000 g/mol).

Configuration	Conditions	Average pore size (calculation method)
	Gel-spinning	
BCP both	800 °C, no tension	21 nm (SEM- Image analysis) 23 nm (BET)
BCP core	800 °C, no tension	30 nm (SEM- Image analysis)
BCP sheath	800 °C, no tension 800 °C, tension 1315 °C, tension	27 nm (SEM- Image analysis) 13 nm (SEM- Image analysis) 19 nm (SEM- Image analysis)
	Electrospinning	
BCP fibers [55]	800 °C, no tension	10.6 nm (TEM) 10.1 nm (SEM- Image analysis) 10 nm (BET)
	Films	
BCP films [63]	800 °C, no tension	40 – 50 nm (AFM- Image analysis)

D.2. Computational study calculations

D.2.1. Calculation of the interaction parameter

Energy of mixing, ΔE_{ij} is defined as:

$$\Delta E_{ij} = \frac{1}{2} V_{ref} \left[(Z_{ij} + Z_{ji}) \frac{IE_{ij}}{nV_{ij}} - (Z_{ii} \frac{IE_{ii}}{nV_{ii}} + Z_{jj} \frac{IE_{jj}}{nV_{jj}}) \right]$$

Here n, Z_{ij}, V_{ij}, V_{ref}, and IE_{ij} refer to the degree of polymerization, coordination number of the species j around the species i, the volume enclosed by the Connolly surface over the combined pair of molecules i and j, reference volume, and interaction energy between individual molecules of species i and j, respectively. The geometry optimizations and the Mulliken charge calculations of PMMA and PAN polymers reported herein were

performed on the basis of spin polarized density functional theory (DFT) within B3LYP functional, as implemented in the Jaguar with 6-31G+(d,p) basis set. Subsequently, the Connolly volume, reference volume, the interaction energy of PMMA and PAN, and the coordination number of PMMA around PAN were obtained to calculate the energy of mixing ΔE_{ij} of BCP *via* Forcite and blends module calculations in Materials Studio simulation package.

D.2.2. Dissipative particle dynamics (DPD)

For a DPD simulation, the bead spring model, where one bead represents a group of multiple atoms, was employed, and the motions of beads are described by integrating Newton's equations of motion as follows:

$$\frac{dr_i}{dt}_i = v_i \text{ and } m_i \frac{dv_i}{dt}_i = f_i$$

where r_i, v_i, and m_i denote the position, velocity, and mass of the *i*-th particle, respectively, and f_i denotes the force acting on the *i*th particle. The force acting on a bead contains three parts:

$$f_i = \sum_{j \neq i} (F_{ij}^C + F_{ij}^D + F_{ij}^R)$$

where F_{ij}^C, F_{ij}^D, and F_{ij}^R denotes conservative repulsive, dissipative, and random force dependent on the position and velocity of the *i*-th particle, respectively. Each force is expressed as follows:

$$F_{ij}^{C} = \begin{cases} a_{ij}\left(1 - \frac{r_{ij}}{r_c}\right)\hat{r}_{ij} & (r_{ij} < r_c) \\ 0 & (r_{ij} \geq r_c) \end{cases}$$

$$F_{ij}^{D} = -\gamma\omega^{D}(r_{ij})\left(\hat{r}_{ij} \cdot \vec{v}_{ij}\right)\hat{r}_{ij}$$

$$F_{ij}^{R} = -\sigma\omega^{R}(r_{ij})\,\theta_{ij}\,\hat{r}_{ij}$$

where a_{ij} and r_{ij} are the maximum repulsion force and the distance between bead *i* and *j*, respectively. γ and ω are the friction coefficient and the noise amplitude, respectively, and ω^{D} and ω^{R} are weight functions. θ_{ij} denotes the white-noise term that randomly fluctuates with Gaussian statistics, with $\langle\theta_{ij}\rangle = 0$ and $\langle\theta_{ij}\rangle = 1$.

The simulation box size was specified as 30 × 30 × 30 with a grid spacing of 1.0 and a bead density of 3.0, enabling the use of the linear relationship between the DPD repulsion parameter $a_{i,j}$ for species *i* and *j* and the corresponding Flory–Huggins $\chi_{i,j}$-parameter, as derived by Groot and Warren. Here, we obtained $\chi_{i,j}$ value for PMMA-*b*-PAN by extrapolating the abovementioned $\chi_{i,j}$ results to the molecular weight used in the experiments. For better computational efficiency, we scaled the di-block copolymer (BCP) down to 1:100, meaning a single linear polymer chain contained 6 PMMA and 18 PAN beads, and a total of 84000 beads were randomly dispersed in the simulation box.

APPENDIX E. SUPPLEMENTARY INFORMATION FOR CHAPTER 5

E.1. Methanol functionalization of asphaltenes

Figure E.1 shows the reaction mechanism of transesterification process that is predicted to occur when nitric acid functionalized asphaltene is further functionalized in methanol in the presence of an acid catalyst. Previous literature used supercritical methanol (at 250 °C) to perform esterification on naphthenic acids in raw crude oil.[183] However, high temperature was likely not required here, as the f-asp was already oxidized. 10 g of washed and dried asphaltene from the 1h nitric acid functionalization (f-Asp) was added to a 1 L round bottom flask along with 500 mL of methanol and 2 mL of nitric acid. A stirrer was added to the flask before setting up a reflux using a condenser and circulating water. The round bottom flask contents were refluxed at 60°C for 24 hours. After functionalization, the contents were filtered and washed with DIW until a neutral pH of 7 was reached. The methanol functionalized asphaltenes were labelled as f1-Asp.

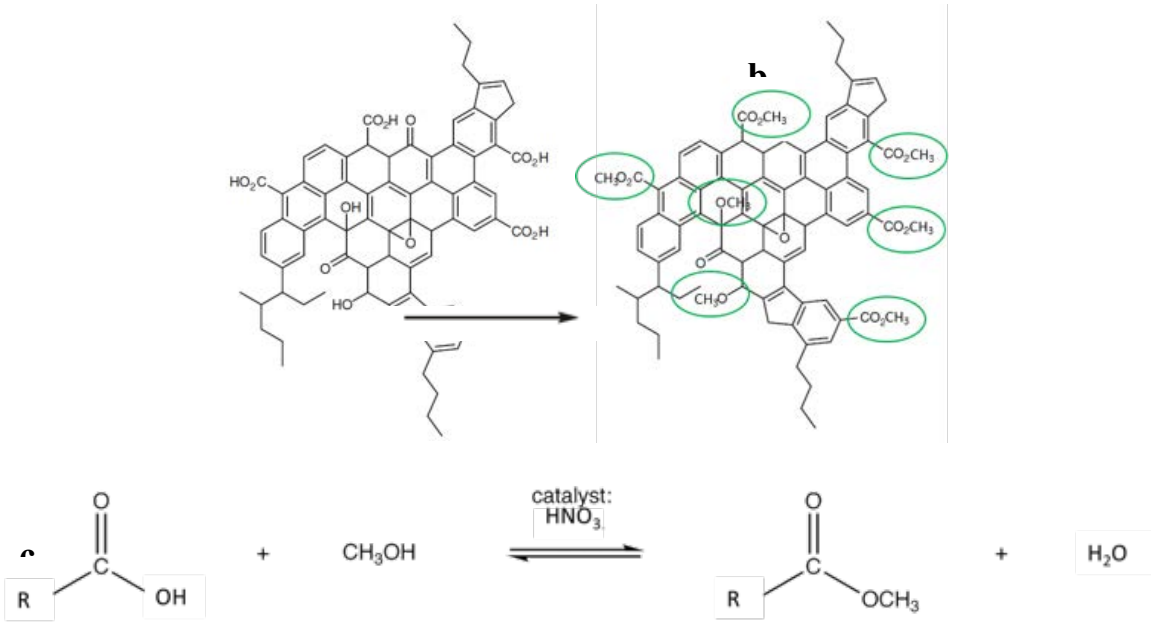

Figure E.1. (a) Structure of oxidized asphaltene[1] after nitric acid functionalization. (b) Structure of methanol functionalized asphaltene (c) Predicted reaction mechanism for transesterification of oxidized asphaltene in the presence of nitric acid.

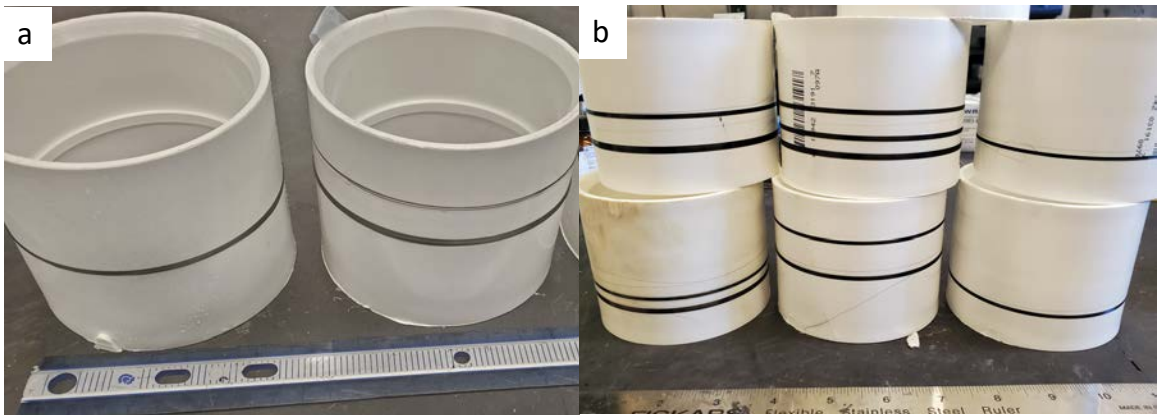

Figure E.2. Representative drawn precursor fibers: (a) Fiber A-P, (b) Fiber C-P.

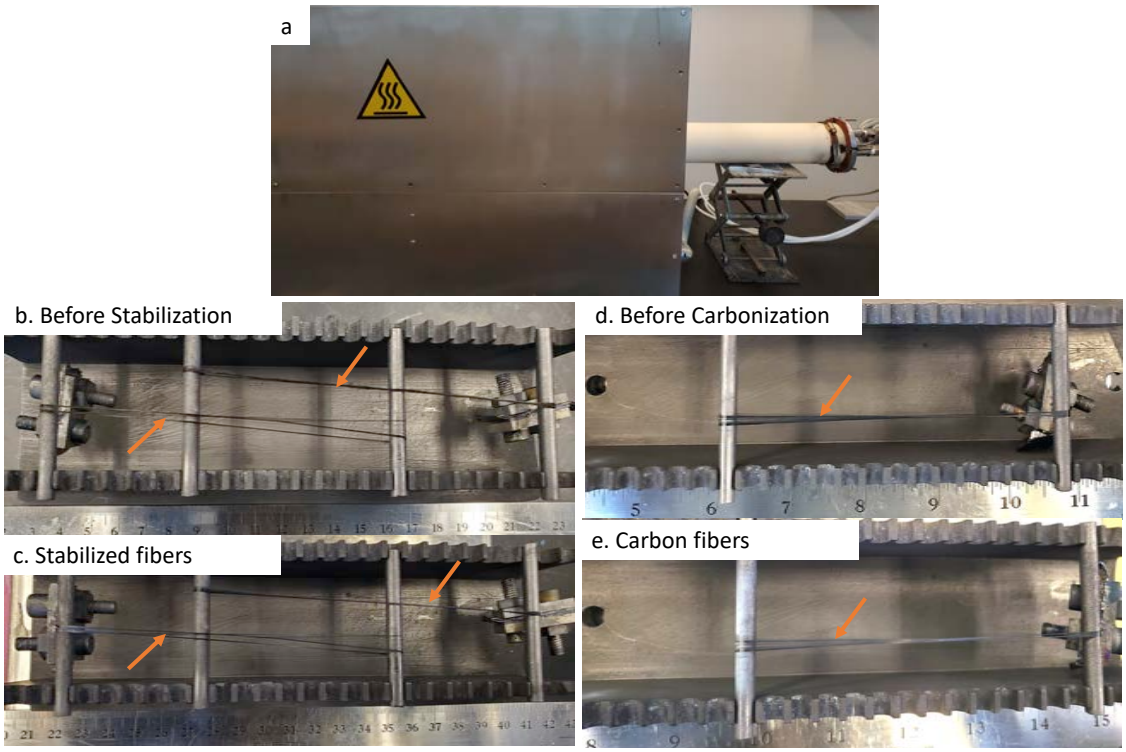

Figure E.3. (a) Tube furnace used for stabilization and carbonization. (b) experimental setup for stabilizing the drawn precursor fibers. (c) stabilized fiber. (d) experimental setup for carbonizing the stabilized fibers. (e) resulting carbon fiber. Arrows indicate the fibers in each case (b-e).

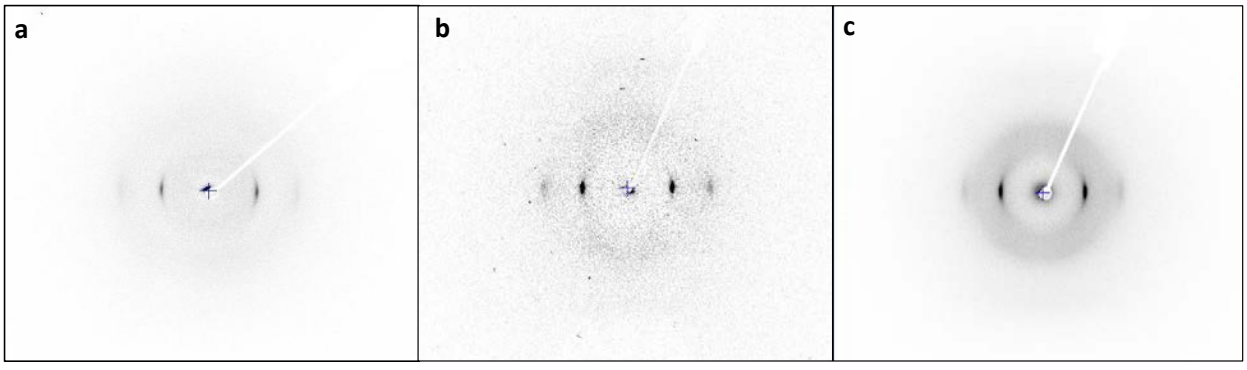

Figure E.4. 2D WAXD patterns of precursor f-Asp/PAN drawn fibers. (a) A-P, (b) B-P and (c) C-P.

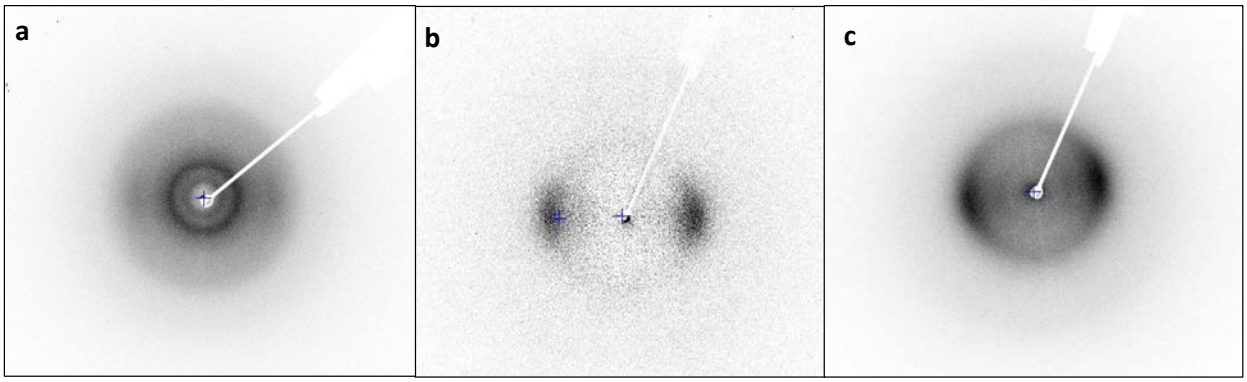

Figure E.5. 2D WAXD patterns of stabilized fibers. (a) A-S, (b) B-S, and (c) C-S.

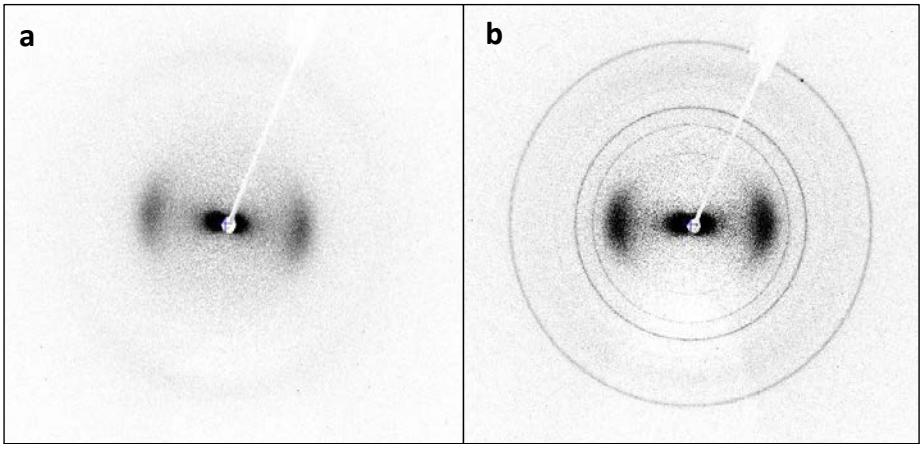

Figure E.6. 2D WAXD patterns of carbon fibers B-C. WAXD (a) and (b) patterns were obtained from different spots on the same sample bundle and indicate that the presence of inorganic impurities was not present everywhere in the fiber.

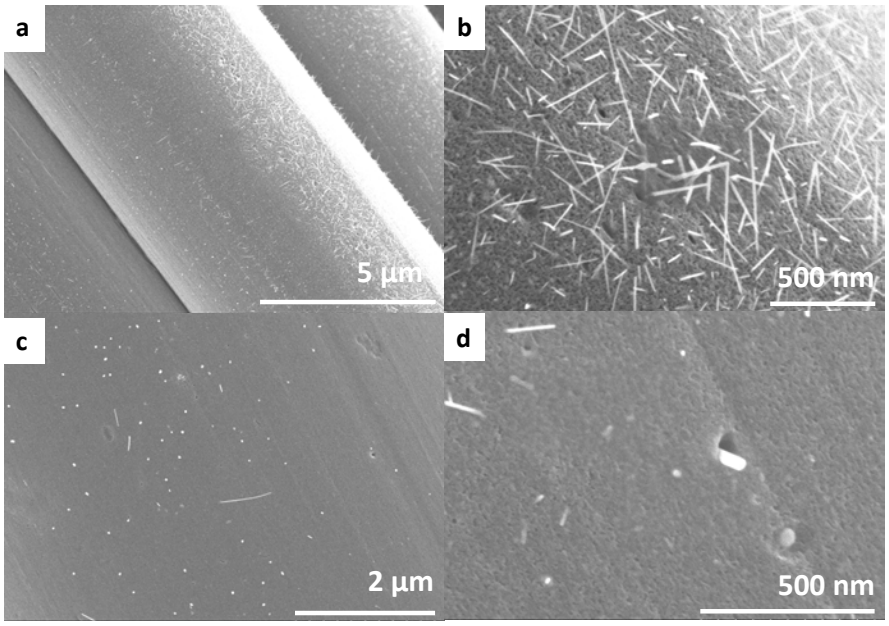

Figure E.7. SEM images of the surface of B-C carbon fibers.

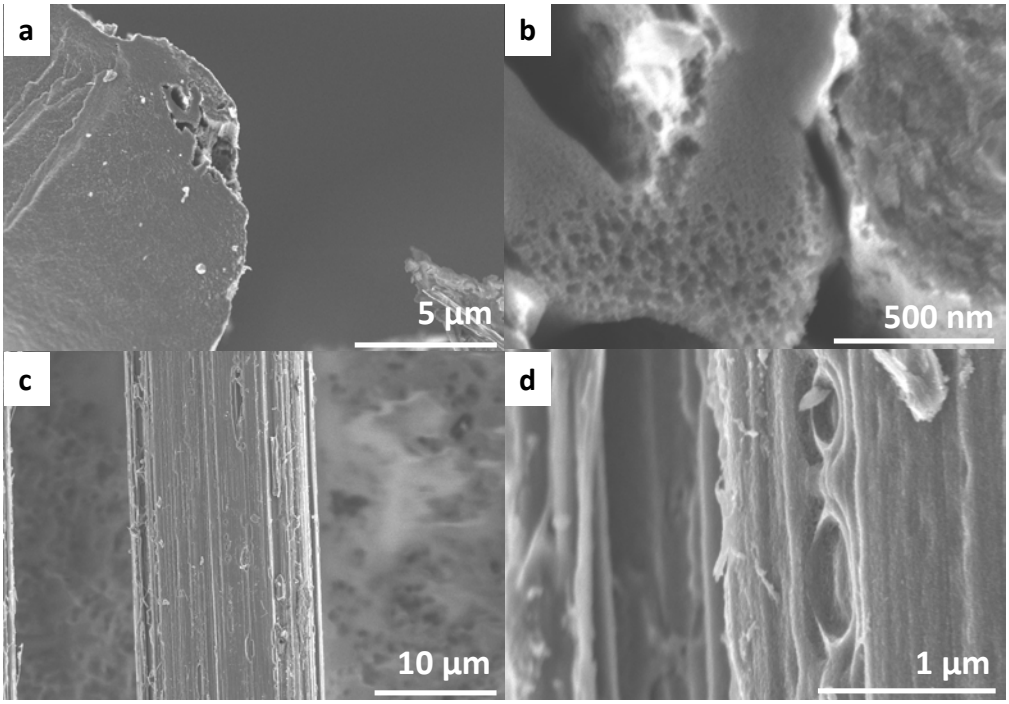

Figure E.8. SEM images of the cross-sections (a-b) and surface (c-d) of C-C carbon fibers.

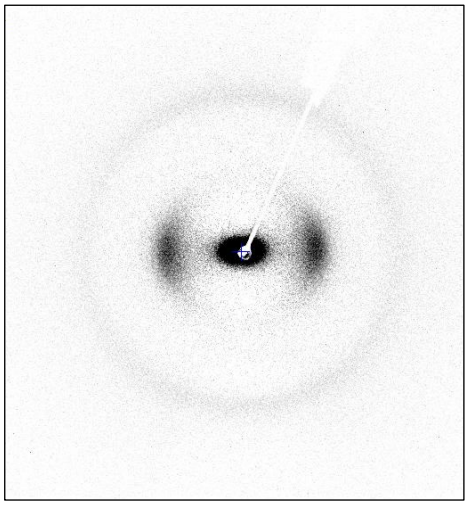

Figure E.9. 2D WAXD patterns of C-C carbon fibers.

Table E.1. Stabilization and carbonization protocols for f-Asp/PAN blends.

Trial A f-Asp/PAN (43/57)	**Trial B** f-Asp/PAN (30/70)	**Trial C** f-Asp/PAN (60/40)
A-S	**B-S**	**C-S**
3 °C /min from RT to 265 °C & hold for 270 min. 3 °C /min to 305 °C & hold for 30 min.	3 °C /min from RT to 265 °C & hold for 150 min. 3 °C /min to 350 °C & hold for 60 min.	3 °C /min from RT to 265 °C & hold for 150 min. 3 °C /min to 350 °C & hold for 60 min.
10	7.5-15	5
Fibers were not broken. No change in length	Fibers were broken. No change in length.	Fibers were not broken. ~11% shrinkage.
A-C	**B-C**	**C-C**
5 °C /min from RT to 1315 °C & hold for 10 min.	5 °C /min from RT to 1315 °C & hold for 10 min.	5 °C /min from RT to 1315 °C & hold for 10 min.
10	No tension	5
Fibers were broken and crimped.	Fibers were not crimped.	Fibers were not broken or crimped.

APPENDIX F. SPINNING OF ASPHALTENE-POLYPROPYLENE BLENDS

Fibers from blend of Asp and PP (SABIC PP FPH50) were obtained through melt compounding and extrusion. All the Asp-PP blend fiber extrusions were done using a micro-compounder (DSM Xplore 15 cc). Asp and PP powders in the designated weight ratios were mixed and used as a feed for the compounding. A spinneret of 500 μm diameter was used to extrude the filament into air and the filaments were attempted to be collected on plastic spools. Figure F.1 shows representative fibers collected on plastic spools. Table F.1 summarizes the samples collected, the temperature used for melt compounding and the collection speed of fibers. The collection speed decreased with increasing asphaltene content.

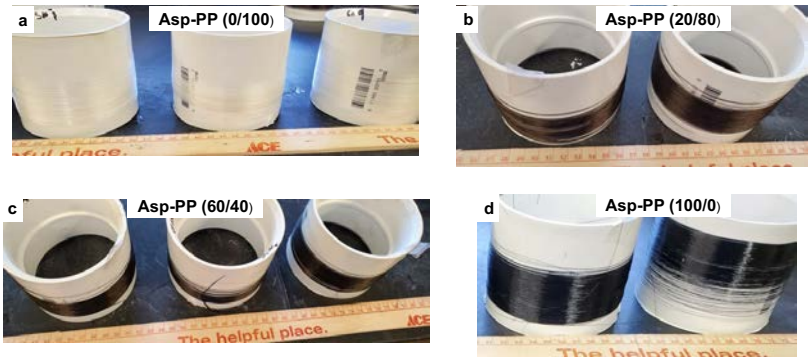

Figure F.1. Representative as-spun fibers: (a) Asp-PP (0/100), (b) Asp-PP (20/80), (c) Asp-PP (60/40) and (d) Asp-PP (100/0).

Table F.1. Summary of the Asp/PP blend fibers collected and the associated parameters.

Asp-PP (wt%/wt%)	Sample Name	Processing Temperature (°C)	Collection Speed (m/min)
Asp-PP (0/100)	T5A1	220	35-78
	T5A2-T5A3		78
Asp-PP (20/80)	T5B1	240	30-83
	T5B2		80
Asp-PP (40/60)	T5C1	240	20-67
	T5C2		56
Asp-PP (60/40)	T5D1	240	20-70
	T5D2		30-70
	T5D3		55
Asp-PP (80/20)	T5E1	240	30-67
	T5E2		55
	T5E3		40
	T5E4		29 (stable)
Asp-PP (100/0)	T5F1-T5F2	240	20-22
	T5F3-T5F4		14.7 (stable)

As-spun fibers of Asp-PP (20/80) and Asp-PP (60/40) were further drawn through a glycerol bath maintained at 130-135 °C (Drawn fibers shown in Figure F.2). Hot draw ratio for both the fibers was 2. Asp-PP (100/0), without the PP, could not be hot drawn at this temperature. Table F.2 lists the mechanical properties of the Asp-PP (20/80), Asp-PP (60/40) and Asp-PP (100/0) fibers. Fibers of Asp-PP (20/80) and Asp-PP (60/40) showed significantly large variation in diameter. Mechanical properties decreased with the increasing asphaltene content. Asp-PP (20/80) fibers produced in this study showed tensile modulus higher than control PP fibers (4.6 GPa) reported previously.[184] Thus,

asphaltene could be potentially serve as a low-cost filler in PP fiber for certain applications.

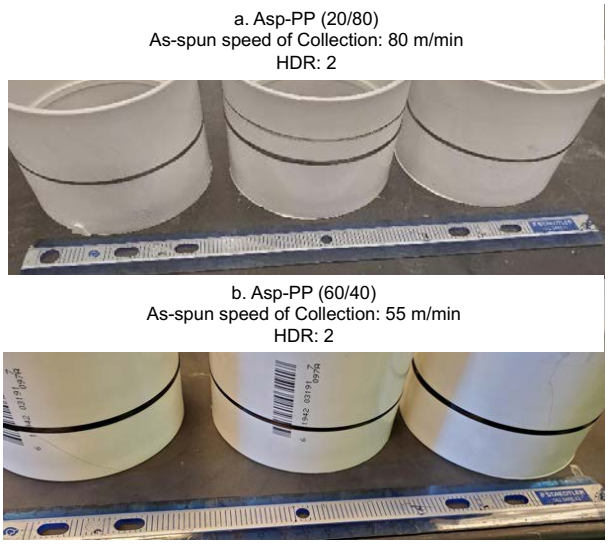

Figure F.2. Representative drawn precursor fibers: (a) Asp-PP (20/80), and (b) Asp-PP (60/40).

Table F.2. Mechanical properties of Asp/PP fibers.

	Asp/PP (20/80) T5B2-2 Drawn	Asp/PP (60/40) T5D3-5 Drawn	Asp/PP (100/0) T5F3 As-spun
Diameter (μm)	36 ± 18	57 ± 27	62 ± 7
Tensile Strength (MPa)	235 ± 22	67 ± 14	11 ± 0.3
Tensile Modulus (GPa)	5.3 ± 0.8	2.7 ± 0.6	0.6 ± 0.4
Elongation at Break (%)	115 ± 49	37 ± 24	2.2 ± 0.6

Stabilization of fibers with asphaltene as the majority component (60 wt%) was attempted, without the application of any tension. Three bundles of drawn fibers of Asp-PP (60/40) were soaked in the spin finish solution (SF-LUROL CF-14676 supplied by Goulston Technologies, North Carolina; Concentration: 5 wt% of spin finish in deionized water) for 2h. The fibers were heated at 3 °C /min to 350 °C and held for 170 min, and then heated s at 3 °C /min to 375 °C and held for 10 min. At the end of stabilization, length of the fibers in Bundle 1 decreased by ~67 %. During this process, fibers fused together. Fibers were brittle and it was difficult to separate the fibers into single filaments as they broke while doing so. Fibers from Bundle 2 did not survive the stabilization process. While for Bundle 3, very few filaments that were stuck to the base of the holder were found. Figure F.3 shows the fibers before and after stabilization.

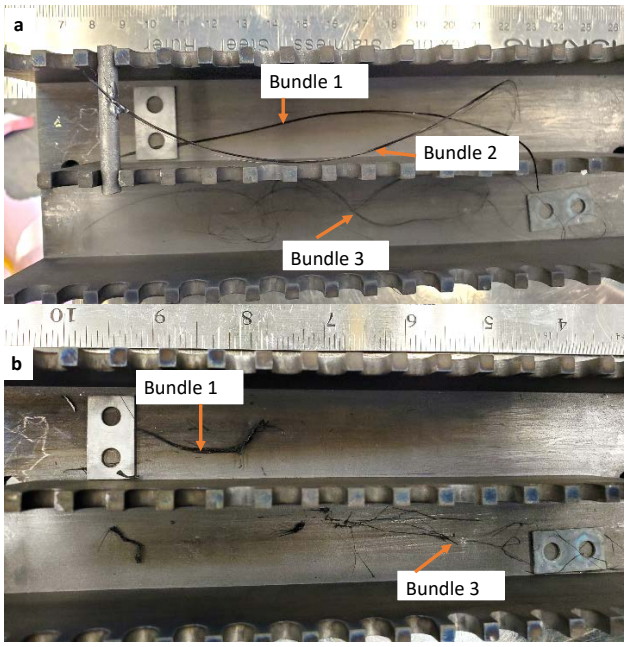

Figure F.3. (a) Experimental set up for stabilizing Asp-PP (60/40) precursor fibers and (b) stabilized fibers.

Wide angle X-ray diffraction (WAXD) using CuK_{α} ($\lambda = 0.1542$ nm) manufactured by Rigaku Micromax-002 (operating voltage and current 50 KV and 0.60 mA) was conducted on Asp powder and Asp-PP (60/40) drawn precursor and stabilized fibers. Figure F4 shows the corresponding integrated WAXD scans. Asp powder had three characteristic peaks 2θ~11-20º , ~26º and ~43º, as reported in the literature.[171] Characteristic peaks of PP at 2θ~14º, 17º, 18.5º, 21º, 22º are dominant in the precursor fiber.[185] PP's characteristic peaks were still present in the stabilized fibers indicating that further work is needed to stabilize this fiber.

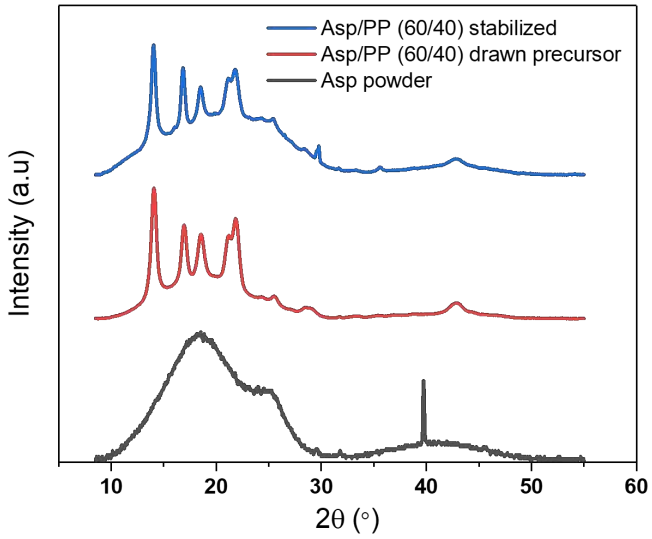

Figure F.4. Integrated WAXD scans of Asp powder, Asp-PP (60/40) drawn precursor and Asp-PP (60/40) stabilized fibers.

Asp-PP fibers of various compositions (wt%/wt%) were melt compounded and extruded. Ductility of the fibers decreased with the increasing content of PP in the fibers.

Fibers of Asp-PP (20/80) and Asp-PP (60/40) were successfully hot drawn. Fibers of Asp-PP (100/0) were brittle and hot drawing the fibers at 135 °C was not feasible. Asp-PP (20/80) drawn precursor fiber of tensile strength 235 MPa and tensile modulus 5.3GPa were made. PP and other thermoplastic composite fibers with Asp as filler could be of potential interest. Asp-PP (60/40) drawn precursor fiber of tensile strength 67 MPa and tensile modulus 2.7 GPa were made. Stabilization of these fibers was attempted, but not complete. Further recommendation for Asp-PP fibers would be to look into the prospect of Asp as filler for PP and other thermoplastic fibers. Asp-PP blend fibers can potentially be use for concrete reinforcement. As for manufacturing carbon fibers through this route, further work is needed to optimize the stabilization protocol before proceeding to carbonization.

REFERENCES

(1) Jung, H.; Bielawski, C. W. Asphaltene Oxide Promotes a Broad Range of Synthetic Transformations. *Commun. Chem.* **2019**, *2* (1), 1–9. https://doi.org/10.1038/s42004-019-0214-4.

(2) Chand, S. Carbon Fibers for Composites. *J. Mater. Sci.* **2000**, *35* (6), 1303–1313. https://doi.org/10.1023/A:1004780301489.

(3) Newcomb, B. A. Processing, Structure, and Properties of Carbon Fibers. *Composites Part A: Applied Science and Manufacturing*. 2016. https://doi.org/10.1016/j.compositesa.2016.10.018.

(4) Liu, Y.; Kumar, S. Recent Progress in Fabrication, Structure, and Properties of Carbon Fibers. *Polym. Rev.* **2012**, *52* (3–4), 234–258. https://doi.org/10.1080/15583724.2012.705410.

(5) Paris, O.; Peterlik, H. *The Structure of Carbon Fibres*; Woodhead Publishing Limited, 2009; Vol. 2. https://doi.org/10.1533/9781845697310.3.353.

(6) Carbon, C. F.; Pan-, T. CHAPTER 4 Carbon Fibers. *New Carbons - Control Struct. Funct.* **1994**. https://doi.org/https://doi.org/10.1016/B978-008043713-2/50004-2.

(7) Park, S. J.; Seo, M. K. *Element and Processing*; 2011; Vol. 18. https://doi.org/10.1016/B978-0-12-375049-5.00006-2.

(8) Morris, E. A.; Weisenberger, M. C.; Abdallah, M. G.; Vautard, F.; Grappe, H.; Ozcan, S.; Paulauskas, F. L.; Eberle, C.; Jackson, D.; Mecham, S. J.; Naskar, A. K. High Performance Carbon Fibers from Very High Molecular Weight Polyacrylonitrile Precursors. *Carbon N. Y.* **2016**, *101*, 245–252. https://doi.org/10.1016/j.carbon.2016.01.104.

(9) Morris, E. A.; Weisenberger, M. C. Solution Spinning of PAN-Based Polymers for Carbon Fiber Precursors. *ACS Symp. Ser.* **2014**, *1173*, 189–213.

https://doi.org/10.1021/bk-2014-1180.ch009.

(10) Minus, M. L.; Kumar, S. The Processing, Properties, and Structure of Carbon Fibers. *J. Miner. Met. Mater. Soc.* **2005**, *57*, 52–58. https://doi.org/10.1007/s11837-005-0217-8.

(11) Chae, H. G.; Newcomb, B. A.; Gulgunje, P. V.; Liu, Y.; Gupta, K. K.; Kamath, M. G.; Lyons, K. M.; Ghoshal, S.; Pramanik, C.; Giannuzzi, L.; Şahin, K.; Chasiotis, I.; Kumar, S. High Strength and High Modulus Carbon Fibers. *Carbon N. Y.* **2015**, *93*, 81–87. https://doi.org/10.1016/j.carbon.2015.05.016.

(12) Newcomb, B. A.; Gulgunje, P. V.; Gupta, K.; Kamath, M. G.; Liu, Y.; Giannuzzi, L. A.; Chae, H. G.; Kumar, S. Processing, Structure, and Properties of Gel Spun PAN and PAN/CNT Fibers and Gel Spun PAN Based Carbon Fibers. *Polym. Eng. Sci.* **2015**. https://doi.org/10.1002/pen.24153.

(13) Dalton, S.; Heatley, F.; Budd, P. M. Thermal Stabilization of Polyacrylonitrile Fibres. *Polymer (Guildf).* **1999**, *40* (20), 5531–5543. https://doi.org/10.1016/S0032-3861(98)00778-2.

(14) Lee, S.; Kim, J.; Ku, B.-C.; Kim, J.; Joh, H.-I. Structural Evolution of Polyacrylonitrile Fibers in Stabilization and Carbonization. *Adv. Chem. Eng. Sci.* **2012**, *02* (02), 275–282. https://doi.org/10.4236/aces.2012.22032.

(15) Liu, Y.; Chae, H. G.; Kumar, S. Gel-Spun Carbon Nanotubes/Polyacrylonitrile Composite Fibers. Part II: Stabilization Reaction Kinetics and Effect of Gas Environment. *Carbon N. Y.* **2011**, *49* (13), 4477–4486. https://doi.org/10.1016/j.carbon.2011.06.042.

(16) Fitzer, E.; Frohs, W.; Heine, M. Optimization of Stabilization and Carbonization Treatment of PAN Fibres and Structural Characterization of the Resulting Carbon Fibres. *Carbon N. Y.* **1986**, *24* (4), 387–395. https://doi.org/10.1016/0008-6223(86)90257-5.

(17) Koumoulos, E. P.; Trompeta, A. F.; Santos, R. M.; Martins, M.; Dos Santos, C. M.; Iglesias, V.; Böhm, R.; Gong, G.; Chiminelli, A.; Verpoest, I.; Kiekens, P.; Charitidis, C. A. Research and Development in Carbon Fibers and Advanced High-Performance Composites Supply Chain in Europe: A Roadmap for

Challenges and the Industrial Uptake. *J. Compos. Sci.* **2019**, *3* (3). https://doi.org/10.3390/jcs3030086.

(18) Toray CSR 2020 https://www.toray.com/global/sustainability/download/pdf/Toray_CSR_report2020_english_03.pdf.

(19) https://www.energy.gov/eere/articles/carbon-fiber-and-clean-energy-4-uses-industry.

(20) Zhang, J.; Chevali, V. S.; Wang, H.; Wang, C. H. Current Status of Carbon Fibre and Carbon Fibre Composites Recycling. *Compos. Part B Eng.* **2020**, *193* (April), 108053. https://doi.org/10.1016/j.compositesb.2020.108053.

(21) Hiremath, N.; Young, S.; Ghossein, H.; Penumadu, D.; Vaidya, U.; Theodore, M. Low Cost Textile-Grade Carbon-Fiber Epoxy Composites for Automotive and Wind Energy Applications. *Compos. Part B Eng.* **2020**, *198* (April), 108156. https://doi.org/10.1016/j.compositesb.2020.108156.

(22) Pervaiz, M.; Panthapulakkal, S.; KC, B.; Sain, M.; Tjong, J. Emerging Trends in Automotive Lightweighting through Novel Composite Materials. *Mater. Sci. Appl.* **2016**, *07* (01), 26–38. https://doi.org/10.4236/msa.2016.71004.

(23) Yang, J.; Liu, Y.; Liu, J.; Shen, Z.; Liang, J.; Wang, X. Rapid and Continuous Preparation of Polyacrylonitrile-Based Carbon Fibers with Electron-Beam Irradiation Pretreatment. *Materials (Basel).* **2018**, *11* (8), 1–10. https://doi.org/10.3390/ma11081270.

(24) Sullivan, R. A. Automotive Carbon Fiber: Opportunities and Challenges. *Jom* **2006**, *58* (11), 77–79. https://doi.org/10.1007/s11837-006-0233-3.

(25) Kleinbaum, S.; Jiang, C.; Logan, S. Enabling Sustainable Transportation through Joining of Dissimilar Lightweight Materials. *MRS Bull.* **2019**, *44* (8), 608–612. https://doi.org/10.1557/mrs.2019.178.

(26) Baker, D. A.; Rials, T. G. Recent Advances in Low-Cost Carbon Fiber Manufacture from Lignin. *J. Appl. Polym. Sci.* **2013**, *130* (2), 713–728.

https://doi.org/10.1002/app.39273.

(27) Sánchez-Romate, X. F.; Bosque, A. Del; Artigas-Arnaudas, J.; Muñoz, B. K.; Sánchez, M.; Ureña, A. A Proof of Concept of a Structural Supercapacitor Made of Graphene Coated Woven Carbon Fibers: EIS Study and Mechanical Performance. *Electrochim. Acta* **2021**, *370*. https://doi.org/10.1016/j.electacta.2021.137746.

(28) Aly, N. M. A Review on Utilization of Textile Composites in Transportation towards Sustainability. *IOP Conf. Ser. Mater. Sci. Eng.* **2017**, *254* (4). https://doi.org/10.1088/1757-899X/254/4/042002.

(29) https://www.energy.gov/eere/vehicles/lightweight-and-propulsion-materials.

(30) Chen, S.; Qiu, L.; Cheng, H. M. Carbon-Based Fibers for Advanced Electrochemical Energy Storage Devices. *Chem. Rev.* **2020**, *120* (5), 2811–2878. https://doi.org/10.1021/acs.chemrev.9b00466.

(31) Asp, L. E.; Bouton, K.; Carlstedt, D.; Duan, S.; Harnden, R.; Johannisson, W.; Johansen, M.; Johansson, M. K. G.; Lindbergh, G.; Liu, F.; Peuvot, K.; Schneider, L. M.; Xu, J.; Zenkert, D. A Structural Battery and Its Multifunctional Performance. *Adv. Energy Sustain. Res.* **2021**, *2* (3), 2000093. https://doi.org/10.1002/aesr.202000093.

(32) Johannisson, W.; Zenkert, D.; Lindbergh, G. Model of a Structural Battery and Its Potential for System Level Mass Savings. *Multifunct. Mater.* **2019**, *2* (3), 035002. https://doi.org/10.1088/2399-7532/ab3bdd.

(33) Newcomb, B. A.; Chae, H. G. The Properties of Carbon Fibers. In *Handbook of Properties of Textile and Technical Fibres*; Woodhead Publishing, 2018; pp 841–871. https://doi.org/10.1016/b978-0-08-101272-7.00021-3.

(34) Chen, Y.; Amiri, A.; Boyd, J. G.; Naraghi, M. Promising Trade-Offs Between Energy Storage and Load Bearing in Carbon Nanofibers as Structural Energy Storage Devices. *Adv. Funct. Mater.* **2019**, *29* (33), 1–11. https://doi.org/10.1002/adfm.201901425.

(35) Qian, H.; Diao, H.; Shirshova, N.; Greenhalgh, E. S.; Steinke, J. G. H.; Shaffer, M. S. P.; Bismarck, A. Activation of Structural Carbon Fibres for Potential Applications in Multifunctional Structural Supercapacitors. *J. Colloid Interface Sci.* **2013**, *395* (1), 241–248. https://doi.org/10.1016/j.jcis.2012.12.015.

(36) Asp, L. E.; Greenhalgh, E. S. Structural Power Composites. *Compos. Sci. Technol.* **2014**, *101*, 41–61. https://doi.org/10.1016/j.compscitech.2014.06.020.

(37) Shirshova, N.; Qian, H.; Shaffer, M. S. P.; Steinke, J. H. G.; Greenhalgh, E. S.; Curtis, P. T.; Kucernak, A.; Bismarck, A. Structural Composite Supercapacitors. *Compos. Part A Appl. Sci. Manuf.* **2013**, *46*, 96–107. https://doi.org/10.1016/j.compositesa.2012.10.007.

(38) Johannisson, W.; Ihrner, N.; Zenkert, D.; Johansson, M.; Carlstedt, D.; Asp, L. E.; Sieland, F. Multifunctional Performance of a Carbon Fiber UD Lamina Electrode for Structural Batteries. *Compos. Sci. Technol.* **2018**, *168* (August), 81–87. https://doi.org/10.1016/j.compscitech.2018.08.044.

(39) Asp, L. E.; Johansson, M.; Lindbergh, G.; Xu, J.; Zenkert, D. Structural Battery Composites: A Review. *Funct. Compos. Struct.* **2019**, *1* (4), 042001. https://doi.org/10.1088/2631-6331/ab5571.

(40) Shirshova, N.; Qian, H.; Houllé, M.; Steinke, J. H. G.; Kucernak, A. R. J.; Fontana, Q. P. V.; Greenhalgh, E. S.; Bismarck, A.; Shaffer, M. S. P. Multifunctional Structural Energy Storage Composite Supercapacitors. *Faraday Discuss.* **2014**, *172* (0), 81–103. https://doi.org/10.1039/c4fd00055b.

(41) Chang, H.; Luo, J.; Gulgunje, P. V.; Kumar, S. Structural and Functional Fibers. *Annu. Rev. Mater. Res.* **2017**, *47* (1), 331–359. https://doi.org/10.1146/annurev-matsci-120116-114326.

(42) Chen, Y.; Cai, J.; Boyd, J. G.; Kennedy, W. J.; Naraghi, M. Mechanics of Emulsion Electrospun Porous Carbon Fibers as Building Blocks of Multifunctional Materials. *ACS Appl. Mater. Interfaces* **2018**, *10* (44), 38310–38318. https://doi.org/10.1021/acsami.8b10499.

(43) Kamkar, M.; Natale, G. A Review on Novel Applications of Asphaltenes: A Valuable Waste. *Fuel* **2021**, *285* (August 2020), 119272.

https://doi.org/10.1016/j.fuel.2020.119272.

(44) Leistenschneider, D.; Zuo, P.; Kim, Y.; Abedi, Z.; Ivey, D. G.; de Klerk, A.; Zhang, X.; Chen, W. A Mechanism Study of Acid-Assisted Oxidative Stabilization of Asphaltene-Derived Carbon Fibers. *Carbon Trends* **2021**, *5*, 100090. https://doi.org/10.1016/j.cartre.2021.100090.

(45) Zuo, P.; Leistenschneider, D.; Kim, Y.; Abedi, Z.; Ivey, D. G.; Zhang, X.; Chen, W. Asphaltene Thermal Treatment and Optimization of Oxidation Conditions of Low-Cost Asphaltene-Derived Carbon Fibers. *J. Ind. Eng. Chem.* **2021**, No. xxxx. https://doi.org/10.1016/j.jiec.2021.08.039.

(46) Https://Www.Jwnenergy.Com/Article/2020/3/2/Carbon-Fibre-Bitumen-Offers-Emissions-Benefits-Mul/.

(47) Lee, J.; Kim, J.; Hyeon, T. Recent Progress in the Synthesis of Porous Carbon Materials. *Adv. Mater.* **2006**, *18* (16), 2073–2094. https://doi.org/10.1002/adma.200501576.

(48) Sun, B.; Fu, R.; Wu, D.; He, H.; Xu, F.; Matyjaszewski, K. Design and Preparation of Porous Polymers. *Chem. Rev.* **2012**, *112* (7), 3959–4015. https://doi.org/10.1021/cr200440z.

(49) Ozaki, J.; Endo, N.; Ohizumi, W.; Igarashi, K.; Nakahara, M.; Oya, A.; Yoshida, S.; Iizuka, T. Novel Preparation Method for the Production of Mesoporous Carbon Fiber from a Polymer Blend. *Carbon N. Y.* **1997**, *35* (7), 1031–1033. https://doi.org/10.1016/S0008-6223(97)89878-8.

(50) Patel, N.; Okabe, K.; Oya, A. Designing Carbon Materials with Unique Shapes Using Polymer Blending and Coating Techniques. *Carbon N. Y.* **2002**, *40* (3), 315–320. https://doi.org/10.1016/S0008-6223(01)00101-4.

(51) Joo, S. H.; Choi, S. J.; Oh, I.; Kwak, J. Ordered Nanoporous Arrays of Carbon.Pdf. **2001**, *412* (July). https://doi.org/http://www.nature.com/nature/journal/v412/n6843/suppinfo/412169a0_S1.html.

(52) Liang, C.; Li, Z.; Dai, S. Mesoporous Carbon Materials: Synthesis and Modification. *Angew. Chemie - Int. Ed.* **2008**, *47* (20), 3696–3717. https://doi.org/10.1002/anie.200702046.

(53) Song, L.; Feng, D.; Campbell, C. G.; Gu, D.; Forster, A. M.; Yager, K. G.; Fredin, N.; Lee, H. J.; Jones, R. L.; Zhao, D.; Vogt, B. D. Robust Conductive Mesoporous Carbon-Silica Composite Films with Highly Ordered and Oriented Orthorhombic Structures from Triblock-Copolymer Template Co-Assembly. *J. Mater. Chem.* **2010**, *20* (9), 1691–1701. https://doi.org/10.1039/b919400b.

(54) Benzigar, M. R.; Talapaneni, S. N.; Joseph, S.; Ramadass, K.; Singh, G.; Scaranto, J.; Ravon, U.; Al-Bahily, K.; Vinu, A. Recent Advances in Functionalized Micro and Mesoporous Carbon Materials: Synthesis and Applications. *Chem. Soc. Rev.* **2018**, *47* (8), 2680–2721. https://doi.org/10.1039/c7cs00787f.

(55) Zhou, Z.; Liu, T.; Khan, A. U.; Liu, G. Block Copolymer – Based Porous Carbon Fibers. **2019**, 1–10.

(56) Lee, J.; Han, S.; Hyeon, T. Synthesis of New Nanoporous Carbon Materials Using Nanostructured Silica Materials as Templates. *J. Mater. Chem.* **2004**, *14* (4), 478. https://doi.org/10.1039/b311541k.

(57) Ji, L.; Lin, Z.; Medford, A. J.; Zhang, X. Porous Carbon Nanofibers from Electrospun Polyacrylonitrile/SiO2 Composites as an Energy Storage Material. *Carbon N. Y.* **2009**, *47* (14), 3346–3354. https://doi.org/10.1016/j.carbon.2009.08.002.

(58) Abeykoon, N. C.; Bonso, J. S.; Ferraris, J. P. Supercapacitor Performance of Carbon Nanofiber Electrodes Derived from Immiscible PAN/PMMA Polymer Blends. *RSC Adv.* **2015**, *5* (26), 19865–19873. https://doi.org/10.1039/C4RA16594B.

(59) Li, Z.; Zhang, J. wei; Yu, L. gui; Zhang, J. wei. Electrospun Porous Nanofibers for Electrochemical Energy Storage. *J. Mater. Sci.* **2017**, *52* (11), 6173–6195. https://doi.org/10.1007/s10853-017-0794-2.

(60) Jo, E.; Yeo, J. G.; Kim, D. K.; Oh, J. S.; Hong, C. K. Preparation of Well-Controlled Porous Carbon Nanofiber Materials by Varying the Compatibility of

Polymer Blends. *Polym. Int.* **2014**, *63* (8), 1471–1477. https://doi.org/10.1002/pi.4645.

(61) Kammer, H. W.; Kressler, J.; Kummerloewe, C. Phase-Behavior of Polymer Blends - Effects of Thermodynamics and Rheology. *Adv. Polym. Sci.* **1993**, *106*, 31–85.

(62) Zhou, Z.; Cao, K.; Chen, X.; Nguyen, M.; Talley, S. J.; Moore, R. B.; Martin, S.; Liu, G. Preferred Domain Orientation in Block Copolymer Fibers after Solvent Annealing. *Mol. Syst. Des. Eng.* **2018**, *3* (2), 357–363. https://doi.org/10.1039/c7me00122c.

(63) Zhou, Z.; Liu, G. Controlling the Pore Size of Mesoporous Carbon Thin Films through Thermal and Solvent Annealing. *Small* **2017**, *13* (15), 19–21. https://doi.org/10.1002/smll.201603107.

(64) BATES, F. S. Polymer-Polymer Phase Behavior. *Science*. 1991, pp 898–905. https://doi.org/10.1126/science.251.4996.898.

(65) Feng, H.; Lu, X.; Wang, W.; Kang, N.-G.; Mays, J.; Xiang, T.; Zhou, Q.; Li, K.; Li, L.; Su, F.; Qian, B.; Zhao, C.; Pathak, J. A.; Colby, R. H.; Kamath, S. Y.; Kumar, S. K.; Stadler, R.; Krause, C.; Wolf, B. A.; Leibler, L.; Li, J.; Ma, P. L.; Favis, B. D.; Matsen, M. W.; Lyngaae???J??rgensen, J.; S??ndergaard, K.; Janert, P. ~K.; Schick, M.; Min, K.; White, J. L.; Fellers, J. F.; Kammer, H. W.; Kressler, J.; Kummerloewe, C.; Salzano De Luna, M.; Filippone, G.; Keestra, B. J.; Goossens, J. G. P.; Anderson, P. D.; Marin, N.; Favis, B. D.; Fowler, M. E.; Barlow, J. W.; Paul, D. R.; Suess, M.; Kressler, J.; Kammer, H. W. Theory of Microphase Separation in Block Copolymers. *Macromolecules* **1987**, *28* (17), 31–85. https://doi.org/10.1016/S0032-3861(02)00280-X.

(66) Fowler, M. E.; Barlow, J. W.; Paul, D. R. Effect of Copolymer Composition on the Miscibility of Blends of Styrene-Acrylonitrile Copolymers with Poly (Methyl Methacrylate). *Polymer (Guildf).* **1987**, *28* (7), 1177–1184. https://doi.org/10.1016/0032-3861(87)90261-8.

(67) Palanisamy, A.; Salim, N. V.; Fox, B. L.; Jyotishkumar, P.; Pradeep, T.; Hameed, N. A Facile Method to Fabricate Carbon Nanostructures via the Self-Assembly of Polyacrylonitrile/Poly(Methyl Methacrylate-b-Polyacrylonitrile) AB/B′ Type Block Copolymer/Homopolymer Blends. *RSC Adv.* **2016**, *6* (61), 55792–55799.

https://doi.org/10.1039/C6RA09823A.

(68) Mullins, O. C. The Asphaltenes. *Annu. Rev. Anal. Chem.* **2011**, *4*, 393–418. https://doi.org/10.1146/annurev-anchem-061010-113849.

(69) Mullins, O. C.; Sabbah, H.; Eyssautier, J.; Pomerantz, A. E.; Barré, L.; Andrews, A. B.; Ruiz-Morales, Y.; Mostowfi, F.; McFarlane, R.; Goual, L.; Lepkowicz, R.; Cooper, T.; Orbulescu, J.; Leblanc, R. M.; Edwards, J.; Zare, R. N. Advances in Asphaltene Science and the Yen-Mullins Model. *Energy and Fuels* **2012**, *26* (7), 3986–4003. https://doi.org/10.1021/ef300185p.

(70) Reynolds, J. G. *Effects of Asphaltene Precipitation on the Size of Vanadium-, Nickel-, and Sulfur-Containing Compounds in Heavy Crude Oils and Residua*; 1994; Vol. 40. https://doi.org/10.1016/S0376-7361(09)70257-2.

(71) Yen, T. F. Structure of Petroleum Asphaltene and Its Significance. *Energy Sources* **1974**, *1* (4), 447–463. https://doi.org/10.1080/00908317408945937.

(72) Richard Oberreiter, Jan Enemaerke, D. B. (12) Patent Application Publication (10) Pub . No .: US 2014 / 0265900 A1 Sé156 Yv Patent Application Publication. *Appar. Methods Control. Appl. Flash Lamp Radation* **2014**, *1* (19).

(73) Qin, F.; Jiang, W.; Ni, G.; Wang, J.; Zuo, P.; Qu, S.; Shen, W. From Coal-Heavy Oil Co-Refining Residue to Asphaltene-Based Functional Carbon Materials. *ACS Sustain. Chem. Eng.* **2019**, *7* (4), 4523–4531. https://doi.org/10.1021/acssuschemeng.9b00003.

(74) Zuo, P.; Qu, S.; Shen, W. Asphaltenes: Separations, Structural Analysis and Applications. *J. Energy Chem.* **2019**, *34*, 186–207. https://doi.org/10.1016/j.jechem.2018.10.004.

(75) Ni, G.; Jiang, W.; Shen, W. Chemical Modification of Asphaltene with SEBS as Precursor for Isotropic Pitch-Based Carbon Fiber. *ChemistrySelect* **2019**, *4* (13), 3690–3696. https://doi.org/10.1002/slct.201803764.

(76) Natarajan, A.; Mahavadi, S. C.; Natarajan, T. S.; Masliyah, J. H.; Xu, Z. Preparation of Solid and Hollow Asphaltene Fibers by Single Step

Electrospinning. *J. Eng. Fiber. Fabr.* **2011**, *6* (2), 1–6. https://doi.org/10.1177/155892501100600201.

(77) Abedi, Z.; Leistenschneider, D.; Chen, W.; Ivey, D. G. Superior Performance of Electrochemical Double Layer Supercapacitor Made with Asphaltene Derived Activated Carbon Fibers. *Energy Technol.* **2020**, *8* (12), 1–11. https://doi.org/10.1002/ente.202000588.

(78) Kim, C.; Jeong, Y. Il; Ngoc, B. T. N.; Yang, K. S.; Kojima, M.; Kim, Y. A.; Endo, M.; Lee, J. W. Synthesis and Characterization of Porous Carbon Nanofibers with Hollow Cores through the Thermal Treatment of Electrospun Copolymeric Nanofiber Webs. *Small* **2007**, *3* (1), 91–95. https://doi.org/10.1002/smll.200600243.

(79) Yu, H. J.; Fridrikh, S. V.; Rutledge, G. C. Production of Submicrometer Diameter Fibers by Two-Fluid Electrospiiming. *Adv. Mater.* **2004**, *16* (17), 1562–1566. https://doi.org/10.1002/adma.200306644.

(80) Li, G.; Xie, T.; Yang, S.; Jin, J.; Jiang, J. Microwave Absorption Enhancement of Porous Carbon Fibers Compared with Carbon Nanofibers. *J. Phys. Chem. C* **2012**, *116*, 9196–9201. https://doi.org/10.1021/jp300050u.

(81) Liu, J.; Xiong, Z.; Wang, S.; Cai, W.; Yang, J.; Zhang, H. Structure and Electrochemistry Comparison of Electrospun Porous Carbon Nanofibers for Capacitive Deionization. *Electrochim. Acta* **2016**, *210*, 171–180. https://doi.org/10.1016/j.electacta.2016.05.133.

(82) Silva, E. F.; Pereira, R. P.; Rocco, A. M. Ternary Blends of Poly(Ethylene Oxide) and Acrylate-Based Copolymers: Crystallinity, Miscibility, Interactions and Proton Conductivity. *Eur. Polym. J.* **2009**, *45* (11), 3127–3137. https://doi.org/10.1016/j.eurpolymj.2009.08.010.

(83) Noh, S.; Nguyen, D. N.; Park, C. S.; Kim, Y.; Kong, H. J.; Kim, S.; Kim, S.; Hur, S. M.; Yoon, H. Development of Effective Porosity in Carbon Nanofibers Based on Phase Behavior of Ternary Polymer Blend Precursors: Toward High-Performance Electrode Materials. *J. Phys. Chem. C* **2017**, *121* (34), 18480–18489. https://doi.org/10.1021/acs.jpcc.7b02558.

(84) Mathew, M.; Ninan, K. N.; Thomas, S. Compatibility Studies of Polymer-Polymer Systems by Viscometric Techniques: Nitrile-Rubber-Based Polymer Blends. *Polymer (Guildf).* **1998**. https://doi.org/10.1016/S0032-3861(97)10191-4.

(85) Newcomb, B. A.; Gulgunje, P. V.; Liu, Y.; Gupta, K.; Kamath, M. G.; Pramanik, C.; Ghoshal, S.; Chae, H. G.; Kumar, S. Polyacrylonitrile Solution Homogeneity Study by Dynamic Shear Rheology and the Effect on the Carbon Fiber Tensile Strength. *Polym. Eng. Sci.* **2016**. https://doi.org/10.1002/pen.24261.

(86) Liu, H. C.; Tuan, C. C.; Bakhtiary Davijani, A. A.; Wang, P. H.; Chang, H.; Wong, C. P.; Kumar, S. Rheological Behavior of Polyacrylonitrile and Polyacrylonitrile/Lignin Blends. *Polymer (Guildf).* **2017**, *111*, 177–182. https://doi.org/10.1016/j.polymer.2017.01.043.

(87) Wang, L.; Feng, L. F.; Gu, X. P.; Zhang, C. L. Influences of the Viscosity Ratio and Processing Conditions on the Formation of Highly Oriented Ribbons in Polymer Blends by Tape Extrusion. *Ind. Eng. Chem. Res.* **2015**, *54* (44), 11080–11086. https://doi.org/10.1021/acs.iecr.5b03240.

(88) Srivastava, H.; Lade, H.; Paul, D.; Arthanareeswaran, G.; Kweon, J. Styrene-Based Copolymer for Polymer Membrane Modifications. *Appl. Sci.* **2016**, *6* (6), 159. https://doi.org/10.3390/app6060159.

(89) Wang, Z.; Wang, J.; Li, M.; Sun, K.; Liu, C. J. Three-Dimensional Printed Acrylonitrile Butadiene Styrene Framework Coated with Cu-BTC Metal-Organic Frameworks for the Removal of Methylene Blue. *Sci. Rep.* **2014**, *4*, 4–10. https://doi.org/10.1038/srep05939.

(90) Liu, H. C.; Chien, A. T.; Newcomb, B. A.; Liu, Y.; Kumar, S. Processing, Structure, and Properties of Lignin- and CNT-Incorporated Polyacrylonitrile-Based Carbon Fibers. *ACS Sustain. Chem. Eng.* **2015**, *3* (9), 1943–1954. https://doi.org/10.1021/acssuschemeng.5b00562.

(91) Chang, H.; Luo, J.; Liu, H. C.; Bakhtiary Davijani, A. A.; Wang, P. H.; Lolov, G. S.; Dwyer, R. M.; Kumar, S. Ductile Polyacrylonitrile Fibers with High Cellulose Nanocrystals Loading. *Polymer (Guildf).* **2017**, *122*, 332–339. https://doi.org/10.1016/j.polymer.2017.06.072.

(92) Chien, A. T.; Newcomb, B. A.; Sabo, D.; Robbins, J.; Zhang, Z. J.; Kumar, S. High-Strength Superparamagnetic Composite Fibers. *Polymer (Guildf).* **2014**, *55* (16), 4116–4124. https://doi.org/10.1016/j.polymer.2014.06.028.

(93) Chae, H. G.; Minus, M. L.; Kumar, S. Oriented and Exfoliated Single Wall Carbon Nanotubes in Polyacrylonitrile. *Polymer (Guildf).* **2006**, *47* (10), 3494–3504. https://doi.org/10.1016/j.polymer.2006.03.050.

(94) Rahaman, M. S. A.; Ismail, A. F.; Mustafa, A. A Review of Heat Treatment on Polyacrylonitrile Fiber. *Polym. Degrad. Stab.* **2007**, *92* (8), 1421–1432. https://doi.org/10.1016/j.polymdegradstab.2007.03.023.

(95) Gupta, A.; Harrison, I. R. New Aspects in the Oxidative Stabilization of Pan-Based Carbon Fibers: II. *Carbon N. Y.* **1997**, *35* (6), 809–818. https://doi.org/10.1016/S0008-6223(97)00025-0.

(96) Liu, H. C.; Chien, A. T.; Newcomb, B. A.; Bakhtiary Davijani, A. A.; Kumar, S. Stabilization Kinetics of Gel Spun Polyacrylonitrile/Lignin Blend Fiber. *Carbon N. Y.* **2016**, *101*, 382–389. https://doi.org/10.1016/j.carbon.2016.01.096.

(97) Luo, J.; Chang, H.; Wang, P. H.; Moon, R. J.; Kumar, S. Cellulose Nanocrystals Effect on the Stabilization of Polyacrylonitrile Composite Films. *Carbon N. Y.* **2018**, *134*, 92–102. https://doi.org/10.1016/j.carbon.2018.03.078.

(98) Chang, H.; Luo, J.; Liu, H. C.; Zhang, S.; Park, J. G.; Liang, Z.; Kumar, S. Stabilization Study of Polyacrylonitrile/Cellulose Nanocrystals Composite Fibers. **2019**. https://doi.org/10.1021/acsapm.9b00057.

(99) Kissinger, H. E. Reaction Kinetics in Differential Thermal Analysis. *Anal. Chem.* **1957**, *29* (11), 1702–1706. https://doi.org/10.1021/ac60131a045.

(100) Reghunadhan Nair, C. P.; Krishnan, K.; Ninan, K. N. Differential Scanning Calorimetric Study on the Claisen Rearrangement and Thermal Polymerisation of Diallyl Ether of Bisphenols. *Thermochim. Acta* **2000**, *359* (1), 61–67. https://doi.org/10.1016/S0040-6031(00)00504-9.

(101) Fitzer, E.; Müller, D. J. The Influence of Oxygen on the Chemical Reactions

during Stabilization of Pan as Carbon Fiber Precursor. *Carbon N. Y.* **1975**, *13* (1), 63–69. https://doi.org/10.1016/0008-6223(75)90259-6.

(102) Bajaj, P.; Sreekumar, T. V.; Sen, K. Thermal Behaviour of Acrylonitrile Copolymers Having Methacrylic and Itaconic Acid Comonomers. *Polymer (Guildf).* **2001**, *42* (4), 1707–1718. https://doi.org/10.1016/S0032-3861(00)00583-8.

(103) Ju, A.; Guang, S.; Xu, H. Effect of Comonomer Structure on the Stabilization and Spinnability of Polyacrylonitrile Copolymers. *Carbon N. Y.* **2013**, *54*, 323–335. https://doi.org/10.1016/j.carbon.2012.11.044.

(104) Moskowitz, J. D.; Wiggins, J. S. Thermo-Oxidative Stabilization of Polyacrylonitrile and Its Copolymers: Effect of Molecular Weight, Dispersity, and Polymerization Pathway. *Polym. Degrad. Stab.* **2016**, *125*, 76–86. https://doi.org/10.1016/j.polymdegradstab.2015.12.025.

(105) Gulgunje, P. V.; Newcomb, B. A.; Gupta, K.; Chae, H. G.; Tsotsis, T. K.; Kumar, S. Low-Density and High-Modulus Carbon Fibers from Polyacrylonitrile with Honeycomb Structure. *Carbon N. Y.* **2015**, *95*, 710–714. https://doi.org/10.1016/j.carbon.2015.08.097.

(106) Zhou, C.; Liu, T.; Wang, T.; Kumar, S. PAN/SAN/SWNT Ternary Composite: Pore Size Control and Electrochemical Supercapacitor Behavior. *Polymer (Guildf).* **2006**, *47* (16), 5831–5837. https://doi.org/10.1016/j.polymer.2006.06.003.

(107) Wang, T. Electrospun Carbon Nanofibers for Electrochemical Capacitor Electrodes. *Biomol. Eng.* **2007**, No. May.

(108) Yoo, S. H.; Joh, H. I.; Lee, S. Synthesis of Porous Carbon Nanofiber with Bamboo-like Carbon Nanofiber Branches by One-Step Carbonization Process. *Appl. Surf. Sci.* **2017**, *402*, 456–462. https://doi.org/10.1016/j.apsusc.2017.01.154.

(109) Zhang, L.; Han, L.; Liu, S.; Zhang, C.; Liu, S. High-Performance Supercapacitors Based on Electrospun Multichannel Carbon Nanofibers. *RSC Adv.* **2015**, *5*, 107313–107317. https://doi.org/10.1039/C5RA23338K.

(110) Moon, S. C.; Choi, J. K.; Farris, R. J. Highly Porous Polyacrylonitrile/Polystyrene Nanofibers by Electrospinning. *Fibers Polym.* **2008**, *9* (3), 276–280. https://doi.org/10.1007/s12221-008-0044-y.

(111) Liu, J.; Xiong, Z.; Wang, S.; Cai, W.; Yang, J.; Zhang, H. Structure and Electrochemistry Comparison of Electrospun Porous Carbon Nanofibers for Capacitive Deionization. *Electrochim. Acta* **2016**, *210*, 171–180. https://doi.org/10.1016/j.electacta.2016.05.133.

(112) Lee, B. S.; Son, S. B.; Park, K. M.; Lee, G.; Oh, K. H.; Lee, S. H.; Yu, W. R. Effect of Pores in Hollow Carbon Nanofibers on Their Negative Electrode Properties for a Lithium Rechargeable Battery. *ACS Appl. Mater. Interfaces* **2012**, *4* (12), 6702–6710. https://doi.org/10.1021/am301873d.

(113) Gao, Z.; Zhu, J.; Rajabpour, S.; Joshi, K.; Kowalik, M.; Croom, B.; Schwab, Y.; Zhang, L.; Bumgardner, C.; Brown, K. R.; Burden, D.; Klett, J. W.; van Duin, A. C. T.; Zhigilei, L. V.; Li, X. Graphene Reinforced Carbon Fibers. *Sci. Adv.* **2020**, *6* (17), 1–11. https://doi.org/10.1126/sciadv.aaz4191.

(114) Xia, K.; Ouyang, Q.; Chen, Y.; Wang, X.; Qian, X.; Wang, L. Preparation and Characterization of Lignosulfonate-Acrylonitrile Copolymer as a Novel Carbon Fiber Precursor. *ACS Sustain. Chem. Eng.* **2016**, *4* (1), 159–168. https://doi.org/10.1021/acssuschemeng.5b01442.

(115) Krause, S. *Polymer–Polymer Compatibility*; ACADEMIC PRESS, INC., 1978; Vol. I. https://doi.org/10.1016/b978-0-12-546801-5.50008-6.

(116) Chang, H.; Luo, J.; Liu, H. C.; Zhang, S.; Park, J. G.; Liang, R.; Kumar, S. Carbon Fibers from Polyacrylonitrile/Cellulose Nanocrystal Nanocomposite Fibers. *Carbon N. Y.* **2019**, *145*, 764–771. https://doi.org/10.1016/j.carbon.2019.01.045.

(117) Liu, H. C.; Luo, J.; Chang, H.; Bakhtiary Davijani, A. A.; Wang, P.-H.; Kumar, S. Polyacrylonitrile Sheath and Polyacrylonitrile/Lignin Core Bi-Component Carbon Fiber. *Carbon N. Y.* **2019**, *149*, 165–172. https://doi.org/10.1016/j.carbon.2019.04.004.

(118) Ramachandran, J.; Lu, M.; Arias-Monje, P. J.; Kirmani, M. H.; Shirolkar, N.; Kumar, S. Towards Designing Strong Porous Carbon Fibers through Gel Spinning

of Polymer Blends. *Carbon N. Y.* **2021**, *173*, 724–735. https://doi.org/10.1016/j.carbon.2020.10.029.

(119) Zhang, B.; Kang, F.; Tarascon, J. M.; Kim, J. K. Recent Advances in Electrospun Carbon Nanofibers and Their Application in Electrochemical Energy Storage. *Prog. Mater. Sci.* **2016**, *76*, 319–380. https://doi.org/10.1016/j.pmatsci.2015.08.002.

(120) Peng, S.; Li, L.; Kong Yoong Lee, J.; Tian, L.; Srinivasan, M.; Adams, S.; Ramakrishna, S. Electrospun Carbon Nanofibers and Their Hybrid Composites as Advanced Materials for Energy Conversion and Storage. *Nano Energy* **2016**, *22*, 361–395. https://doi.org/10.1016/j.nanoen.2016.02.001.

(121) Lee, J. H.; Kim, I. J.; Park, S. J. Preparation and Electrochemical Behaviors of Styrene-Acrylonitrile-Based Porous Carbon Electrodes. *Electrochim. Acta* **2013**, *113*, 23–28. https://doi.org/10.1016/j.electacta.2013.09.006.

(122) Kim, J. G.; Kim, H. C.; Kim, N. D.; Khil, M. S. N-Doped Hierarchical Porous Hollow Carbon Nanofibers Based on PAN/PVP@SAN Structure for High Performance Supercapacitor. *Compos. Part B Eng.* **2020**, *186* (January), 107825. https://doi.org/10.1016/j.compositesb.2020.107825.

(123) Mooste, M.; Kibena-Põldsepp, E.; Matisen, L.; Merisalu, M.; Kook, M.; Kisand, V.; Vassiljeva, V.; Krumme, A.; Sammelselg, V.; Tammeveski, K. Oxygen Reduction on Catalysts Prepared by Pyrolysis of Electrospun Styrene–Acrylonitrile Copolymer and Multi-Walled Carbon Nanotube Composite Fibres. *Catal. Letters* **2018**, *148* (7), 1815–1826. https://doi.org/10.1007/s10562-018-2392-6.

(124) Mooste, M.; Kibena-Põldsepp, E.; Vassiljeva, V.; Merisalu, M.; Kook, M.; Treshchalov, A.; Kisand, V.; Uibu, M.; Krumme, A.; Sammelselg, V.; Tammeveski, K. Electrocatalysts for Oxygen Reduction Reaction Based on Electrospun Polyacrylonitrile, Styrene–Acrylonitrile Copolymer and Carbon Nanotube Composite Fibres. *J. Mater. Sci.* **2019**, 11618–11634. https://doi.org/10.1007/s10853-019-03725-z.

(125) Niknejad, A. S.; Bazgir, S.; Kargari, A.; Barani, M.; Ranjbari, E.; Rasouli, M. A High-Flux Polystyrene-Reinforced Styrene-Acrylonitrile/Polyacrylonitrile Nanofibrous Membrane for Desalination Using Direct Contact Membrane

Distillation. *J. Memb. Sci.* **2021**, *638* (April), 119744. https://doi.org/10.1016/j.memsci.2021.119744.

(126) Lee, B. S.; Park, K. M.; Yu, W. R.; Youk, J. H. An Effective Method for Manufacturing Hollow Carbon Nanofibers and Microstructural Analysis. *Macromol. Res.* **2012**, *20* (6), 605–613. https://doi.org/10.1007/s13233-012-0087-1.

(127) Lee, B. S.; Son, S. B.; Park, K. M.; Yu, W. R.; Oh, K. H.; Lee, S. H. Anodic Properties of Hollow Carbon Nanofibers for Li-Ion Battery. *J. Power Sources* **2012**, *199*, 53–60. https://doi.org/10.1016/j.jpowsour.2011.10.030.

(128) Jin, L.; Zeng, G.; Wu, H.; Niederberger, M.; Morbidelli, M. A Poly-(Styrene-Acrylonitrile) Copolymer-Derived Hierarchical Architecture in Electrode Materials for Lithium-Ion Batteries. *J. Mater. Chem. A* **2016**, *4* (29), 11481–11490. https://doi.org/10.1039/c6ta04102g.

(129) Zhou, Z.; Liu, T.; Khan, A. U.; Liu, G. Block Copolymer–Based Porous Carbon Fibers. *Sci. Adv.* **2019**, *5* (2), eaau6852. https://doi.org/10.1126/sciadv.aau6852.

(130) Shirolkar, N.; Maffe, A.; DiLoreto, E.; Arias-Monje, P. J.; Lu, M.; Ramachandran, J.; Gulgunje, P.; Gupta, K.; Park, J. G.; Shih, K. C.; Kirmani, M. H.; Sharits, A.; Nepal, D.; Nieh, M. P.; Liang, R.; Tsotsis, T.; Kumar, S. Multichannel Hollow Carbon Fibers: Processing, Structure, and Properties. *Carbon N. Y.* **2021**, *174*, 730–740. https://doi.org/10.1016/j.carbon.2020.11.077.

(131) Zhou, Z.; Liu, T.; Khan, A. U.; Liu, G. Controlling the Physical and Electrochemical Properties of Block Copolymer-Based Porous Carbon Fibers by Pyrolysis Temperature. *Mol. Syst. Des. Eng.* **2020**, *5* (1), 153–165. https://doi.org/10.1039/c9me00066f.

(132) Serrano, J. M.; Liu, T.; Khan, A. U.; Botset, B.; Stovall, B. J.; Xu, Z.; Guo, D.; Cao, K.; Hao, X.; Cheng, S.; Liu, G. Composition Design of Block Copolymers for Porous Carbon Fibers. *Chem. Mater.* **2019**, *31* (21), 8898–8907. https://doi.org/10.1021/acs.chemmater.9b02918.

(133) Liu, T.; Liu, G. Block Copolymers for Supercapacitors, Dielectric Capacitors and Batteries. *Journal of Physics Condensed Matter*. IOP Publishing 2019.

https://doi.org/10.1088/1361-648X/ab0d77.

(134) Liu, Y.; Chae, H. G.; Choi, Y. H.; Kumar, S. Preparation of Low Density Hollow Carbon Fibers by Bi-Component Gel-Spinning Method. *J. Mater. Sci.* **2015**, *50* (10), 3614–3621. https://doi.org/10.1007/s10853-015-8922-3.

(135) Shirolkar, N.; Maffe, A.; DiLoreto, E.; Arias-Monje, P. J.; Lu, M.; Ramachandran, J.; Gulgunje, P.; Gupta, K.; Park, J. G.; Shih, K. C.; Kirmani, M. H.; Sharits, A.; Nepal, D.; Nieh, M. P.; Liang, R.; Tsotsis, T.; Kumar, S. Multichannel Hollow Carbon Fibers: Processing, Structure, and Properties. *Carbon N. Y.* **2021**, *174*, 730–740. https://doi.org/10.1016/j.carbon.2020.11.077.

(136) González, C.; Vilatela, J. J.; Molina-Aldareguía, J. M.; Lopes, C. S.; LLorca, J. Structural Composites for Multifunctional Applications: Current Challenges and Future Trends. *Prog. Mater. Sci.* **2017**, *89*, 194–251. https://doi.org/10.1016/j.pmatsci.2017.04.005.

(137) Li, J.; Wu, S.; Wu, C.; Qiu, L.; Zhu, G.; Cui, C.; Liu, Y.; Hou, W.; Wang, Y.; Zhang, L.; Teng, I.; Yang, H.-H.; Tan, W. Versatile Surface Engineering of Porous Nanomaterials with Bioinspired Polyphenol Coatings for Targeted and Controlled Drug Delivery. *Nanoscale* **2016**, *8* (16), 8600–8606. https://doi.org/10.1039/C6NR00600K.

(138) Callaway, C. P.; Hendrickson, K.; Bond, N.; Lee, S. M.; Sood, P.; Jang, S. S. Molecular Modeling Approach to Determine the Flory-Huggins Interaction Parameter for Polymer Miscibility Analysis. *ChemPhysChem* **2018**, *19* (13), 1655–1664. https://doi.org/10.1002/cphc.201701337.

(139) Ahmed, E.; Womble, C. T.; Cho, J.; Dancel-Manning, K.; Rice, W. J.; Jang, S. S.; Weck, M. One-Pot Synthesis of Linear Triblock Terpolymers and Their Aqueous Self-Assembly. *Polym. Chem.* **2021**, *12* (13), 1967–1974. https://doi.org/10.1039/d1py00054c.

(140) Thommes, M.; Kaneko, K.; Neimark, A. V.; Olivier, J. P.; Rodriguez-Reinoso, F.; Rouquerol, J.; Sing, K. S. W. Physisorption of Gases, with Special Reference to the Evaluation of Surface Area and Pore Size Distribution (IUPAC Technical Report). *Pure Appl. Chem.* **2015**, *87* (9–10), 1051–1069. https://doi.org/10.1515/pac-2014-1117.

(141) Naeimirad, M.; Zadhoush, A.; Kotek, R.; Esmaeely Neisiany, R.; Nouri Khorasani, S.; Ramakrishna, S. Recent Advances in Core/Shell Bicomponent Fibers and Nanofibers: A Review. *J. Appl. Polym. Sci.* **2018**, *135* (21), 28–30. https://doi.org/10.1002/app.46265.

(142) Maqsood, M.; Seide, G. Novel Bicomponent Functional Fibers with Sheath/Core Configuration Containing Intumescent Flame-Retardants for Textile Applications. *Materials (Basel).* **2019**, *12* (19). https://doi.org/10.3390/ma12193095.

(143) Yang, Z.; Peng, H.; Wang, W.; Liu, T. Crystallization Behavior of Poly(ε-Caprolactone)/Layered Double Hydroxide Nanocomposites. *J. Appl. Polym. Sci.* **2010**, *116* (5), 2658–2667. https://doi.org/10.1002/app.

(144) Minagawao, N.; White, J. L. Influence of Viscosity and Die Cross-Section on Interface Shape. *Engineering* **1975**, *15*, 825–830.

(145) Rwei, S. P.; Lin, Y. T.; Su, Y. Y. Study of Self-Crimp Polyester Fibers. *Polym. Eng. Sci.* **2005**, *45* (6), 838–845. https://doi.org/10.1002/pen.20338.

(146) Prahsarn, C.; Klinsukhon, W.; Roungpaisan, N.; Srisawat, N. Self-Crimped Bicomponent Fibers Containing Polypropylene/Ethylene Octene Copolymer. *Mater. Lett.* **2013**, *91*, 232–234. https://doi.org/10.1016/j.matlet.2012.09.106.

(147) Oh, T. H. Effects of Spinning and Drawing Conditions on the Crimp Contraction of Side-by-Side Poly(Trimethylene Terephthalate) Bicomponent Fibers. *J. Appl. Polym. Sci.* **2006**, *102* (2), 1322–1327. https://doi.org/10.1002/app.23988.

(148) Lin, T.; Wang, H.; Wang, X. Self-Crimping Bicomponent Nanofibers Electrospun from Polyacrylonitrile and Elastomeric Polyurethane. *Adv. Mater.* **2005**, *17* (22), 2699–2703. https://doi.org/10.1002/adma.200500901.

(149) Chien, A. T.; Gulgunje, P. V.; Chae, H. G.; Joshi, A. S.; Moon, J.; Feng, B.; Peterson, G. P.; Kumar, S. Functional Polymer-Polymer/Carbon Nanotube Bi-Component Fibers. *Polymer (Guildf).* **2013**, *54* (22), 6210–6217. https://doi.org/10.1016/j.polymer.2013.08.061.

(150) Wiley, J. Effect of Crimp on the Tensile and Compressive Properties. **1971**, No. I,

1539–1544.

(151) Sawai, D.; Kanamoto, T.; Yamazaki, H.; Hisatani, K. Dynamic Mechanical Relaxations in Poly(Acrylonitrile) with Different Stereoregularities. *Macromolecules* **2004**, *37* (8), 2839–2846. https://doi.org/10.1021/ma0352330.

(152) Lu, B.; Lamnawar, K.; Maazouz, A.; Zhang, H. Revealing the Dynamic Heterogeneity of PMMA/PVDF Blends: From Microscopic Dynamics to Macroscopic Properties. *Soft Matter* **2016**, *12* (13), 3252–3264. https://doi.org/10.1039/c5sm02659h.

(153) Ji, H.; Zhao, X.; Qiao, Z.; Jung, J.; Zhu, Y.; Lu, Y.; Zhang, L. L.; MacDonald, A. H.; Ruoff, R. S. Capacitance of Carbon-Based Electrical Double-Layer Capacitors. *Nat. Commun.* **2014**, *5* (Cmcm). https://doi.org/10.1038/ncomms4317.

(154) Dyatkin, B.; Gogotsi, Y. Effects of Structural Disorder and Surface Chemistry on Electric Conductivity and Capacitance of Porous Carbon Electrodes. *Faraday Discuss.* **2014**, *172*, 139–162. https://doi.org/10.1039/c4fd00048j.

(155) Fredi, G.; Jeschke, S.; Boulaoued, A.; Wallenstein, J.; Rashidi, M.; Liu, F.; Harnden, R.; Zenkert, D.; Hagberg, J.; Lindbergh, G.; Johansson, P.; Stievano, L.; Asp, L. E. Graphitic Microstructure and Performance of Carbon Fibre Li-Ion Structural Battery Electrodes. *Multifunct. Mater.* **2018**, *1* (1). https://doi.org/10.1088/2399-7532/aab707.

(156) Snyder, J. F.; Wong, E. L.; Hubbard, C. W. Evaluation of Commercially Available Carbon Fibers, Fabrics, and Papers for Potential Use in Multifunctional Energy Storage Applications. *J. Electrochem. Soc.* **2009**, *156* (3), A215. https://doi.org/10.1149/1.3065070.

(157) He, G.; Song, Y.; Chen, S.; Wang, L. Porous Carbon Nanofiber Mats from Electrospun Polyacrylonitrile/Polymethylmethacrylate Composite Nanofibers for Supercapacitor Electrode Materials. *J. Mater. Sci.* **2018**, *53* (13), 9721–9730. https://doi.org/10.1007/s10853-018-2277-5.

(158) Khomenko, V.; Raymundo-Piñero, E.; Béguin, F. Optimisation of an Asymmetric Manganese Oxide/Activated Carbon Capacitor Working at 2 v in Aqueous Medium. *J. Power Sources* **2006**, *153* (1), 183–190.

https://doi.org/10.1016/j.jpowsour.2005.03.210.

(159) Gracia-Medrano-Bravo, V. A.; Merklein, L.; Oberle, N.; Batora, M.; Scharfer, P.; Schabel, W. Determination of Binary Interaction Parameters for Ternary Polymer–Polymer–Solvent Systems Using Raman Spectroscopy. *Adv. Mater. Technol.* **2021**, *6* (2), 1–8. https://doi.org/10.1002/admt.202000149.

(160) Kyu, T.; Matkar, R. A.; Lim, D. S.; Ko, C. Discrepancy in Determination of χ Parameters by Melting Point Depression versus Small-Angle Neutron Scattering in Blends of Deuterated Polycarbonate and Isotactic Poly(Methyl Methacrylate). *J. Appl. Crystallogr.* **2007**, *40* (SUPPL. 1), 675–679. https://doi.org/10.1107/S0021889806054999.

(161) Nguyen, C. T.; Kim, D. P. Direct Preparation of Mesoporous Carbon by Pyrolysis of Poly(Acrylonitrile-b-Methylmethacrylate) Diblock Copolymer. *J. Mater. Chem.* **2011**, *21* (37), 14226–14230. https://doi.org/10.1039/c1jm10920k.

(162) Uemura, T.; Kaseda, T.; Sasaki, Y.; Inukai, M.; Toriyama, T.; Takahara, A.; Jinnai, H.; Kitagawa, S. Mixing of Immiscible Polymers Using Nanoporous Coordination Templates. *Nat. Commun.* **2015**, *6* (May). https://doi.org/10.1038/ncomms8473.

(163) Painter, P.; Veytsman, B.; Youtcheff, J. Guide to Asphaltene Solubility. *Energy and Fuels* **2015**, *29* (5), 2951–2961. https://doi.org/10.1021/ef502918t.

(164) Choi, S.; Pyeon, W.; Kim, J. D.; Nho, N. S. Simple Functionalization of Asphaltene and Its Application for Efficient Asphaltene Removal. *Energy and Fuels* **2016**, *30* (9), 6991–7000. https://doi.org/10.1021/acs.energyfuels.6b01184.

(165) Ignatenko, V. Y.; Kostina, Y. V.; Antonov, S. V.; Ilyin, S. O. Oxidative Functionalization of Asphaltenes from Heavy Crude Oil. *Russ. J. Appl. Chem.* **2018**, *91* (11), 1835–1840. https://doi.org/10.1134/S1070427218110149.

(166) Platonov, V. V; Kudrya, A. N.; Proskuryakov, S. V. Ozonolysis of Asphaltenes from Semicoking Tar of G17 Coal. *Russ. J. Appl. Chem.* **2003**, *76* (1), 154–158.

(167) Al-Samarraie, M. F.; Steedman, W. A Study of the Nitric Acid Oxidation of

Petroleum Asphaltenes. *Liq. Fuels Technol.* **1985**, *3* (1), 55–71. https://doi.org/10.1080/07377268508915371.

(168) Worsley, K. A.; Kalinina, I.; Bekyarova, E.; Haddon, R. C. Functionalization and Dissolution of Nitric Acid Treated Single-Walled Carbon Nanotubes. *J. Am. Chem. Soc.* **2009**, *131* (50), 18153–18158. https://doi.org/10.1021/ja906267g.

(169) Kitamura, H.; Sekido, M.; Takeuchi, H.; Ohno, M. The Method for Surface Functionalization of Single-Walled Carbon Nanotubes with Fuming Nitric Acid. *Carbon N. Y.* **2011**, *49* (12), 3851–3856. https://doi.org/10.1016/j.carbon.2011.05.020.

(170) Zhang, F.; Adachi, D.; Tamalampudi, S.; Kondo, A.; Tominaga, K. Real-Time Monitoring of the Transesterification of Soybean Oil and Methanol by Fourier-Transform Infrared Spectroscopy. *Energy and Fuels* **2013**, *27* (10), 5957–5961. https://doi.org/10.1021/ef4012998.

(171) Alhumaidan, F. S.; Hauser, A.; Rana, M. S.; Lababidi, H. M. S.; Behbehani, M. Changes in Asphaltene Structure during Thermal Cracking of Residual Oils: XRD Study. *Fuel* **2015**, *150*, 558–564. https://doi.org/10.1016/j.fuel.2015.02.076.

(172) Liu, Y. J.; Li, Z. F. Structural Characterisation of Asphaltenes during Residue Hydrotreatment with Light Cycle Oil as an Additive. *J. Chem.* **2015**, *2015*. https://doi.org/10.1155/2015/580950.

(173) Andersen, S. I.; Jensen, J. O.; Speight, J. G. X-Ray Diffraction of Subfractions of Petroleum Asphaltenes. *Energy and Fuels* **2005**, *19* (6), 2371–2377. https://doi.org/10.1021/ef050039v.

(174) Bhogle, C.; Pandit, A. B.; Rao, G.; D'Melo, D.; Bhattacharya, S. Impedance Response of Asphaltene Solutions: Effect of Solvation. *Fuel Commun.* **2021**, *7*, 100019. https://doi.org/10.1016/j.jfueco.2021.100019.

(175) Alhreez, M.; Wen, D. Molecular Structure Characterization of Asphaltene in the Presence of Inhibitors with Nanoemulsions. *RSC Adv.* **2019**, *9* (34), 19560–19570. https://doi.org/10.1039/c9ra02664a.

(176) Han, C. D.; Kim, J.; Kim, J. K. Determination of the Order-Disorder Transition Temperature of Block Copolymers. *Macromolecules* **1989**, *22* (1), 383–394. https://doi.org/10.1021/ma00191a071.

(177) Chuang, H.-K.; Han, C. D. Rheological Behavior of Polymer Blends. *J. Appl. Polym. Sci.* **1984**, *29* (6), 2205–2229. https://doi.org/https://doi.org/10.1002/app.1984.070290625.

(178) Painter, P.; Veytsman, B.; Youtcheff, J. Asphaltene Aggregation and Solubility. *Energy and Fuels* **2015**, *29* (4), 2120–2133. https://doi.org/10.1021/ef5024912.

(179) Lu, M.; Xu, J.; Arias-Monje, P. J.; Gulgunje, P. V.; Gupta, K.; Shirolkar, N.; Maffe, A. P.; DiLoreto, E.; Ramachandran, J.; Sahoo, Y.; Agarwal, S.; Meredith, C.; Kumar, S. Continuous Stabilization of Polyacrylonitrile (PAN) - Carbon Nanotube (CNT) Fibers by Joule Heating. *Chem. Eng. Sci.* **2021**, *236*, 116495. https://doi.org/10.1016/j.ces.2021.116495.

(180) Paulauskas, F. L.; Bigelow, T. S.; Yarborough, K. D.; Meek, T. T. Manufacturing of Carbon Fibers Using Microwave-Assisted Plasma Technology. *SAE Tech. Pap.* **2000**, No. 724. https://doi.org/10.4271/2000-01-1527.

(181) Newcomb, B. A.; Giannuzzi, L. A.; Lyons, K. M.; Gulgunje, P. V.; Gupta, K.; Liu, Y.; Kamath, M.; McDonald, K.; Moon, J.; Feng, B.; Peterson, G. P.; Chae, H. G.; Kumar, S. High Resolution Transmission Electron Microscopy Study on Polyacrylonitrile/Carbon Nanotube Based Carbon Fibers and the Effect of Structure Development on the Thermal and Electrical Conductivities. *Carbon N. Y.* **2015**, *93*, 502–514. https://doi.org/10.1016/j.carbon.2015.05.037.

(182) Fiber, C. *HexTow ® IM7*; 2020; Vol. 000.

(183) Khan, M. K.; Riaz, A.; Yi, M.; Kim, J. Removal of Naphthenic Acids from High Acid Crude via Esterification with Methanol. *Fuel Process. Technol.* **2017**, *165*, 123–130. https://doi.org/10.1016/j.fuproc.2017.05.015.

(184) Kumar, S.; Doshi, H.; Srinivasarao, M.; Park, J. O.; Schiraldi, D. A. Fibers from Polypropylene/Nano Carbon Fiber Composites. *Polymer (Guildf).* **2002**, *43* (5), 1701–1703. https://doi.org/10.1016/S0032-3861(01)00744-3.

(185) Ghoshal, S.; Wang, P. H.; Gulgunje, P.; Verghese, N.; Kumar, S. High Impact Strength Polypropylene Containing Carbon Nanotubes. *Polymer (Guildf).* **2016**, *100*, 259–274. https://doi.org/10.1016/j.polymer.2016.07.069.